

QUEEN'S UNIVERSITY BELFAST

**Ab initio Atomistic Thermodynamics of the
(001) surface of Strontium Titanate**

Leandro Liborio
Licentiate in Physics

A thesis submitted to the Faculty of Science and Agriculture
in partial fulfilment of the requirements for the degree of
Doctor of Philosophy.

December 8, 2005

Para Alejandra González Beltrán, por supuesto.

Abstract

The scope of this thesis covers the study of the atomic scale models that were proposed to understand the surface reconstructions that have been observed on $\text{SrTiO}_3(001)$. These atomic scale models were investigated using first principles total energy calculations. Two newly proposed models for $\text{SrTiO}_3(001)$ were studied: the so called *Sr adatom* model and the *double layer* model. In particular, I have focused on the models proposed to explain the (2×1) and $c(4\times 2)$ reconstructions on $\text{SrTiO}_3(001)$, and on the set of surface phase transitions observed by Kubo and Nozoye on $\text{SrTiO}_3(001)$.

To achieve this goal, I have used first principles atomic scale thermodynamics. This technique links concepts and techniques from thermodynamics with results obtained from atomistic electronic structure theory. Since most of the experimental evidence comes from Scanning Tunnelling Microscopy (STM), I have complemented the analysis with simulations of the observed STM images for different surface reconstructions.

The results for the set of surface phase transitions observed by Kubo and Nozoye show that the lower Sr coverage implied in the Sr adatom model can only be explained if the surface is far from equilibrium, in a transient state as it loses Sr to the environment. Depending on the values of the environmental variables, stable atomic scale models were found for the (2×1) and $c(4\times 2)$ reconstructions.

Acknowledgements

In the first place I would like to thank my supervisors Dr. Anthony Paxton and Professor Michael Finnis for all their support throughout these three years. In addition, I would also like to thank Dr. Cristián Sánchez, who helped me from the very beginning, giving me personal and scientific support during all my PhD.

I would also like to thank Dr. Karen Johnston, who always kindly helped me in the first year of my PhD.

I am especially grateful to Dr. Martin Castell and David Newell, from the Department of Materials at Oxford University, who provided me with essential experimental evidence on the (001) surface of Strontium Titanate.

The people in the Atomistic Simulation Centre have provided me with an excellent scientific and human environment to do my PhD. In particular, I would like to thank Dr. Alexander Lozovoi, who helped me understand some key concepts in thermodynamics. Dr. Mario del Popolo has been a friend as well as a critical discussion partner.

The first principles calculations in this thesis were performed with the SIESTA program. All the STM simulated images on this thesis were generated with a program developed by Dr. Cristián Sánchez.

The research described in this dissertation was supported financially by an EPSRC studentship, which the author gratefully acknowledges.

Contents

Contents	2
List of Figures	4
List of Tables	13
1 Introduction	15
1.1 Dissertation outline	18
2 Experimental and theoretical studies on SrTiO₃	20
2.1 Sample preparation, annealing conditions and surface science techniques . .	20
2.2 Relaxation of the (1×1) unreconstructed surface	22
2.2.1 Review of experimental literature	24
2.2.2 Review of theoretical literature	28
3 Thermodynamics	32
3.1 Atomic scale thermodynamics	32
3.1.1 The formalism for the surface free energy	33
3.1.2 Gas phase: the oxygen chemical potential $\mu_{O_2}(p_{O_2}, T)$	39
3.1.3 Discussion: the UHV pressure.	47
4 Total energy calculations with SIESTA	51
4.1 SIESTA basics	52
4.1.1 Numerical atomic orbitals (NAO)	52
4.1.2 Multiple- ζ and polarisation orbitals	53
4.1.3 SIESTA basis for the Strontium Titanate	55
4.2 Tests for SrTiO ₃	56
4.2.1 Lattice and elastic constants of SrTiO ₃	56

<i>CONTENTS</i>	3
4.2.2 Antiferrodistortive phase transition in SrTiO ₃	59
4.2.3 Surface energies	59
4.2.4 The right slab size	60
4.2.5 Bandstructure of SrTiO ₃	61
5 Thermodynamics of the SrTiO₃(001) surfaces	63
5.1 The Sr adatom model	63
5.1.1 Thermodynamics of the Sr adatom model	67
5.1.2 Brief discussion on the kinetics of the Sr adatom model	70
5.2 The Double-layer model and the (2×1) and c(4×2) surface reconstructions	71
5.2.1 Vibrational contributions in the double-layer model	71
5.2.2 The (2×1) and c(4×2) surface reconstructions	76
5.2.3 Thermodynamics of the (2×1) and c(4×2) surface reconstructions .	80
6 STM images	85
6.1 Theory of Tunnelling Microscopy.	85
6.1.1 Tunnelling physics	85
6.1.2 Density of states (DOS) effects	87
6.1.3 Imaging mode	88
6.2 STM images of the Sr adatom model.	88
6.3 STM images for the (2×1) and c(4×2) surface reconstructions	94
6.3.1 The (2×1) reconstruction	94
6.4 The c(4×2) reconstruction	106
6.5 Summary of results	117
7 Conclusions	118
7.1 The Sr adatom model	119
7.2 The (2×1) surface reconstructions	120
7.3 The c(4×2) surface reconstructions	122
7.4 Open questions and future work	123
8 Appendix	125
Bibliography	131

List of Figures

1.1	The two possible (1×1) surface terminations for $\text{SrTiO}_3(001)$: SrO termination is on the left and TiO_2 termination is on the right.	16
1.2	STM images of the (2×1) reconstructed surface obtained by Castell [11]. In figure (a) we can see that the surface morphology has wavy step edges. A horizontal line scan through the centre of (a) is displayed in (b) showing that the steps are 0.4 nm high which corresponds to one bulk unit cell. A high resolution image of one of the terraces (c) shows the 0.8 nm separation between the lines of the (2×1) reconstruction.	17
1.3	STM images of the $c(4\times 2)$ reconstructed surface obtained by Castell [11]. In figure (a) we can see that the surface morphology has straight step edges following the $\langle 010 \rangle$ and $\langle 100 \rangle$. The step height between terraces is 0.4 nm high which corresponds to one bulk unit cell. An atomic resolution image of one of the terraces (b) shows the two domains of the $c(4\times 2)$ reconstruction indicated by surface units cells.	18
2.1	The left picture shows the ideal SrTiO_3 crystal in the $\langle 001 \rangle$ direction. The alternating TiO_2 and SrO layers are clearly seen. The picture on the right shows a schematic diagram of the relaxation parameters. Sr is red, Ti is blue and O is grey. This figure was taken from [26].	24
2.2	Comparison of experimental and theoretical 10, 01 and 11 beams LEED intensity-energy spectra for a $\text{Si}(111)-(\sqrt{3} \times \sqrt{3})-\text{R}30^\circ$ surface[28].	27

3.1	In (a) the vibrational modes at the surface differ by +50% from the bulk values, while in (b) the difference is -50%. The depicted reconstructions are as follows: (1) $(\sqrt{13} \times \sqrt{13})$, (2) $c(4 \times 4)$, (3) $(\sqrt{5} \times \sqrt{5})$ and (4) (2×1) from the Sr adatom model (See Section (5.1)). (5) $c(4 \times 2)$ TiO ₂ -DL(B) and (6) (2×1) TiO ₂ -DL from the Double layer model (See Section (5.2)). Finally, we have (7) (2×1) TiO ₂ -SL which is our proposed model for the (2×1) surface reconstruction (See Section (5.2)).	39
3.2	Distribution of μ_{O_2} around $\bar{\mu}_{O_2}$. The red dotted lines represents the standard deviation for $\bar{\mu}$	44
3.3	Schematic representation of the limits on $\mu_O(p_{O_2}, T)$. The dashed line represents expression (3.35), while the solid one accounts for equation (3.31). The shaded region shows the beginning of the allowed region of $\mu_O(p_{O_2}, T)$ values. The values of μ_{TiO_2} on the x axis go from equilibrium with TiO ₂ (left limit) to equilibrium with SrO (right limit).	46
3.4	Temperature dependence of $\log(p_{O_2})$ within the stated temperature range at $P = 1 \times 10^{-12}$ atm.	50
4.1	Figure produced by Sánchez[73]. It shows confined orbitals for the oxygen atom. s in (a) and (b), p in (c) and (d). In (a), R_c is the cutoff radii we obtain with an confinement energy of 0.1 eV. The thin line in (b) indicates a single- ζ basis. The second radial function is the solid line in (a). As we can see in (b), due to the action of the second radial function $r^l(a - br^2)$, the new double- ζ orbital, represented by a thick line, has a shorter tail than the single- ζ one, showed as a thin line. R_{DZ} indicates the new confinement radii for the double- ζ orbital. Figures (c) and (d) show the same for the p orbital.	54
4.2	(a) fit of energy vs lattice constant. (b) shows the energy vs α curve for the elastic constants C' and C_{44}	57
4.3	(a) temperature dependence of SrTiO ₃ elastic constants in the phase transition region divided by their room temperature values C° [78]. (b), (c) and (d) temperature dependences of C_{11} , C_{12} and C_{44} in SrTiO ₃ from -161 to 30°C[77].	58
4.4	The antiferrodistortive transition of SrTiO ₃ at 105 K. Consecutive oxygen octahedra tilt about the z -axis in a different sense. The figure on the right shows the transition viewed along the z -axis[26].	59

- 4.5 (a) Calculated values and fits of the total energy per unit cell as a function of the octahedral rotation angle θ_z , computed at the frozen theoretical cubic lattice constant, for both R point (diamonds) and M point (circles) octahedral rotation modes. θ_z is shown in the inset of Figure (a) indicating the rotation of the oxygen atoms in the TiO_2 layer[79]. (b) Our fitted values for the total energy per unit cell as a function of θ_z in the R point of the Brillouin zone. 60
- 4.6 (a) Surface energies for the (1×1) and (2×1) surface structures as a function of μ_{TiO_2} at $T=1000$ K and $p_{\text{O}_2}=1$ atm, as calculated by Johnston *et al.*[36]. (b) Our results for the surface energy of the same (1×1) and (2×1) surface reconstructions under the same conditions. 61
- 4.7 (a) Convergence of the unrelaxed (1×1) terminated surface reconstructions for SrTiO_3 with the number of layers in the slab. (b) Shows the convergence of the aforementioned surface reconstructions with the number of vacuum layers between slabs. Three vacuum layers is enough to ensure that no significant interaction between two neighbouring surfaces exists. 62
- 4.8 Electronic band structure of SrTiO_3 obtained with SIESTA. The dashed line indicates the Fermi level. 62
- 5.1 Sr adatom model for the (2×2) ($\theta=0.25$) surface reconstruction of $\text{SrTiO}_3(001)$. On the right we have an oblique view and on the left we have a top view of the proposed surface reconstruction. Ti ions are yellow, Sr ions are red and Oxygens are blue. In the top view the (2×2) surface unit cell is indicated with a black rectangle, and the atomic layer below the surface is shown with reduced depth of colour. 63
- 5.2 STM images of $\text{SrTiO}_3(001)$ after heating to: (a) 1000°C , (b) 1100°C , (c) 1180°C , (d) 1200°C and (e) 1250°C [12]. Proposed Sr adatom models of the $\text{SrTiO}_3(001)$ (f) $c(4 \times 4)(\theta=0.375)$, (g) $(2 \times 2)(\theta=0.25)$, (h) $c(4 \times 4)(\theta=0.125)$, (i) $(4 \times 4)(\theta=0.0625)$, (j) $(\sqrt{5} \times \sqrt{5})\text{-R-}26.6^\circ$ ($\theta=0.2$) and (k) $(\sqrt{13} \times \sqrt{13})\text{-R-}33.7^\circ$ ($\theta=0.0769$) phases[12]. (l)-(n) models to explain the structural phase transitions, all from reference[12]. 64
- 5.3 Top views of the Sr adatom model surface structures listed in Table 5.1. The black circles represent Sr adatoms and the surface unit cell is indicated in each reconstruction. The clean TiO_2 -terminated surface is the atomic layer below each reconstruction and is showed as a foggy background. (a) $c(4 \times 4)$ $\theta = 0.375$ (b) (2×2) $\theta = 0.25$ (c) $(\sqrt{5} \times \sqrt{5})$ $\theta = 0.20$ (d) $c(4 \times 4)$ $\theta = 0.125$ (e) $(\sqrt{13} \times \sqrt{13})$ $\theta = 0.0769$ 66

5.4	Surface phase diagram for the different Sr adatom structures as a function of temperature and partial oxygen pressure. Continuous lines separate the regions in which each structure is stable, the dashed line in figure (a) indicates the oxygen partial pressure in equilibrium with solid C. The surfaces are denoted as follows: (0) TiO ₂ terminated (1 × 1) (1) ($\sqrt{13} \times \sqrt{13}$) $\theta = 0.0769$ (2) $c(4 \times 4)$ $\theta = 0.125$ (3) ($\sqrt{5} \times \sqrt{5}$) $\theta = 0.20$ (4) (2 × 2) $\theta = 0.25$	68
5.5	Surface phase diagram for the different Sr adatom structures as a function of μ_{O} and μ_{TiO_2}	69
5.6	Double layer model for the $c(4 \times 2)$ surface reconstruction of SrTiO ₃ (001). On the right we have an oblique view and on the left we have a top view of the proposed surface reconstruction. Ti ions are yellow, Sr ions are red and Oxygens are blue. In the top view the $c(4 \times 2)$ surface unit cell is indicated with a black rhombus. The atomic layer below the surface is shown with reduced depth of colour and it is a (1 × 1)TiO ₂ -terminated surface.	72
5.7	Top views of the studied surface reconstructions. (a) the (2 × 1)SL-TiO ₂ surface reconstruction. This reconstruction was obtained by SIESTA when relaxing the (2 × 1)SL-TiO ₂ proposed by M. Castell [11]. This surface reconstruction has two types of surface floppy oxygens. (b)-(d) Top views of the (2 × 1)DL-TiO ₂ and $c(4 \times 2)$ DL-TiO ₂ -A/B double-layer surface reconstructions proposed by Erdman <i>et al.</i> [15, 16]. We have labelled each one of the four different surface floppy oxygens on each of these double layer reconstructions.	73
5.8	Temperature dependence of the vibrational contributions due to the floppy oxygens of each of the surface reconstructions studied here.	75
5.9	Four candidate structures proposed for the (2 × 1) surface reconstruction. (a) the double layer model of the (2 × 1) surface reconstruction proposed by Erdman <i>et al.</i> [15]. (b) the Sr adatom model for (2 × 1) surface reconstruction proposed by Kubo and Nozoye[12]. (c) M. Castell's proposed structure of the (2 × 1) reconstructed surface with Ti ₂ O ₃ stoichiometry [11]. (d) the (2 × 1) surface reconstruction proposed by me. This structure has TiO ₂ stoichiometry.	77
5.10	Theoretical direct methods solution of the (2 × 1) structure. (a) the calculated scattering potential map and the primitive unit cell is indicated with solid lines. (b) an interpretation of the map in terms of TiO _x units, where the black spots are regions of high potential -that is possible atomic sites- which subsequent analysis demonstrated were Ti atoms[15].	78

5.11	Top view illustrating the $(\sqrt{2} \times \sqrt{2})R45^\circ$ surface reconstruction.	79
5.12	Four candidate structures proposed for the $c(2 \times 4)$ surface reconstruction. (a) and (b) are the two double layer model proposed by Erdman <i>et al</i> [16]. (c) is the model proposed by Castell[11] and (d) is the Sr adatom model.	79
5.13	Theoretical direct-method solution of the $c(4 \times 2)$ structure[16]. It shows the scattering potential map and the primitive unit cell is indicated with solid lines. The dark features were determined to be Ti sites. The scattering potential map is interpreted in terms of TiO_x pseudo-octahedral units.	80
5.14	Surfaces energies for all the proposed atomic scale models of the (2×1) surface reconstructions. Surface energies are expressed as functions of p_{O_2} at $T = 1000 K$. In (a) the reconstructions are in equilibrium with SrO and in (b) with TiO_2 . The labelling is as follows: TiO_2 -DL \rightarrow Figure (5.9a), Sr adatom \rightarrow Figure (5.9b), Ti_2O_3 -SL \rightarrow Figure (5.9c), TiO_2 -SL \rightarrow Figure (5.9d), TiO_2 -SL1 \rightarrow Figure (5.11).	82
5.15	Surfaces energies for all the proposed atomic scale models of the $c(4 \times 2)$ surface reconstructions. Surface energies are expressed as functions of p_{O_2} at $T = 1000 K$. In (a) the reconstructions are in equilibrium with SrO and in (b) with TiO_2 . The labelling is as follows: TiO_2 -DL(A) \rightarrow Figure (5.12a), TiO_2 -DL(B) \rightarrow Figure (5.12b), TiO_2 -SL \rightarrow Figure (5.12c), Sr adatom \rightarrow Figure (5.12d).	83
6.1	(a) Schematic of quantum-mechanical tunnelling between a metal tip and a metal surface a distance s apart. The tunnelling barrier is determined by the work functions of the surface and tip, ϕ_s and ϕ_t , respectively, and the bias voltage applied between the two, V . For the case shown, surface positive with respect to the tip, electrons tunnel from bands below the Fermi level of the tip to those above the Fermi level of the surface. (b) Detailed schematic of the role of the density of states near E_f on the tunnelling process both into and out of empty and filled states, respectively, on a semiconductor surface. This figure was extracted from L. J. Whitman [88].	86
6.2	Simulated STM images of the Sr adatom model surface structures. Surfaces are denoted as follows: (1) $(\sqrt{13} \times \sqrt{13}) \theta = 0.0769$ (2) $c(4 \times 4) \theta = 0.125$ (3) $(\sqrt{5} \times \sqrt{5}) \theta = 0.20$ (4) $(2 \times 2) \theta = 0.25$. Scales in the x and y axis are in \AA . These plots shows the local density of electronic states in the horizontal plane 4\AA above the surface. In rough correspondence with the experimental bias conditions, we summed the density of conduction band states from E to $(E + eV)$ eV above the Fermi level. The colour scale indicates $\frac{\text{(number of electronic states)}}{(\text{\AA})^3}$	89

- 6.3 Contour plots of the spatially resolved density of electronic states of the Sr adatom model surface structures. Scales in the axis are in Å. The density of states was integrated in an energy window that corresponded to the experimental bias voltage. The value of the LDOS for the contour level at the surface is $1 \times 10^{-8} \frac{\text{(number of electronic states)}}{\text{Å}^3}$ in correspondence with the experimental tunnelling current[90]. Surfaces are denoted as follows: (1) $(\sqrt{13} \times \sqrt{13}) \theta = 0.0769$ (2) $c(4 \times 4) \theta = 0.125$ (3) $(\sqrt{5} \times \sqrt{5}) \theta = 0.20$ (4) $(2 \times 2) \theta = 0.25$ 90
- 6.4 Calculated density of states for bulk SrTiO₃ and the Sr adatom surface reconstructions involved in the phase transition. All the density of states are divided by the number of atoms in each supercell. As before, the surfaces are denoted as follows: (0) $(1 \times 1)\text{TiO}_2$ -terminated (1) $(\sqrt{13} \times \sqrt{13}) \theta = 0.0769$ (2) $c(4 \times 4) \theta = 0.125$ (3) $(\sqrt{5} \times \sqrt{5}) \theta = 0.20$ (4) $(2 \times 2) \theta = 0.25$. The vertical dashed line indicates the Fermi level, which is set at the zero of energy. All the surface reconstructions are metallic ones. 91
- 6.5 STM image ($2V$ bias voltage, $0.5nA$ tunnelling current) of the (2×1) reconstructed surface [36]. By averaging vertically through the image a plot of the average row heights is created as shown in the lower panel. The typical corrugation height is between 0.4 and 0.5 Å. 94
- 6.6 Calculated density of states for the (2×1) surface reconstructions 95
- 6.7 Contour plots of the spatially resolved density of states and electronic density in the model proposed by Erdman *et al* [15] for the (2×1) surface reconstruction. Scales in the axis are in Å. The density of states was integrated in an energy window of $2.3eV$ above the conduction band edge. Figure (a) shows a top view of $n(\mathbf{r})$ in a plane parallel to the surface that is 2 Å above the topmost atom on the relaxed surface structure. Figures (b) and (c) show the electronic density and the density of states for a slice running along the length of the rectangular unit cell showed in Figure (5.9b). Figures (d) and (e) show the same, but for a slice running along the width of the aforementioned rectangle. 97

- 6.8 Contour plots of the spatially resolved density of states and electronic density in the model proposed by me for the (2×1) surface reconstruction. Scales in the axis are in Å. The density of states was integrated in an energy window to 2.3 eV above the conduction band edge. Figure (a) shows a top view of $n(\mathbf{r})$ in a plane parallel to the surface that is 2Å above the topmost atom on the relaxed surface structure. Figures (b) and (c) show the electronic density and the density of states for a slice running along the length of the rectangular unit cell showed in Figure (5.9a). Figures (d) and (e) show the same, but for a slice running along the width of the aforementioned rectangle. 99
- 6.9 Contour plots of the spatially resolved density of states and electronic density in the model proposed by Castell [11] for the (2×1) surface reconstruction. Scales in the axis are in Å. The density of states was integrated in an energy window to 2.3 eV above the Fermi energy. (a) a top view of $n(\mathbf{r})$ in a plane parallel to the surface that is 3Å above the topmost atom on the relaxed surface structure. (b)-(c) the electronic density and the density of states for a slice running along the length of the rectangular unit cell showed in Figure (5.9a), (d) (e) the same but for a slice running along the width of the aforementioned rectangle. 101
- 6.10 Top view of the $(\sqrt{2} \times \sqrt{2}R45^\circ)$ surface reconstruction. 102
- 6.11 Contour plots of the spatially resolved density of electronic states of the Sr adatom model for the (2×1) surface reconstruction. Scales in the axis are in Å. The density of states was integrated in an energy window to 2.3 eV above the Fermi level. (a) a top view of $n(\mathbf{r})$ in a plane parallel to the surface that is 4Å above the topmost atom on the relaxed surface structure. (b)-(c) the electronic density and the density of states for a slice running along the length of the rectangular unit cell shown in Figure (5.9b), (d)-(e) the same, but for a slice running along the width of the aforementioned rectangle. . . 103
- 6.12 (a) Top view of the simulated STM image for the $\text{TiO}_2\text{-DL1}$ model of the (2×1) reconstruction. (b) a closer view of the experimentally observed STM image of the (2×1) reconstruction. 104

6.13	Contour plots of the spatially resolved density of electronic states of the TiO ₂ -DL1 model for the (2×1) surface reconstruction. The density of states was integrated in an energy window to 2.3 eV above the conduction band edge. Scales in the axis are in Å. (a) a top view of $n(\mathbf{r})$ in a plane parallel to the surface that is 2 Å above oxygens O1. (b)-(c) the electronic density and the density of states for a slice running along the dotted line shown in Figure (6.10). (d)-(e) the same, but for a slice running along the dash-dotted line in Figure (6.10)	105
6.14	STM images of the c(4×2) reconstruction observed by Castell [11]. In (a) (0.87 V bias, 0.15 nA current) the top of the image contains one spot per c(4×2) unit cell similar to the image from another region shown in (b) (0.2 V bias, 0.1 nA current). After a tip change indicated by arrows half way through the image in (a) two spots per unit cell are seen. This is also observed in a different region as shown in (c) (0.25 V bias, 1 nA current). Sometimes a mixture of the two images in (b) and (c) is observed as shown in (d) (0.45 V bias, 0.44 nA current). The c(4x2) unit cells are indicated in (b-d). Note that the crystallographic directions in (a) are rotated by 45° relative to (b-d).	107
6.15	Calculated density of states for the c(4×2) surface reconstructions	108
6.16	Lateral views for the DL-TiO ₂ -A proposed model for the c(4×2) surface reconstruction. Scales on the axis are in Å. The topmost contours in Figures (6.16b), (6.16d) and (6.16f) are representing constant density of states' values of $1 \times 10^{-7} \frac{\text{number of states}}{\text{Å}^3}$. This is the value we need for the experimental tunnelling current to be of the order of 0.1 nA[90].	109
6.17	Top view c(4×2) DL-TiO ₂ -A. Bias voltage: 2 V	110
6.18	Top view of the DL-TiO ₂ -A model for the c(4×2) reconstruction. Bias voltage: 0.87 V. Scales in the axis are in Å.	111
6.19	Top view c(4×2) DL-TiO ₂ -B. Bias voltage: 2 V. Scales in the axis are in Å.	112
6.20	Lateral views for the DL-TiO ₂ -B proposed model for the c(4×2) surface reconstruction. The topmost contours in Figures (6.20b), (6.20d) and (6.20f) represent constant density of states' values of $1 \times 10^{-7} \frac{\text{number of states}}{\text{Å}^3}$. This is the value we need for the experimental tunnelling current to be of the order of 0.1 nA[90]. Scales in the axis are in Å.	113
6.21	Top view c(4×2) Kubo and Nozoye[12]. Bias voltage: 0.7 V. Scales in the axis are in Å.	114

- 6.22 Top and lateral views $c(4\times 2)$ Kubo and Nozoye[12]. Bias voltage: $0.7V$. The topmost contour in Figure (6.22b), is representing a constant density of states' value of $3 \times 10^{-8} \frac{\text{numberofstates}}{\text{\AA}^3}$. This is the value we need for the experimental tunnelling current to be of the order of $0.03nA$ [90]. Scales in the axis are in \AA . . 115
- 6.23 Top and lateral views of the SL-TiO₂ model for the $c(4\times 2)$ reconstruction proposed by Castell [11]. The experimental bias voltage was $2V$. The topmost contours in Figures (6.23b) and (6.23d) represent constant density of states' values of $1 \times 10^{-7} \frac{\text{numberofstates}}{\text{\AA}^3}$. This is the value we need for the experimental tunnelling current to be of the order of $0.1nA$ [90]. Scales in the axis are in \AA . . 116

List of Tables

2.1	Dependence of the ordering of SrTiO ₃ surfaces on the initial surface treatments. The pristine surface was obtained from a SrTiO ₃ single crystal that was first mechanically and then mechano-chemically polished with an alkaline solution containing colloidal silica particles. The O ₂ annealed surface was annealed at 1100°C in flowing oxygen for three hours in a clean quartz tube[8].	21
2.2	Summary of the experimental results obtained by different groups on SrTiO ₃ (001) surface structures.	23
2.3	Experimental structural relaxations for the SrTiO ₃ (001) TiO ₂ terminated surface. In the MEIS measurements, the positions of the second layer Sr atoms were taken as the origin by the authors.	25
2.4	Experimental structural relaxations for the SrTiO ₃ (001) SrO terminated surface.	26
2.5	Theoretical atomic displacements along the z direction and structural relaxations for the SrTiO ₃ (001) TiO ₂ terminated surface. Positive displacements correspond to a displacement towards the vacuum.	29
2.6	Theoretical atomic displacements along the z direction and structural relaxations for the SrTiO ₃ (001) SrO terminated surface. Positive displacements correspond to a displacement towards the vacuum.	30
3.1	Maximum vibrational contributions to the surface free energy for different surfaces. In the case of PdO, this maximum corresponds to more than one surface termination, namely: PdO(001), PdO(100) PdO(101), PdO(110) and PdO(111).	38
3.2	Structural parameters for several oxides. <i>exp</i> stands for experimental and <i>cal</i> for calculated. Except where specified, all the experimental results are from [54]. . .	43
3.3	Coefficients in expression (3.26) [36]	44
4.1	Reference configuration and cutoff radii (in Bohr) of the pseudopotentials used in our study[74].	55

4.2	Results obtained for the lattice constant (a), bulk modulus (B) and elastic constants (C_{44} and C') of bulk SrTiO ₃ compared with existing results obtained from experiment [76], full-potential linear muffin tin orbitals method (FP-LMTO)[26] and the pseudo-potential plane waves method (PWP) [70]	57
4.3	Γ_{TiO_2} and Γ_{O} for the slabs representing the different (1×1) and (2×1) surface structures. $A_s^{(1\times 1)}$ is the area of one of the surfaces of a (1×1) terminated slab.	60
5.1	N_{SrO} , Γ_{TiO_2} and Γ_{O} for the slabs representing the different surface structures. $A_s^{(1\times 1)}$ is the area of one of the surfaces of a (1×1) terminated slab. θ_{Sr} is the coverage of Sr in the adatom model and T^E is the experimental temperature at which the surface reconstruction was observed in [12].	66
5.2	Labelling for the different surface reconstructions involved in the structural surface phase transitions.	67
5.3	Calculated Sr adsorption energies involved in the surface phase transitions.	67
5.4	Γ_{TiO_2} and Γ_{O} for the slabs representing the different surface structures. $A_s^{(1\times 1)}$ is the area of one of the surfaces of a (1×1) terminated slab. (2×1) TiO ₂ -DL1 labels the $(\sqrt{2} \times \sqrt{2})R45^\circ$ reconstruction.	81
6.1	Experimental tunnelling currents and bias voltages for the Sr adatom surface reconstructions. These are the reconstructions involved in the phase transitions depicted in Figure (5.2).	92
6.2	Experimental tunnelling currents and bias voltages for the (2×1) surface reconstructions. The reconstructions proposed by Erdman[15, 16] and Kubo and Nozoye[12] were not observed by STM.	96
6.3	Experimental tunnelling currents and bias voltages for the c(4×2) surface reconstructions. The reconstructions proposed by Erdman[16] were not observed by STM.	108
6.4	Brief summary of results on the simulated STM images.	117
8.1	Values for the frequencies in the Einstein model.	127

Chapter 1

Introduction

The surfaces of the perovskite of ABO_3 type are of interest for basic research as well as due to their technological applications. Among these materials, $SrTiO_3$ has attracted special attention and is generally regarded as a model substance for the perovskite group. $SrTiO_3$ is a particularly useful material for surface studies since it does not exhibit a domain structure which influences the topography of the surfaces; it is paraelectric and maintains the simple cubic crystal structure for a wide temperature range.

$SrTiO_3$ has been used extensively as a substrate for the growth of high T_c superconducting thin films [1] or hetero-structures [2]. More recently, it has also been tested as a candidate for crystalline gate dielectric in silicon-based devices [3], and as a buffer material for the growth of GaAs on Si [4]. The (100) surface of $SrTiO_3$ is probably the most thoroughly studied surface of all the perovskite [5, 6]. We might think of the ideal crystal in the [001] direction as made up from a stack of alternating TiO_2 and SrO layers, so that two non-polar bulk terminations of this crystal are possible: the (1×1) - TiO_2 surface and the (1×1) SrO surface, which are shown in Figure (1.1). Normally, the vacuum-fractured surface exposes fragments of both surfaces, but special treatment can provide atomically smooth surfaces of either type [7]. However, if we change the *environmental* parameters (pressure, temperature and oxygen partial pressure), titanium ions in the crystal can exhibit different valences and coordination numbers, so the surface structure is actually more complex than the aforementioned (1×1) . Depending upon the experimental environment, under oxidative conditions (2×1) , (4×2) and (6×2) surface reconstructions of $SrTiO_3$ have been reported [8, 9, 10], together with more complicated structures obtained by annealing in vacuum under reducing conditions [11, 12, 13]. The main experimental techniques used to study the aforementioned geometries in the surface structures were scanning tun-

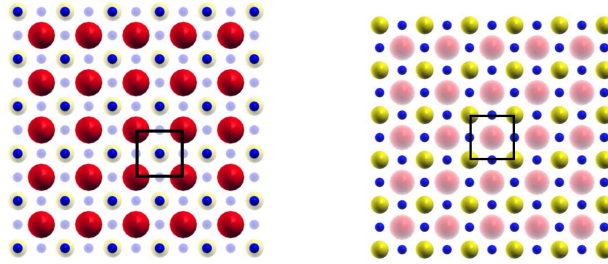


Figure 1.1: The two possible (1×1) surface terminations for $\text{SrTiO}_3(001)$: SrO termination is on the left and TiO_2 termination is on the right.

nelling microscopy (STM) [10, 11, 12, 13], low energy electron diffraction (LEED) [8, 10], reflection high-energy electron diffraction (RHEED)[9], grazing incidence X-ray diffraction (GIXD)[14] and a combination of high resolution electron microscopy with theoretical direct methods [15, 16]. Figure (1.2) shows a STM image of the (2×1) surface reconstruction. In figure (1.3) we have a STM image of the $c(4 \times 2)$ surface reconstruction. Figure (1.3)(b) shows an atomic resolution STM image where we can see two $c(4 \times 2)$ domains with their corresponding unit cells. Figures (1.2)(c) and (1.3)(b) are examples of the sort of periodic arrangement of bright spots we have to understand in terms of a thermodynamically stable atomic structure. Several models have been proposed for these two particular surface reconstructions [11, 12, 15, 16]. However, in most cases the results are inconclusive and even contradictory. For instance, the creation of point defects for thermally reduced crystals (predominantly oxygen vacancies) has been extensively investigated [5, 6]. Also, the possibility of reconstruction due to ordering of the vacancies has been discussed and experimentally [17] and theoretically [18] examined. From the wide range of observed reconstructions no consistent picture of the effects of thermal treatment under reducing conditions has so far emerged. Thus, it is apparent for thermal reduction that the behaviour of the (001) surface of SrTiO_3 cannot be described by a single point defect model in terms of oxygen vacancies. This situation also applies to oxidising conditions.

All the previously stated shows part of the great variety of surface reconstructions that have been observed on $\text{SrTiO}_3(001)$. The scope of this thesis covers the study of the atomic scale models that were proposed to understand some of these surface reconstructions. In particular, we have focused on the models proposed for the (2×1) and $c(4 \times 2)$ surface reconstructions [11, 12, 15, 16] and on the set of surface phase transitions observed by Kubo

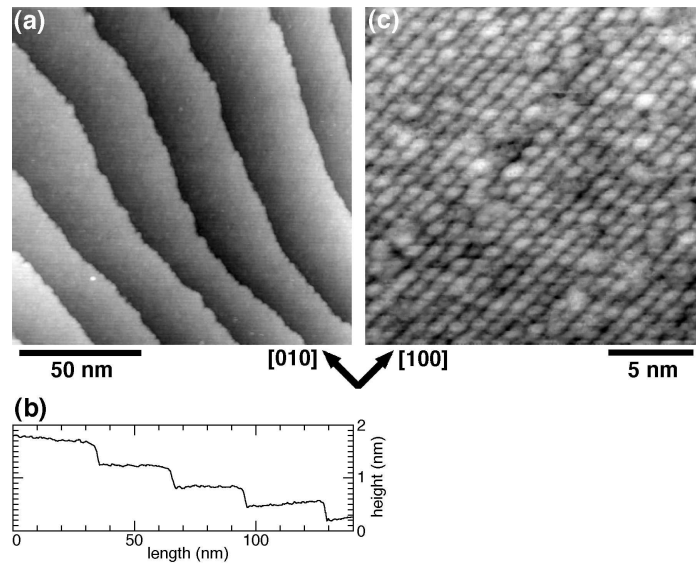


Figure 1.2: STM images of the (2×1) reconstructed surface obtained by Castell [11]. In figure (a) we can see that the surface morphology has wavy step edges. A horizontal line scan through the centre of (a) is displayed in (b) showing that the steps are 0.4 nm high which corresponds to one bulk unit cell. A high resolution image of one of the terraces (c) shows the 0.8 nm separation between the lines of the (2×1) reconstruction.

and Nozoye [12]. We have studied from first principles two newly proposed models for $\text{SrTiO}_3(001)$ surface reconstructions, the *Sr adatom model* [12] and the *Double layer model* [15]. To achieve this goal, we have used first principles *atomic scale thermodynamics*. The aforementioned technique links concepts and techniques from thermodynamics with results obtained from atomistic electronic structure theory.

Since most of the experimental evidence comes from Scanning Tunnelling Microscopy (STM), we have complemented the analysis with simulations of the STM images for the different surface reconstructions.

The aim of this dissertation is to answer which of the proposed models for each of the observed surface reconstructions is the most stable and reproduces the observed STM image.

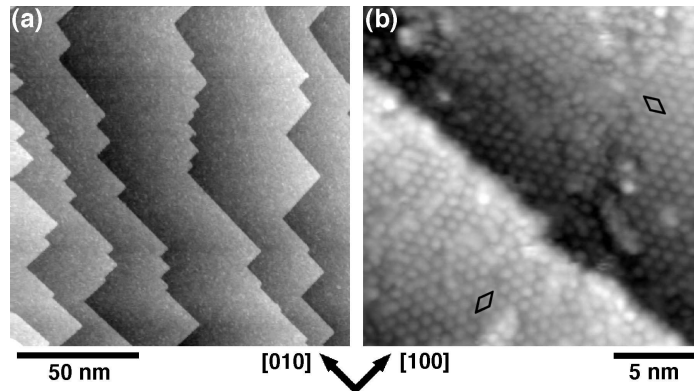


Figure 1.3: STM images of the $c(4\times 2)$ reconstructed surface obtained by Castell [11]. In figure (a) we can see that the surface morphology has straight step edges following the $\langle 010 \rangle$ and $\langle 100 \rangle$. The step height between terraces is 0.4 nm high which corresponds to one bulk unit cell. An atomic resolution image of one of the terraces (b) shows the two domains of the $c(4\times 2)$ reconstruction indicated by surface units cells.

1.1 Dissertation outline

In Chapter 2 we present a review of the experimental and theoretical studies that have been performed on the (001) surface of SrTiO_3 . Where possible, we contrast experimental results coming from different methodologies, as well as compare them with relevant theoretical studies. Finally, we discuss all this experimental and theoretical evidence to set up the groundwork over which our calculations and theoretical models are based.

Chapter 3 outlines the definition of atomic scale thermodynamics, and how to apply it to calculate the surface free energies of the different reconstructions observed on $\text{SrTiO}_3(001)$.

In Chapter 4 we present SIESTA, the code used to perform our total energy calculations. We briefly explain some of the fundamentals of SIESTA and how we built the basis set for each atom in the SrTiO_3 . Convergence tests, for the total energy vs the size of the slab and the number of vacuum layers, are presented. We also present our calculated values for the lattice constant, elastic constants, bulk modulus and equilibrium rotation angle for the antiferrodistortive transition of SrTiO_3 . All these values are compared with previous experimental and theoretical results. We show the calculated band structure for SrTiO_3 and compare it with previous band structure calculations. Finally, we present the first principles surface energy results obtained for the several candidate structures that cur-

rently exists for the (1×1) and (2×1) reconstructions. These results are compared with previous ones.

In Chapter 5 we use atomic scale thermodynamics to study the stability of the different models proposed to explain the observed $\text{SrTiO}_3(001)$ surface reconstructions. We pay special attention to the *Sr adatom models* and the *Double layer models* of each reconstruction. We compute the surface free energies, for each structural model, as a function of the environmental variables i.e., oxygen partial pressure and temperature.

Chapter 6 briefly outlines the theory of Scanning Tunnelling Microscopy. We explain how to simulate a STM image using first principles calculations and, for each surface reconstruction, compare these images with the experimental ones.

Chapter 7 summarises the results obtained so far and outline the direction for future work.

Chapter 2

Experimental and theoretical studies on SrTiO₃

2.1 Sample preparation, annealing conditions and surface science techniques

There are basically three preparation routes for SrTiO₃(001) surfaces: (a) treating the (001) polished crystal surface with a pH-controlled NH₄F-HF solution [7, 11, 12]; (b) by first mechanically and then mechanico-chemically polishing single crystals of SrTiO₃(001), which are later cleaned with organic solvents [8, 9, 15]; (c) by repeated cycles of Ar⁺ sputtering and annealing at 900K of commercially available single crystals of SrTiO₃(001) [19, 20]. The key point of procedure (a) is to achieve smoothness at atomic level in a TiO₂-terminated surface. The crystal structure of SrTiO₃ consists of alternating stacks of SrO and TiO₂ atomic layers (See Figure (2.1)). Because SrO is a basic oxide and TiO₂ is an acidic oxide, the selective dissolution of one of these layers may be achieved by a pH controlled solution. A buffered NH₄F-HF (BHF) with pH=4.5 can dissolve the SrO layer, leaving a terraced and atomically flat TiO₂-terminated surface. Figure (1.2) shows a STM image of a SrTiO₃(001) sample prepared this way and annealed in UHV for 30 min., at temperatures between 600 and 800°C. This methodology was used by Castell [11] and Kubo and Nozoye [12]. Samples from procedure (b) and (c) were pre-annealed: samples from (b) in flowing oxygen, and samples from (c) under an oxygen pressure of 9.86×10^{-10} atm.

The main advantage of methodology (a) is that it assures a well-known surface termination

to start with the annealing process. The pre-annealing process in procedures (b) and (c), which in the (c) case include argon sputtering, may induce a high density of defects, as well as a change of surface composition. As the final surface ordering depends sensitively on the state of the surface, even keeping the annealing conditions unchanged, different ordering can be expected if the surfaces received different treatments. Table (2.1) shows an example of this.

Starting surface	Temperature (°C)	Pressure (atm)	Duration (min)	Surface (LEED)
Pristine surface	950	$< 4.93 \times 10^{-11}$	120	(2×1)
O ₂ annealed	950	$< 4.93 \times 10^{-11}$	120	c(6×2)

Table 2.1: Dependence of the ordering of SrTiO_3 surfaces on the initial surface treatments. The pristine surface was obtained from a SrTiO_3 single crystal that was first mechanically and then mechano-chemically polished with an alkaline solution containing colloidal silica particles. The O₂ annealed surface was annealed at 1100°C in flowing oxygen for three hours in a clean quartz tube[8].

With regard to the annealing conditions and the experimental techniques used, Table (2.2) presents a summary of the large number of studies that have been performed in an effort to understand surface structure variations in $\text{SrTiO}_3(001)$ under different experimental conditions. As we can see from Table (2.2), the results obtained by different research groups are sometimes contradictory, and only a few of the studies have attempted to support their results with models for the surface structures. Liang and Bonnell [21] observed that upon UHV annealing, a rearrangement of surface atoms resulted in the formation of row-like structures with spacings of 12 and 20 Å. The authors proposed two structural reorganisation mechanisms: (1) the formation of new phases on the surface upon reduction, accompanied by changes in the composition and geometry of the surface; and (2) an alteration of the surface morphology due to reordering of oxygen vacancies. Based upon the observed spacings they attributed the observed surface to an SrO-rich surface with the formation of the so-called Ruddlesden-Popper phases [22]. This conclusion was based on an assumption of different sublimation rates for Sr, Ti and O at the surface, i.e. TiO_x has a higher sublimation rate than SrO at high temperatures in vacuum. A more recent AFM study by Szot et al [23] suggested that oxidation above 900°C can also cause the $\text{SrTiO}_3(001)$ surface to become SrO-rich, albeit without chemically characteris-

ing the surface. These conclusions were based on measurements of step heights from AFM images. The authors proposed that under oxidising conditions at high temperatures, the near-surface region reconstructs via dismantling, transport and intercalation of SrO layers combined with a crystallographic shearing mechanism. Jiang and Zegenhagen [8, 10] used STM and LEED and observed a well-ordered and atomically flat surface after annealing in vacuum at different temperatures. Further observations showed the existence of domains rotated by 90° with respect to one-another as well as the formation of single unit cell height steps on the surface. In the same experiment a change in Auger peak intensity ratios (O-to-Ti and Sr-to-Ti) was observed for the (2×1) , $c(4 \times 2)$ and $c(6 \times 2)$ surface structures. These results show that the reconstructions with larger size unit cells tend to be richer in Ti. Formation of $\text{Sr}_{n-1}\text{Ti}_n\text{O}_{3n-1}$ -type phases on the surface was suggested as a possible explanation of the features and periodicities obtained in STM images. The authors also proposed that two competing processes -bulk oxygen diffusion and oxygen desorption from the surface- determine the final structure of the surface. Castell [11, 24] used the chemical etching methodology described at the beginning of this section, in some cases combined with argon ion sputtering and subsequent UHV annealing to obtain (2×1) , $c(4 \times 2)$ and (6×2) structures on the $\text{SrTiO}_3(001)$ surface. The surface, inspected by LEED and STM, showed large surface steps with 0.4 nm step height. The structural models proposed by the author were based on a qualitative interpretation of the STM images. These models are modifications of the (1×1) TiO_2 -terminated surface and we have performed total energy calculations for all of them. No surface chemical probes (like coaxial impact collision ion scattering spectroscopy [11]) were reported that could provide definitive evidence for the proposed surface models. Castell rejected the idea that impurity segregation (from the Nb-doped SrTiO_3 samples) is a governing factor in the formation of various SrTiO_3 surface structures. Kubo and Nozoye [12] have also used the chemical etching methodology. Inspecting the surface by STM, they reported almost every observed surface reconstruction on $\text{SrTiO}_3(001)$ and proposed a new model to explain what they saw: the Sr adatom model. In this dissertation we study this model in detail, and a more detailed analysis of Kubo and Nozoye findings will be given in the following sections.

2.2 Relaxation of the (1×1) unreconstructed surface

The SrTiO_3 crystal viewed in the $[001]$ direction comprises a stack of alternating TiO_2 and SrO layers, so that two charge neutral (001) bulk terminations of this crystal are possible:

Reconstruction	Sample preparation	Technique
(1×1)	(1)UHV annealing, T=826.85 °C, 60 min [8, 21, 25] (2)Annealing in 9.86×10^{-9} atm O_2 [25]	AES [8], AFM [25] STM [21], RHEED [25]
(2×1)	(1)UHV annealing, T=950 °C, 120 min[8] (2)UHV annealing, T=600-800 °C, 30 min[8, 11] (3)Ar ion sputtering + Annealing in an O_2 flow, T=950-1000 °C.	LEED, STM [8, 11] AES [8] HREM+direct methods [15]
(2×2)	(1)Annealing in 10×10^{-9} atm O_2 [25]	MEIS [25]
c(4×2)	(1)UHV annealing in 9.86×10^{-9} atm H_2 , T=950 °C, 120 min [8] (2)Ar ion sputtering + UHV annealing, T=1200 °C 30 min [11] (3)Ar ion sputtering + UHV annealing, T=839-950 °C [16]	LEED, STM [8, 11] AES [8] HREM+direct methods [16]
c(4×4)	(1)UHV annealing, T=1100 °C, ≈ 1 min [12]	STM [12]
c(6×2)	(1) O_2 annealing, T=1100 °C, 90 min; followed by UHV annealing, T=950 °C, 120 min [8]	LEED, AES, STM [8]
(6×2)	(1)Ar ion sputtering + UHV annealing, T=870-975 °C 20-10 min [11]	LEED, STM[24]
($\sqrt{5} \times \sqrt{5}$)R26.6°	(1)UHV annealing, T=900 °C, 15h; then flashing at T-1200 °C, 2 min [17] (2)UHV annealing, T=1200 °C, several seconds [13]	RHEED, XPS, STM, LEED [17] STM, NC-AFM [13]
($\sqrt{13} \times \sqrt{13}$)R33.7°	(1)UHV annealing, T=1250 °C, several seconds [12]	STM [12]

Table 2.2: Summary of the experimental results obtained by different groups on $\text{SrTiO}_3(001)$ surface structures.

the SrO surface and the TiO_2 surface, which were presented in Figure(1.1).

The relaxation parameters used to characterise the surfaces were defined differently by different authors. We adopted the parameters proposed by Bickel and coworkers [20] and translated the results obtained by other groups into this notation to ease the comparison among them. In Bickel's notation the atomic displacements δz are defined such that a positive displacement denotes a movement towards the vacuum. The change in spacing between atomic layers i and j (Δd_{ij}) is given by the expression

$$\Delta d_{ij} = \delta z^{M_i} - \delta z^{M_j} \quad (2.1)$$

where M_i denotes the metal atom in layer i . The relative displacements of the oxygen and metal atoms within the i th atomic layer is given by the so called buckling parameter s_i , which is defined as

$$s_i = \delta z^{O_i} - \delta z^{M_i}. \quad (2.2)$$

Parameters Δd_{ij} and s_i are given as percentages of the interlayer spacing d_0 . These parameters are shown schematically in Figure (2.1).

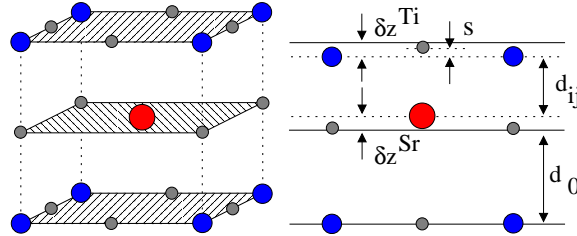


Figure 2.1: The left picture shows the ideal SrTiO_3 crystal in the $\langle 001 \rangle$ direction. The alternating TiO_2 and SrO layers are clearly seen. The picture on the right shows a schematic diagram of the relaxation parameters. Sr is red, Ti is blue and O is grey. This figure was taken from [26].

2.2.1 Review of experimental literature

The relaxation of the unreconstructed (1×1) surface of $\text{SrTiO}_3(001)$ has been investigated using various experimental techniques, namely: medium energy ion scattering (MEIS)[25], low energy electron diffraction (LEED)[20], surface X-ray diffraction (SXRD)[19] and reflection high energy electron diffraction (RHEED)[27]. Results for the TiO_2 and SrO

terminations are summarised in tables (2.3) and (2.4).

TiO ₂ terminated				
Atomic displacements (Å)	LEED[20]	RHEED[27]	MEIS[25]	SXRD[19]
δz^{Ti_1}	-	-	0.02±0.01	0.00±0.03
δz^{O_1}	-	-	0.08±0.01	-0.50±0.30
δz^{Sr_2}	-	-	-	-0.01±0.01
δz^{O_2}	-	-	-	0.20±0.10
$s_i = \delta z^{O_i} - \delta z^{M_i}$	LEED[20]	RHEED[27]	MEIS[25]	SXRD[19]
s_1 (Å)	0.08±0.08	0.10	0.06±0.02	-0.50±0.33
s_1 (%)	4±4	5.1	3.1±1.0	-26±17
s_2 (Å)	-	-	-	0.21±0.11
s_2 (%)	-	-	-	11±6
$\Delta d_{ij} = \delta z^{M_i} - \delta z^{M_j}$	LEED[20]	RHEED[27]	MEIS[25]	SXRD[19]
Δd_{12} (Å)	0.04±0.04	0.07	0.02±0.01	0.01±0.04
Δd_{12} (%)	2±2	3.6	1±0.5	0.5±2.0
Δd_{23} (Å)	0.04±0.04	0.05	-	-
Δd_{23} (%)	-2±2	2.6	-	-

Table 2.3: Experimental structural relaxations for the $\text{SrTiO}_3(001)$ TiO₂ terminated surface. In the MEIS measurements, the positions of the second layer Sr atoms were taken as the origin by the authors.

The reported LEED measurements in tables (2.3) and (2.4) were carried out by Beckel *et al.* [20]. A sharp LEED pattern confirmed the (1×1) geometry of the surface.

Several structural parameters were used to fit theoretical data to their experimental data. These parameters included interlayer spacing Δd_{12} and Δd_{23} , first layer's buckling (as defined in equation 2.2) and the ratio between the two types of termination. The data are obtained through *multiple scattering* computational methods. The objective of these methods is to provide an adequate description of the multiple scattering mechanisms affecting the incident electrons in their path inside the crystal. The agreement between experimental and theoretical data measures the correctness of the computational method. An example of the quality match possible is given in Figure (2.2), where a comparison of experimental and theoretical spectra is shown for the $\text{Si}(111)-(\sqrt{3} \times \sqrt{3})\text{-R}30^\circ$. To optimise and assess experiment-theory comparisons a number of reliability factors were proposed. Among them, there is the method proposed by Pendry [29], which is the one used by Bickel and coworkers. The Pendry factor gives a measure of how well the proposed structures fit

SrO terminated			
Atomic displacements (Å)	LEED[20]	RHEED[27]	SXRD[19]
δz^{Sr_1}	-	-	-0.25 ± 0.07
δz^{O_1}	-	-	-0.3 ± 0.4
δz^{Ti_2}	-	-	-0.24 ± 0.07
δz^{O_2}	-	-	-0.4 ± 0.7
$s_i = \delta z^{O_i} - \delta z^{M_i}$	LEED[20]	RHEED[27]	SXRD[19]
s_1 (Å)	0.16 ± 0.08	0.16	-0.05 ± 0.47
s_1 (%)	8 ± 4	8.2	2.6 ± 24.1
s_2 (Å)	-	-	-0.16 ± 0.77
s_2 (%)	-	-	-8.2 ± 39.4
$\Delta d_{ij} = \delta z^{M_i} - \delta z^{M_j}$	LEED[20]	RHEED[27]	SXRD[19]
Δd_{12} (Å)	-0.20 ± 0.04	0.10	-0.01 ± 0.14
Δd_{12} (%)	-10 ± 2	5.1	-0.51 ± 7.2
Δd_{23} (Å)	0.08 ± 0.04	0.05	-0.26 ± 0.11
Δd_{23} (%)	4 ± 2	2.6	-13.3 ± 5.6

Table 2.4: Experimental structural relaxations for the SrTiO₃(001) SrO terminated surface.

the experimental data. Depending on the values of the aforementioned interlayer spacings and surface buckling, Bickel *et al.* calculated 588 trial structures for each SrTiO₃(001)-(1×1) surface termination. As every structure has to be combined with each other, a total of about 3.5×10^5 Pendry factor calculations were performed. The best fit structure was obtained for a 1:1 mixture of both terminations with a Pendry factor $R_P = 0.53$. However, the authors pointed out that the structure found could be refined by additional structural variations. The reconstruction may extend also to deeper layers and the assumed 1:1 mixture of terminations is only an approximation.

Hikita *et al.* studied the relaxation of the SrTiO₃(001) surface using RHEED. They prepared the TiO₂-terminated surface by cleaning the supplied SrTiO₃ samples with a Bi deposition/desorption cleaning method [30]. The cleaning was followed by further oxidation in NiO₂ for one hour, with a pressure of 1×10^{-4} Pa and a temperature of 673 K. The SrO terminated surface was prepared by depositing a monolayer of SrO on the TiO₂ terminated surface [27]. The authors claim they had pure TiO₂ and SrO (1×1) terminations. RHEED experimental data were fitted using interlayer spacing Δd_{12} and Δd_{23} and the first layer's buckling as parameters. The structure was optimised to give the minimum R_P factor. The discrepancy in values of Δd_{12} , Δd_{23} and buckling, compared to the values

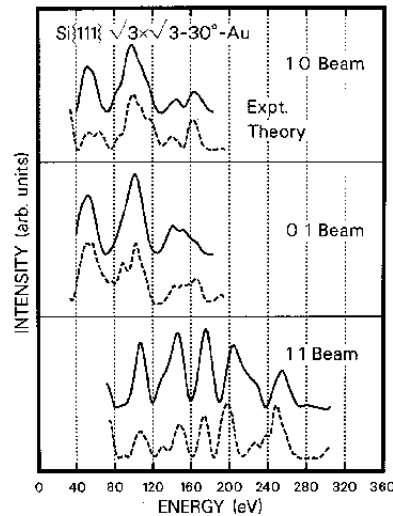


Figure 2.2: Comparison of experimental and theoretical 10, 01 and 11 beams LEED intensity-energy spectra for a $\text{Si}(111)-(\sqrt{3} \times \sqrt{3})\text{-R}30^\circ$ surface[28].

obtained by Bickel *et al.*, was attributed to the difference in surface preparation.

Charlton *et al* studied the $\text{SrTiO}_3(001)$ surface using SXRD. Again the experimental data were fitted to theory. The fitting was performed using 19 parameters, including atomic displacements parameters, buckling parameters and a parameter to describe the fraction of each type of surface termination. The best fit was obtained for a surface which was 78% TiO_2 terminated and 22% SrO terminated.

The surface relaxation of the TiO_2 terminated surface was investigated by Nishimura *et al.* [25] using MEIS and RHEED. They prepared their samples using a chemical etch to remove SrO termination, obtaining a surface $88 \pm 2\%$ TiO_2 terminated.

From the previously stated there is a large disagreement between the experimental results. These disagreements could arise from differences in surface preparation techniques [27] and from approximations in the theoretical analysis of the results. Hikita *et al.*, Charlton *et al.* and Bickel *et al* all used a fitting procedure to find the optimum structure that corresponds to the observed experimental data. These experiment-theory comparisons are assessed using reliability factors, such as the aforementioned Pendry factor or the one

proposed by Zanazzi and Jona [31]. Although these factors do provide a more quantitative and objective basis for structure optimisation, the criteria on which they are based remain essentially arbitrary [32]. Besides, as Johnston [26] pointed out, it is a cause of concern when a mixture of different terminations is used in the fitting of a structure to experimental data. If two terminations are simultaneously present, the surface cannot be in equilibrium with any bulk or solid phases because the equilibrium condition implies that the surface reconstruction with the lowest Gibbs free energy would eliminate the other. However, two surface terminations are possible if the surface was decoupled from equilibrium with the bulk and vapour phases, or if the sample was quenched during transformation between two equilibrium surface reconstructions [26].

2.2.2 Review of theoretical literature

Compared with the experimental results, DFT calculations of the atomic relaxations of $\text{SrTiO}_3(001)$ showed better agreement with each other than the experimental results. Results for the TiO_2 -terminated and SrO -terminated surface are showed in tables (2.5) and (2.6).

The results from Padilla and Vanderbilt [33] were obtained using an ultrasoft pseudopotential calculation with a plane wave basis and the LDA approximation. They used a slab with 7 atomic layers and three vacuum layers. They observed the largest relaxations for the metal atoms in the surface layer, -5.7% and -3.4% for the SrO -terminated and TiO_2 -terminated surfaces respectively. On the other hand, the displacement of the oxygen atoms from their bulk positions was very small. They observed a substantial contraction of the interlayer spacing Δd_{12} for both surface terminations and a notable outward relaxation of the second layer in the TiO_2 -terminated surface.

The other set of Plane-Waves Pseudopotential calculations we show here was performed by Cheng *et al* using the CASTEP code [34]. The surfaces were simulated using slabs with eleven atomic layers and four layers of vacuum. According to the authors, the small differences between their results and the ones reported by Padilla and Vanderbilt [33], observed in tables (2.6) and (2.5), were due to employing different pseudopotentials in each case.

As in this work, Zhang and Demkov [35] used SIESTA, a pseudopotential code using a local basis of atomic orbitals within the LDA approximation, and slabs of seven atomic

Method Ref.	PWP		SIESTA		FP-LMTO
	[33]	[34]	Present	[35]	[26]
Atomic displacements (Å)					
δz^{Ti_1}	-0.131	-0.07	-0.09	-0.1	-0.1241
δz^{O_1}	-0.062	-0.01	-0.02	-0.04	-0.0689
δz^{Sr_2}	0.097	0.18	0.15	0.18	0.0906
δz^{O_2}	-0.019	0.03	0.04	0.06	-0.0235
δz^{Ti_3}	-0.027	-0.01	-	-	-0.0247
δz^{O_3}	-0.019	0.01	-	-	-0.0204
δz^{Sr_4}	-	0.04	-	-	-
δz^{O_4}	-	0.01	-	-	-
Surface rumpling (Å) $s_i = \delta z^{\text{O}_i} - \delta z^{\text{M}_i}$					
s_1	0.07	0.07	0.07	0.06	0.0552
s_2	-0.116	-0.15	-0.1	-0.12	-0.1141
s_3	0.008	0.016	-	-	0.0043
s_4	-	-0.026	-	-	-
Change in interlayer spacing $\Delta d_{ij} = \delta z^{\text{M}_i} - \delta z^{\text{M}_j}$					
$\Delta d_{12}(\text{Å})$	-0.228	-0.25	-0.3	-0.28	-0.2147
(%)	-11.8	-12.8	-15.5	-14.3	-11.2
$\Delta d_{23}(\text{Å})$	0.12	0.19	0.27	-	0.1153
(%)	6.2	9.4	6.88	-	6.0
$\Delta d_{34}(\text{Å})$	-	-0.05	-	-	-
(%)	-	-2.2	-	-	-

Table 2.5: Theoretical atomic displacements along the z direction and structural relaxations for the SrTiO_3 (001) TiO_2 terminated surface. Positive displacements correspond to a displacement towards the vacuum.

layers. They found that surface layer Sr and Ti atoms relax inwards towards the bulk, Sr atoms having the largest displacement. Although the agreement between our results and the ones proposed by Zhang *et al.* is very good, differences of $\approx 10^{-2}$ (Å) do exist. The main reason for these discrepancies may be due to the fact that, for the relaxation process, Zhang and Demkov used a force tolerance of $0.02 \text{ eV}/\text{Å}$ while we used $0.005 \text{ eV}/\text{Å}$.

Johnston[26] used the full-potential linear combination of muffin-tin orbitals (FP-LMTO) method to study the $\text{SrTiO}_3(001)$ surfaces. This method implements DFT within the local density approximation (LDA). She used a supercell with seven atomic layers and three vacuum layers. For the TiO_2 -terminated surfaces, the author found that the surface Ti

Method	PWP		SIESTA		FP-LMTO
Ref.	[33]	[34]	Present	[35]	[26]
Atomic displacements (\AA)					
δz^{Sr_1}	-0.220	-0.26	-0.2	-0.17	-0.231
δz^{O_1}	0.004	0.04	0.03	0.02	-0.012
δz^{Ti_2}	0.046	0.07	0.06	0.05	0.025
δz^{O_2}	0.00	0.01	0.01	0.01	-0.018
δz^{Sr_3}	-0.046	-0.06	-	0.03	-0.047
δz^{O_3}	-0.004	0.01	-	0.06	-0.010
δz^{Sr_4}	-	0.01	-	-	-
δz^{O_4}	-	0.00	-	-	-
Surface rumpling (\AA) $s_i = \delta z^{\text{O}_i} - \delta z^{\text{M}_i}$					
s_1	0.224	0.30	0.23	0.19	0.219
s_2	-0.046	-0.06	-0.02	-0.04	-0.043
s_3	0.042	0.07	-	0.03	0.037
s_4	-	-0.01	-	-	-
Change in interlayer spacing $\Delta d_{ij} = \delta z^{\text{M}_i} - \delta z^{\text{M}_j}$					
$\Delta d_{12}(\text{\AA})$	-0.26	-0.33	-0.24	-0.22	-0.256
(%)	-13.8	-16.8	-12	-11.2	-13.3
$\Delta d_{23}(\text{\AA})$	0.10	0.14	0.06	0.02	0.072
(%)	4.8	6.9	3.2	1.0	3.74
$\Delta d_{34}(\text{\AA})$	-	-0.08	-	-	-
(%)	-	-3.9	-	-	-

Table 2.6: Theoretical atomic displacements along the z direction and structural relaxations for the SrTiO_3 (001) SrO terminated surface. Positive displacements correspond to a displacement towards the vacuum.

atoms moved towards the bulk while the rumpling in the surface layer was 0.0552 \AA , in good agreement with all the other theoretical results. As regards the Sr atoms in the second layer, these moved away from the bulk by 0.091 \AA , in excellent agreement with Padilla *et al* and in good agreement with the rest of the theoretical calculations. The rumpling in this second layer was -0.1141 \AA , in very good agreement with the rest of the published results. For the SrO-terminated surface one of the differences was in the displacement of the surface O atoms. The FP-LMTO method predicted an inwards displacement while all the other methods predicted an outwards displacement. Something similar happens with the O in the second layer: all the methods except FP-LMTO predicted an outwards displacement while FP-LMTO gave an inwards displacement. However, the rumpling for the first two

layers compares well with the other results.

Chapter 3

Thermodynamics

3.1 Atomic scale thermodynamics

Atomic scale thermodynamics is the methodology that studies how total energy electronic structure calculations can be linked with concepts from thermodynamics. In recent years, this methodology [36, 37, 38, 39, 40] has become an important strategy in structure stability analysis of complex surfaces and, in this chapter, we outline how to apply atomic scale thermodynamics to calculate surface free energies of different surface reconstructions.

As was described in Chapter 1, in this dissertation we are using DFT to describe the total energies. A typical DFT calculation output includes detailed information about the electronic structure (band structure). Here, we are specially interested in the total energy and in the stable atomic coordinates. By the Hellmann-Feynman theorem, the charge density obtained from a DFT calculation can be used to obtain the forces acting on the nuclei and hence, by relaxing the forces to zero, a stable configuration is obtained. In fact, what is typically called a stable surface in reality is the statistical average over all elementary adsorption processes from, and desorption processes to, the surrounding gas phase. When the total number of desorption processes (averaged over time) equals the number of adsorption processes, the average surface composition and structure will remain constant: the surface has attained its thermodynamic equilibrium with the environment.

The *atomic scale thermodynamics* approach is to screen a limited number of known (or proposed) surface structures and evaluate which of them turns out to be the most stable. In thermodynamical terms this means we have to compute the surface energy as a function of the environmental variables for each structural model. The one with the lowest surface

energy is identified as the most stable.

3.1.1 The formalism for the surface free energy

Our formulation of the surface free energy is based on Cahn's [41] which Finnis [42] generalised to crystalline interfaces and surfaces. We might think of surfaces as simpler systems where one of the crystalline species is replaced by vacuum, into which no diffusion is allowed. The system we consider here is an infinite slab in two dimensions ($x - y$), whose thickness in the z dimension is some tens of atomic planes, which is the kind of atomic system we simulate with SIESTA, only a certain area is used in the simulation, and periodic boundary conditions are used to represent the surface. The basic unit which is infinitely repeated all over the space is known as a *supercell*.

Our slab has, at most, a volume of $\approx 6.33 \times 10^{-27} m^3$, half of which is vacuum. For an ideal diatomic gas (we consider the oxygen to behave like one), the volume per molecule at $T = 1500$ K and $p = 1 \times 10^{-25}$ atm is $0.20 \times 10^{-22} \frac{m^3}{atom}$. Therefore, in the supercell vapour phase we would have approximately 0.0003 oxygen molecules and we can assume that this phase is well represented by the vacuum fraction within the supercell.

The interface area is A . The surface energy σ is the energy per unit area of surface and its general thermodynamic formula is

$$\sigma = \frac{1}{A} \left(G^{\text{slab}} - \sum_i \mu_i N_i \right) \quad (3.1)$$

G^{slab} denotes the total Gibbs free energy of the contents of the supercell, including the surface. A is the surface area of the slab within the supercell¹, the index i runs over all the component species (SrO, TiO₂ and O₂ in our case), μ_i are the chemical potentials of these species, N_i are the numbers of atoms of each species in the supercell and σ is the surface energy. For simplicity, we assume there is no strain.

Equation (3.1) suggests the interpretation of the surface energy as an excess Gibbs free energy due to the formation of the surface; i.e.: we can think of $\sum_i \mu_i N_i$ as the Gibbs free energy of a hypothetical bulk single phases containing the same components as there are in our system.

¹ $A = 2A_s$ where A_s is the area of each slab face.

Following the formulation proposed by Cahn [41], we define the “surface excess” of component i with respect to component 1, Γ_i as

$$\Gamma_i = \frac{1}{2A_s} \left(N_i - N_1 \frac{\nu_i^{\text{bulk}}}{\nu_1^{\text{bulk}}} \right). \quad (3.2)$$

where $\frac{\nu_i^{\text{bulk}}}{\nu_1^{\text{bulk}}}$ represents the number of atoms of component i in bulk phase for each atom of component 1 in the bulk phase. Recasting equation (3.1) in terms of excesses, we obtain

$$\sigma = \frac{1}{2A_s} \left(G^{\text{slab}} - \frac{N_1}{N_1^{\text{bulk}}} g^{\text{bulk}} \right) - \sum_{i \neq 1} \mu_i \Gamma_i. \quad (3.3)$$

N_1^{bulk} is the number of atoms of the reference species within an arbitrary representative quantity of the bulk phase and g^{bulk} is the free energy of that quantity.

For the particular case of SrTiO₃, we take a unit cell as a reference amount. Defining the components SrO, O₂ and TiO₂, we have $N_{\text{SrO}}^{\text{bulk}}=1$ and $N_{\text{TiO}_2}^{\text{bulk}}=1$. Defining SrO as the reference component for excesses leads us to the final expression for the surface energy we will use for strontium titanate:

$$\sigma = \frac{1}{2A_s} \left(G^{\text{slab}} - g_{\text{SrTiO}_3}^{\text{bulk}} N_{\text{SrO}} \right) - \mu_{\text{TiO}_2}^{\text{slab}} \Gamma_{\text{TiO}_2} - \mu_{\text{O}} \Gamma_{\text{O}}. \quad (3.4)$$

It is clear that we are dealing with a two-phase system. The system is composed of three components, namely: SrO, TiO₂ and O₂. According to the Gibbs phase rule there are therefore three degrees of freedom. We choose T , p_{O_2} and μ_{TiO_2} to be the so called *environmental parameters*. Within equilibrium conditions, the allowed range of values for these parameters represent all different thermodynamically accessible situations. In terms of these parameters, the above equation becomes

$$\begin{aligned} \sigma(\mu_{\text{TiO}_2}^{\text{slab}}, p_{\text{O}_2}, T) &= \frac{1}{2A_s} \left(G^{\text{slab}}(p_{\text{O}_2}, T) - g_{\text{SrTiO}_3}^{\text{bulk}}(p_{\text{O}_2}, T) N_{\text{SrO}} \right) - \\ &\mu_{\text{TiO}_2}^{\text{slab}}(p_{\text{O}_2}, T) \Gamma_{\text{TiO}_2} - \mu_{\text{O}}(p_{\text{O}_2}, T) \Gamma_{\text{O}}. \end{aligned} \quad (3.5)$$

Before going any further, it is necessary to discuss which approximations can be done in equation (3.5) to render this problem more tractable. For each atomic configuration in the supercell, we need to compute all the thermodynamic potentials entering into the expression for σ .

Clearly, the most expensive *ab initio* calculation is the one performed for the slab to

calculate $G^{\text{slab}}(p_{\text{O}_2}, T)$, which has an expanded mathematical expression² given by

$$G^{\text{slab}}(p_{\text{O}_2}, T) = E_{0K}^{\text{slab}} + F_{\text{Vib}}^{\text{slab}}(T) - TS_{\text{Config}}^{\text{slab}} + pV^{\text{slab}} \quad (3.6)$$

where $F_{\text{Vib}}^{\text{slab}}(T)$ is the Helmholtz vibrational contribution, defined as

$$F_{\text{Vib}}^{\text{slab}}(T) = E_{\text{Vib}}^{\text{slab}}(T) - TS_{\text{Vib}}^{\text{slab}}(T). \quad (3.7)$$

E_{0K}^{slab} is the total energy calculated from first principles, $S_{\text{Config}}^{\text{slab}}$ is the configurational entropy and V^{slab} is the volume of the supercell. In the same way, we can express $g_{\text{SrTiO}_3}^{\text{bulk}}$. The total Gibbs free energy of a certain amount N_{SrTiO_3} of bulk SrTiO₃ is given by

$$G_{\text{SrTiO}_3}^{\text{bulk}}(p_{\text{O}_2}, T) = E_{0K}^{\text{SrTiO}_3} + F_{\text{Vib}}^{\text{SrTiO}_3}(T) - TS_{\text{Config}}^{\text{SrTiO}_3} + pV_{\text{SrTiO}_3}^{\text{bulk}} \quad (3.8)$$

with

$$F_{\text{Vib}}^{\text{SrTiO}_3}(T) = E_{\text{Vib}}^{\text{SrTiO}_3}(T) - TS_{\text{Vib}}^{\text{SrTiO}_3}(T) \quad (3.9)$$

and $g_{\text{SrTiO}_3}^{\text{bulk}}(p_{\text{O}_2}, T) = \frac{G_{\text{SrTiO}_3}^{\text{bulk}}(p_{\text{O}_2}, T)}{N_{\text{SrTiO}_3}}$. Regarding $\mu_{\text{TiO}_2}^{\text{slab}}$, its value in the experimental conditions under which the observed surface structures were created or observed is not known. However, standard thermodynamics allows us to put bounds on this parameter.

We define the Gibbs formation energy of one formula unit of bulk SrTiO₃ with respect to TiO₂ and SrO as

$$\Delta G_{\text{f SrTiO}_3}(p_{\text{O}_2}, T) = g_{\text{SrTiO}_3}^{\text{bulk}}(p_{\text{O}_2}, T) - g_{\text{TiO}_2}^{\text{bulk}}(p_{\text{O}_2}, T) - g_{\text{SrO}}^{\text{bulk}}(p_{\text{O}_2}, T) \quad (3.10)$$

where $\Delta G_{\text{f SrTiO}_3}(p_{\text{O}_2}, T) < 0$. $g_{\text{SrTiO}_3}^{\text{bulk}}(p_{\text{O}_2}, T)$, $g_{\text{TiO}_2}^{\text{bulk}}(p_{\text{O}_2}, T)$, $g_{\text{SrO}}^{\text{bulk}}(p_{\text{O}_2}, T)$ are the Gibbs free energies of the bulk crystals per formula unit at (p_{O_2}, T) .

Considering the slab to be in equilibrium³

$$g_{\text{SrTiO}_3}^{\text{bulk}}(p_{\text{O}_2}, T) = \mu_{\text{SrO}}^{\text{slab}}(p_{\text{O}_2}, T) + \mu_{\text{TiO}_2}^{\text{slab}}(p_{\text{O}_2}, T). \quad (3.11)$$

Equation (3.11) constrains the chemical potentials of TiO₂ and SrO to the Gibbs free

²In this expression we consider the effect of T on the free energy of the electrons as negligible.

³The Gibbs free energy of n moles of A is $G_A(n, T, P)$. It is known that $G_A(n, T, P)$ is a homogeneous function of first degree in n . Therefore, $G_A(n, T, P) = n \frac{\partial G_A(n, T, P)}{\partial n} = n\mu(T, P)$, and $\mu(T, P) = \frac{G_A(n, T, P)}{n} = g_A(T, P)$.

energy per formula unit of SrTiO_3 and, ignoring the small deviation from stoichiometry that must be present, this implies that only one of these chemical potentials (TiO_2 in our case) is an independent degree of freedom. Nevertheless, this freedom is limited. It is known that the chemical potential of TiO_2 or SrO in the SrTiO_3 cannot be above that of the bulk phase; in such a case, the SrTiO_3 slab would decompose into TiO_2 and SrO . In formulae

$$\begin{aligned}\mu_{\text{TiO}_2}^{\text{slab}}(p_{\text{O}_2}, T) &\leq g_{\text{TiO}_2}^{\text{bulk}}(p_{\text{O}_2}, T) \\ \mu_{\text{SrO}}^{\text{slab}}(p_{\text{O}_2}, T) &\leq g_{\text{SrO}}^{\text{bulk}}(p_{\text{O}_2}, T).\end{aligned}\quad (3.12)$$

Combining equations (3.10), (3.11) and inequalities (3.12) results that the surface can be in equilibrium with its surroundings *only* if $\mu_{\text{TiO}_2}^{\text{slab}}$ is within both upper and lower limits:

$$g_{\text{TiO}_2}^{\text{bulk}}(p_{\text{O}_2}, T) + \Delta G_{\text{f SrTiO}_3}(p_{\text{O}_2}, T) \leq \mu_{\text{TiO}_2}^{\text{slab}}(p_{\text{O}_2}, T) \leq g_{\text{TiO}_2}^{\text{bulk}}(p_{\text{O}_2}, T). \quad (3.13)$$

Therefore when

$$\mu_{\text{TiO}_2}^{\text{slab}}(p_{\text{O}_2}, T) = g_{\text{TiO}_2}^{\text{bulk}}(p_{\text{O}_2}, T) \quad (3.14)$$

the system is in equilibrium with TiO_2 , and when

$$\mu_{\text{TiO}_2}^{\text{slab}}(p_{\text{O}_2}, T) = g_{\text{TiO}_2}^{\text{bulk}}(p_{\text{O}_2}, T) + \Delta G_{\text{f SrTiO}_3}(p_{\text{O}_2}, T) \quad (3.15)$$

the system is in equilibrium with SrO .

Equation (3.13) gives theoretically well-defined limits for $\mu_{\text{TiO}_2}^{\text{slab}}$.

When the system is at equilibrium with SrO $\Delta G_{\text{f SrTiO}_3}(p_{\text{O}_2}, T)$ enters the formulae for $\mu_{\text{TiO}_2}^{\text{slab}}(p_{\text{O}_2}, T)$ in Equation (3.15). $\Delta G_{\text{f SrTiO}_3}(p_{\text{O}_2}, T)$ is computed from equation (3.10) at 0 K and $p_{\text{O}_2} = 0$ using *ab initio* values. Our calculations render $\Delta G_{\text{f SrTiO}_3}(0, 0)$ equal to -1.54 eV per formula unit, which compares very well with the previous theoretical results from Demkov: -1.52 eV per formula unit [35], and Johnston: -1.49 eV per formula unit [26]. We use $\Delta G_{\text{f SrTiO}_3}(0, 0)$ as the range between our two equilibrium situations. This represents an estimate of the truly accessible range of the TiO_2 chemical potentials and allows equation (3.13) to be written as

$$\Delta G_{\text{f SrTiO}_3}(0, 0) \leq \mu_{\text{TiO}_2}^{\text{slab}}(p_{\text{O}_2}, T) - \mu_{\text{TiO}_2}^{\text{bulk}}(p_{\text{O}_2}, T) \leq 0. \quad (3.16)$$

Summing all the considerations already made in Equations (3.6) and (3.8), and assuming we are *in equilibrium with TiO_2* , we can recast equation (3.5) as⁴

$$\begin{aligned}
\sigma(\mu_{TiO_2}, p_{O_2}, T) &= \\
&= \frac{1}{2A_s} \underbrace{\left(E_{0K}^{slab} - N_{SrO} E_{SrTiO_3, 0K}^{bulk} \right) - \Gamma_{TiO_2} E_{TiO_2, 0K}^{bulk}}_{\text{surface energy at 0K}} + \\
&\frac{1}{2A_s} \underbrace{\left(F_{Vib}^{slab}(T) - N_{SrO} F_{SrTiO_3, Vib}(T) \right) - \Gamma_{TiO_2} F_{TiO_2, Vib}(T)}_{\text{surface vibrational free energy}} + \\
&\frac{1}{2A_s} \left(p(V^{slab} - N_{SrO} V_{SrTiO_3}^{bulk}) - \Gamma_{TiO_2} V_{TiO_2}^{bulk} - \right. \\
&\left. \Gamma_O \mu_O(p_{O_2}, T) \right).
\end{aligned} \tag{3.17}$$

The pressure p will never be greater than 1 atm (in fact, experiments are usually made in UHV conditions) and since $(V^{slab} - N_{SrO} V_{SrTiO_3}^{bulk} - \Gamma_{TiO_2} V_{TiO_2}^{bulk})$, for the slabs simulated in this thesis, it has a value of at most $6 \times 10^{-27} m^3$, the $p(V^{slab} - N_{SrO} V_{SrTiO_3}^{bulk} - \Gamma_{TiO_2} V_{TiO_2}^{bulk})$ term could contribute only a maximum of $5 \times 10^{-23} \frac{J}{m^2}$ to σ , which we can ignore. As regards S_{Config}^{slab} , $S_{Config}^{SrTiO_3}$ and $S_{Config}^{TiO_2}$, they are set equal to zero, provided the atomic configuration is known.

A key point to notice in the first two terms of equation (3.17) is that the absolute Gibbs free energies do not enter into the computation of $\sigma(\mu_{TiO_2}, p_{O_2}, T)$, but the *difference* of the Gibbs free energies of bulk and surface do. This often implies some cancellation of those parts of the energy that scales with the size of the slab, like the surface energy at 0 K and the surface vibrational free energy. In physical terms, we might say that the relevant vibrational contributions are those due to changes of vibrational modes at the surface as compared to the bulk. In table (3.1) we can see examples of these contributions in several oxides taken from the literature.

The contributions depicted in Table (3.1) are small, but not small on the scale of the differences in σ we have found between some of the different surface structures and terminations, to be described in Chapter (5). As the $SrTiO_3$ is a ceramic we might think that its vibrational contributions to the surface free energy are small as well. However, to obtain a rough estimate of this contribution, we have used an Einstein model⁵ and

⁴In equilibrium with SrO we would have to add the extra term $\frac{1}{2A_s} (\Gamma_{TiO_2} \Delta G_f^{SrTiO_3}(0, 0))$ to Equation (3.5). But the rest is the same.

⁵A detailed explanation of this model is presented in the Appendix. The expression for the surface

Compound	Vib. Contribution [J/m ²]
PdO [40]	-0.3
RuO ₂ (001) [39]	-0.16
α Al ₂ O ₃ [43]	-0.18
NiO(100) [44]	-0.2

Table 3.1: Maximum vibrational contributions to the surface free energy for different surfaces. In the case of PdO, this maximum corresponds to more than one surface termination, namely: PdO(001), PdO(100) PdO(101), PdO(110) and PdO(111).

approximated the phonon density of states by just one characteristic frequency for each atom type. If we further consider that the vibrational modes of the atoms in the topmost layer might be significantly changed at the surface, we have $\omega_O^{Bulk SrTiO_3} = 4.5 \times 10^{12} \frac{1}{s}$, $\omega_{Sr}^{Bulk SrTiO_3} = 3.75 \times 10^{12} \frac{1}{s}$ and $\omega_{Ti}^{Bulk SrTiO_3} = 5.0 \times 10^{12} \frac{1}{s}$ as characteristic frequencies of O, Sr and Ti in SrTiO₃ bulk [45]. The values of ω at the surface are a variation of 50% of these values at SrTiO₃ bulk. Equation (3.17) includes $F_{TiO_2 Vib}^{bulk}(T)$ and, to be consistent with our model, we have approximated its density of states by characteristic frequencies for each atom type: $\omega_O^{Bulk TiO_2} = 15 \times 10^{12} \frac{1}{s}$ and $\omega_{Ti}^{Bulk TiO_2} = 12.5 \times 10^{12} \frac{1}{s}$ are these frequencies in TiO₂ bulk [46].

Using the aforementioned model, we have computed the vibrational contributions to the surface free energy of all the surface reconstructions studied in this thesis. In Figure (3.1) we present the vibrational contributions to the surface free energy of seven different reconstructions, in the temperature range of interest in the present study, which represent the trend within all the reconstructions. Furthermore, all the vibrational contributions of the reconstructions not included in Figure (3.1) stay within 0.2 J/m². In conclusion, we take the values on Figure (3.1) to be indicative the vibrational influence on the surface free energy. Such a 0.2 J/m² is not a completely negligible factor, yet as it will become apparent in the discussion of the results, this uncertainty does not affect the physical conclusions drawn in the present application⁶. Hence, we neglect the complete vibrational contribution to the surface free energy, leaving only the term labelled as *surface energy at 0K* as a good approximation to the entire solid-phase contribution to the surface free energy. However, we stress that it is not a general result and needs to be checked for every specific system.

vibrational free energy becomes considerably complex.

⁶There is only one exception: the $c(4 \times 2)$ TiO₂-DL(B) surface reconstruction. This particular case will be discussed in detail in Section (5.2)

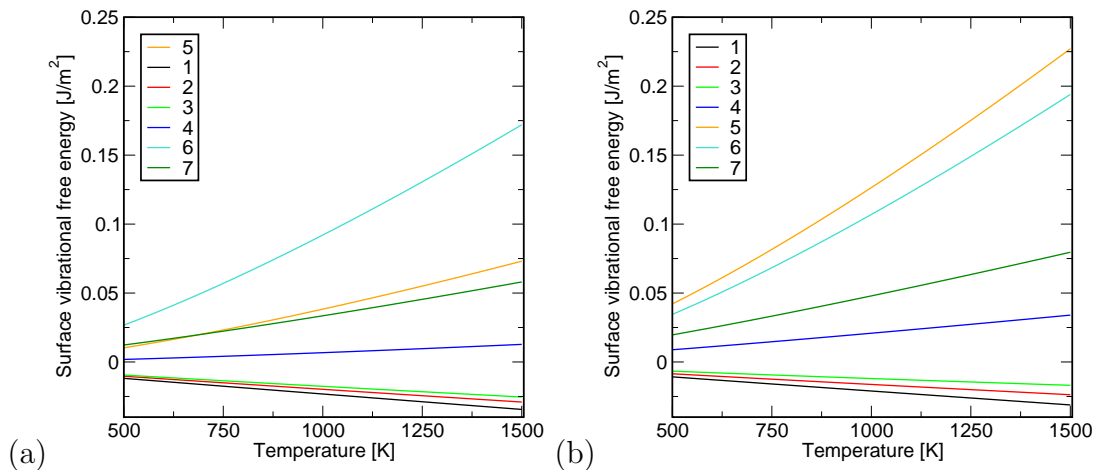


Figure 3.1: In (a) the vibrational modes at the surface differ by +50% from the bulk values, while in (b) the difference is -50%. The depicted reconstructions are as follows: **(1)** $(\sqrt{13} \times \sqrt{13})$, **(2)** $c(4 \times 4)$, **(3)** $(\sqrt{5} \times \sqrt{5})$ and **(4)** (2×1) from the Sr adatom model (See Section (5.1)). **(5)** $c(4 \times 2)$ TiO₂-DL(B) and **(6)** (2×1) TiO₂-DL from the Double layer model (See Section (5.2)). Finally, we have **(7)** (2×1) TiO₂-SL which is our proposed model for the (2×1) surface reconstruction (See Section (5.2)).

The fourth term in equation (3.17) is the gas phase's contribution to the surface free energy calculated using the oxygen chemical potential $\mu_O(p_{O_2}, T)$. Here the effect of pressure and temperature upon the chemical potential cannot be ignored. Moreover, the large variations in $\mu_O(p_{O_2}, T)$ can be used to control the state of condensed phases in equilibrium with the gas. In general, the function $\mu_O(p_{O_2}, T)$ is complicated but can in principle be determined for any gas either experimentally or theoretically. This will be presented in detail in the next section.

3.1.2 Gas phase: the oxygen chemical potential $\mu_{O_2}(p_{O_2}, T)$

An expression for $\mu_O(p_{O_2}, T)$ is what we need to express equation (3.17) in terms of p_{O_2} . Since we are dealing with temperatures well above 298 K and pressures below 1 atm, we may assume that O₂ behaves as an ideal gas. We can, therefore, use standard thermodynamics techniques to obtain an expression for $\mu_{O_2}(p_{O_2}, T)$ and then use this value to obtain $\mu_O(p_{O_2}, T)$, since $\mu_O(p_{O_2}, T) = \frac{\mu_{O_2}(p_{O_2}, T)}{2}$. We take as a reference point the chemical potential of oxygen at standard pressure and temperature $\mu_{O_2}(p_{O_2}^0, T^0) \equiv \mu_{O_2}^0$, and then

integrate along the pressure and temperature axes in turn until we reach the desired p_{O_2} and T [36]. We cannot obtain $\mu_{O_2}^0$ directly from experimental data, because this $\mu_{O_2}^0$ will be used in equation (3.17) to calculate the surface free energy and all the terms in this equation must be referred to the same zero of energy, that is: the one established by the method of total energy calculation. The general approach to calculating $\mu_{O_2}^0$ makes use of the Gibbs formation energies of oxides [36, 47]. Information on these energies is usually available from tabulated experimental data. In the following, we will briefly describe the methodology used to obtain an analytical expression for $\mu_{O_2}(p_{O_2}, T)$ that was proposed by Johnston and coworkers [36].

We start looking for an analytical expression for the oxygen chemical potential first by writing $\mu_{O_2}(p_{O_2}, T)$ using the standard thermodynamic relation for perfect gases [36]

$$\left(\frac{\partial \mu_{O_2}}{\partial p}\right)_T = \frac{kT}{p}. \quad (3.18)$$

Equation (3.18) is integrated from the reference pressure $p_{O_2}^0=1$ atm up to the desired pressure p_{O_2} , at some constant temperature T . We obtain the expression

$$\mu_{O_2}(p_{O_2}, T) = \mu_{O_2}(p_{O_2}^0, T) + kT \ln \left(\frac{p_{O_2}}{p_{O_2}^0}\right). \quad (3.19)$$

Now it is possible to use tabulated experimental data for $\mu_{O_2}(p_{O_2}, T) - \mu_{O_2}(p_{O_2}, T^0)$. Before doing so, it is useful to explore the ideal gas model a little more [36]. Temperature dependence is derived using the Gibbs-Helmholtz relation

$$\frac{\partial}{\partial T} \left(\frac{\mu_{O_2}}{T}\right)_p = -\frac{H}{T^2} \quad (3.20)$$

where H is the enthalpy per oxygen molecule. As we are dealing with an ideal gas composed of rigid balls, H can be expressed as $H = E_0 + C_p T$, where E_0 is the energy per molecule at 0 K and $C_p = \frac{5k}{2}$. Therefore, integrating (3.20) from the reference temperature T^0 up to T at constant pressure leaves us with

$$\mu_{O_2}(p_{O_2}, T) = E_0 + (\mu_{O_2}^0 - E_0) \left(\frac{T}{T^0}\right) - C_p T \ln \left(\frac{T}{T^0}\right) + kT \ln \left(\frac{p_{O_2}}{p_{O_2}^0}\right) \quad (3.21)$$

Equation (3.21) still contains two unknown quantities: E_0 and $\mu_{O_2}^0$. Lets first focus on the

second one.

We know that the standard Gibbs formation energy of a generic oxide M_xO_y is given by

$$\Delta G_{f M_xO_y}(p_{O_2}^0, T^0) = \mu_{M_xO_y}(p_{O_2}^0, T^0) - x \mu_M(p_{O_2}^0, T^0) - \frac{y}{2} \mu_{O_2}^0 \quad (3.22)$$

from where we can express $\mu_{O_2}^0$ as

$$\mu_{O_2}^0 = \frac{2}{y} \left[-\Delta G_{f M_xO_y}(p_{O_2}^0, T^0) + \mu_{M_xO_y}(p_{O_2}^0, T^0) - x \mu_M(p_{O_2}^0, T^0) \right]. \quad (3.23)$$

A nice property of equation (3.23) is that it does not require the calculation of any absolute oxygen molecule property; in particular, its internal energy at $0 K$, which is subject to greater uncertainty than the energy of simple metals and their oxides[48]⁷. As $\mu_{O_2}^0$ has to be referred to the zero of energy established by the total energy calculations, we must calculate $\mu_{M_xO_y}(p_{O_2}^0, T^0)$ and $\mu_M(p_{O_2}^0, T^0)$ from first principles. The full temperature dependence of these bulk chemical potentials is very expensive to compute from first principles but, for condensed phases like bulk metals or metallic oxides it is known to be very small, as we will see in the following.

We can then recast equation (3.23) as

$$\begin{aligned} \mu_{O_2}^0 = & \frac{2}{y} \left[-\Delta G_{f M_xO_y}(p_{O_2}^0, T^0) + E_{M_xO_y}^0(0K) - x E_M^0(0K) \right] + \\ & \frac{2}{y} \underbrace{\left[\Delta h_{M_xO_y}(T^0) - x \Delta h_M(T^0) + T^0 (S_{M_xO_y}(T^0) - x S_M(T^0)) \right]}_{E_G(T^0)} \end{aligned} \quad (3.24)$$

⁷Li *et al* [48] calculated the binding energy, bond length and frequency of molecular oxygen. Their DFT total energy calculations were performed using a pseudopotential plane wave method within the generalised gradient approximation (GGA) for the exchange correlation functional. Their converged results are: 3.6 eV/atom for the binding energy, 2.3 bohr for the bond length and 189 meV for the frequency. The respective experimental results are 2.56 eV, 2.28 bohr and 197 meV, while the binding energy calculated by Perdew *et al* with the same GGA-PBE is 3.12 eV[49]. The calculated bond length and frequency agreed very well with the experimental results. Despite the over binding of the calculated binding energy, the different theoretical methods give comparable results. These results clearly indicate that the over binding is from the exchange and correlation approximation in DFT. The error is a systematic one.

or, alternatively as

$$\mu_{O_2}^0 = \frac{2}{y} \left[-\Delta H_{f_{M_xO_y}}(p_{O_2}^0, T^0) + E_{M_xO_y}^0(0K) - x E_M^0(0K) \right] + \underbrace{\frac{2}{y} [\Delta h_{M_xO_y}(T^0) - x \Delta h_M(T^0)]}_{E_H(T^0)}. \quad (3.25)$$

In Equation (3.24), we have assumed that $0K$ total energies are estimates of the Gibbs energies of solid phases, while in Equation (3.25) the assumption was that the $0K$ total energies are estimates of the enthalpies of solid phases. The enthalpy change between $0K$ and T^0 is given by $\Delta h(T^0)$, while the Gibbs energy change in the same temperature range is given by $\Delta h(T^0) + T^0 S(T^0)$. $\Delta G_{f_{M_xO_y}}(p_{O_2}^0, T^0)$ and $\Delta H_{f_{M_xO_y}}(p_{O_2}^0, T^0)$ can be obtained from tables of experimental data. $E_G(T^0)$ and $E_H(T^0)$ are the errors implied by either approach. Using available experimental data, Lozovoi and coworkers [47] have tabulated these errors for all but three of the oxides used in this work⁸. They concluded that, although all these errors are very small, using the $0K$ ab initio total energies as estimates of the Gibbs free energies is better than using them as estimates of the enthalpies.

We applied equation (3.24) to twelve oxides, considering the values of $E_G(T^0)$ obtained by Lozovoi and coworkers [47] as negligible⁹. In table (3.2) we present the structural parameters of all the oxides involved in the calculation of $\mu_{O_2}^0$. The calculated values for $\mu_{O_2}^0$ are presented in figure (3.2).

In theory, the results should be independent of the oxide used. However, as it can be seen in figure (3.2), there is some dispersion in the values of $\mu_{O_2}^0$ depending on the oxide. Leaving aside the experimental errors, one of the reasons for $\mu_{O_2}^0$ to differ from one oxide to another, is the neglect of thermal contributions to the Gibbs energies of the solids which are present in the experimental $\Delta G_{f_{M_xO_y}}(p_{O_2}^0, T^0)$. Moreover, the values of $\mu_{O_2}^0$ are dependent on the implicit reference states of the components in the first principles calculation. The aforementioned considerations, together with the fact that DFT has intrinsic errors related with the treatment of exchange and correlation, make it difficult to eliminate the dispersion on the $\mu_{O_2}^0$'s values. We adopted $\bar{\mu}$ (the mean value) and its corresponding standard deviation as a representative value: $\mu_{O_2}^0 = -433.23 \text{ eV}^{10}$. In Figure

⁸They did not calculate $E_G(T^0)$ and $E_H(T^0)$ for Cu_2O , Ag_2O and PbO_2 .

⁹The largest correction is for SrO and is equal to 0.025 eV .

¹⁰This value is in the SIESTA reference.

M_xO_y/M	Structure	$a_{exp}[\text{\AA}]$	$a_{cal}[\text{\AA}]$	$c_{exp}[\text{\AA}]$	$c_{cal}[\text{\AA}]$	$(c/a)_{exp}$	$(c/a)_{cal}$
Sr	FCC	6.08	5.76	-	-	-	-
SrO	Rock salt	5.16	5.075	-	-	-	-
Ti	HCP	2.95	2.808	4.69	4.47	1.59	1.59
TiO ₂ [50]	Rutile	4.593	4.58	2.96	2.94	0.644	0.642
Mg	HCP	3.21	3.19	5.21	5.17	1.62	1.62
MgO	Rocksalt	4.21	4.16	-	-	-	-
Si	Diamond	5.43	5.42	-	-	-	-
SiO ₂ [51]	α -quartz	4.916	4.127	5.405	5.299	1.1	1.284
Al	FCC	4.05	4.001	-	-	-	-
Al ₂ O ₃ [52]	Corundum	4.761	4.758	12.991	12.935	2.729	2.718
Ca	FCC	5.58	5.757	-	-	-	-
CaO	Rocksalt	4.81	4.936	-	-	-	-
Pb	FCC	4.95	5.01	-	-	-	-
PbO ₂ [53]	Rutile	4.955	5.058	3.383	3.53	0.683	0.697
Cd	HCP	2.98	3.07	5.62	4.90	1.89	1.59
CdO[52]	Rocksalt	4.6953	4.7122	-	-	-	-
α -Sn	Diamond	6.49	6.43	-	-	-	-
SnO ₂ [53]	Rutile	4.738	4.701	3.188	3.193	0.673	0.679
Cu	FCC	3.615	3.544	-	-	-	-
Cu ₂ O	Cuprite	4.2696	4.1456	-	-	-	-
Ag	FCC	4.0862	4.009	-	-	-	-
Ag ₂ O	Cuprite	4.72	4.591	-	-	-	-
Zn	HCP	2.66	2.61	4.95	4.90	1.86	1.88
ZnO	Zincite	3.2493	3.3070	5.2054	5.2967	1.602	1.602

Table 3.2: Structural parameters for several oxides. *exp* stands for experimental and *cal* for calculated. Except where specified, all the experimental results are from [54].

(3.2), SrO is well outside the region limited by the standard deviation. From Table (3.2), we notice that the largest error in the calculated lattice constant is in the case of Sr. We attributed this error to the Sr's pseudopotential. This pseudopotential works very well in SrO, but the calculation of $\mu_{O_2}^0$ needs the total energies of both, Sr and SrO. In the subsequent sections, it will become clear that the achieved accuracy is enough for making our theoretical calculations meaningful in the context of the problem we intend to approach.

Now that $\mu_{O_2}^0$ has been estimated, we are still left with the problem of calculating E_0 in equation (3.21). Attempting an accurate total energy calculation for the oxygen molecule would have been unnecessarily complicated. Instead, we made use again of experimental data. For oxygen, the temperature dependence of the Gibbs free energies per mole at

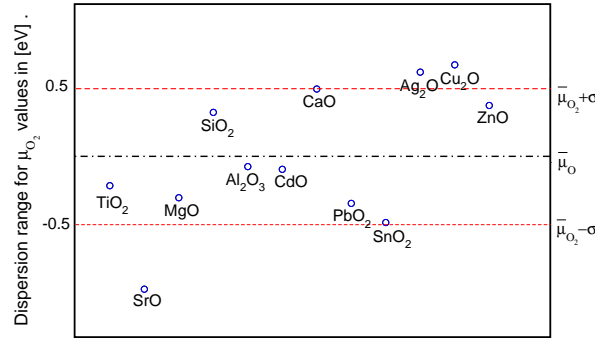


Figure 3.2: Distribution of μ_{O_2} around $\bar{\mu}_{O_2}$. The red dotted lines represents the standard deviation for $\bar{\mu}$.

standard pressure has been fitted to polynomials [55], namely

$$G(p_{O_2}^0, T) = A(T - T \ln(T)) - \frac{1}{2}BT^2 - \frac{1}{2}CT^3 - \frac{1}{2}DT^4 - \frac{E}{2T} + F - GT. \quad (3.26)$$

And the coefficients in equation (3.26) are listed in Table (3.3)

Parameter	Value	Units
A	29.659×10^{-3}	$\frac{\text{KJ}}{\text{mol K}}$
B	6.137261×10^{-6}	$\frac{\text{KJ}}{\text{mol K}^2}$
C	-1.186521×10^{-9}	$\frac{\text{KJ}}{\text{mol K}^3}$
D	0.095780×10^{-12}	$\frac{\text{KJ}}{\text{mol K}^4}$
E	0.219663×10^3	$\frac{\text{KJK}}{\text{mol}}$
F	-9.861391	$\frac{\text{KJ}}{\text{mol}}$
G	237.948×10^{-3}	$\frac{\text{KJ}}{\text{mol K}}$

Table 3.3: Coefficients in expression (3.26) [36]

We rewrite Equation (3.26) as

$$\mu_{O_2}(p_{O_2}, T) = \mu_{O_2}^0 + G(p_{O_2}^0, T) - G(p_{O_2}^0, T^0) + kT \ln\left(\frac{p_{O_2}}{p_{O_2}^0}\right) \quad (3.27)$$

and we can now fix the value of E_0 by equating the temperature derivative of equations

(3.21) and (3.27), using (3.26) to evaluate $\frac{\partial G(p_{O_2}^0, T)}{\partial T}$ [36].

Finally, once we have a value for E_0 , we use equation (3.21) to evaluate $\mu_{O_2}(p_{O_2}, T)$, which we can in turn be used to evaluate $\mu_O(p_{O_2}, T)$, since $\mu_{O_2}(p_{O_2}, T) = 2\mu_O(p_{O_2}, T)$. Expression (3.21) may be recast according to [47]

$$\begin{aligned} \mu_O(p_{O_2}, T) = & \frac{1}{y} [\Delta G_{f_{M_x O_y}}(p_{O_2}^0, T^0) - \mu_{M_x O_y}(p_{O_2}^0, T^0) + \\ & x \mu_M(p_{O_2}^0, T^0)] + \Delta \mu_O(p_{O_2}, (T - T^0)) + \frac{1}{2} kT \ln \left(\frac{p_{O_2}}{p_{O_2}^0} \right). \end{aligned} \quad (3.28)$$

This expression allows us to estimate the accuracy of the ideal gas approximation as we increase the temperature. The best values for $\Delta \mu_O(p_{O_2}, T)$ are obtained interpreting experimental data with statistical mechanics for ideal gases [55]. If we compare these values with the ones obtained through formula (3.21), we find that equation (3.21) accurately predicts the temperature dependence [47].

Stability limits for $\mu_O(p_{O_2}, T)$

In principle, the gas expressions alone permit any values of the $\mu_{O_2}(p_{O_2}, T)$. This may lead us to an unphysical situation because there are limits on the allowable range in equilibrium with all possible phases. If $\mu_{O_2}(p_{O_2}, T)$ becomes too low, all oxygen would leave the sample, i.e. the SrO and TiO₂ oxides would decompose into solid Sr and Ti and oxygen gas. This implies that, due to thermodynamical reasons, a whole region on the (p_{O_2}, T) plane will be excluded when plotting surface energy plots. The analytical formulation of the previous statements will allow us to find mathematically well defined expressions for the limits on $\mu_O(p_{O_2}, T)$ for which the slab is stable.

As the TiO₂ is at equilibrium in the slab

$$\mu_{TiO_2}^{slab} = \mu_{Ti}^{slab} + 2\mu_O(p_{O_2}, T) \quad (3.29)$$

and the titanium chemical potential in the slab must be less or equal to the one in the bulk phase

$$\mu_{Ti}^{slab} \leq \mu_{Ti}^{bulk} \quad (3.30)$$

by combining equations (3.29) and (3.30) we get

$$\mu_{\text{O}}(p_{\text{O}_2}, T) \geq \frac{\mu_{\text{TiO}_2}^{\text{slab}} - \mu_{\text{Ti}}^{\text{bulk}}}{2}. \quad (3.31)$$

The same can be postulated for the SrO in the slab

$$\mu_{\text{SrO}}^{\text{slab}} = \mu_{\text{Sr}}^{\text{slab}} + \mu_{\text{O}}(p_{\text{O}_2}, T) \quad (3.32)$$

with

$$\mu_{\text{Sr}}^{\text{slab}} \leq \mu_{\text{Sr}}^{\text{bulk}} \quad (3.33)$$

and the combination of equations (3.32) and (3.33) gives

$$\mu_{\text{O}}(p_{\text{O}_2}, T) \geq \mu_{\text{SrO}}^{\text{slab}} - \mu_{\text{Sr}}^{\text{bulk}}. \quad (3.34)$$

Recalling equation (3.11), the equilibrium equation for the slab, we can re-write (3.34) as

$$\mu_{\text{O}}(p_{\text{O}_2}, T) \geq g_{\text{SrTiO}_3}^{\text{bulk}} - \mu_{\text{TiO}_2}^{\text{slab}} - \mu_{\text{Sr}}^{\text{bulk}}. \quad (3.35)$$

Since $\mu_{\text{TiO}_2}^{\text{slab}}$ varies within a range stated by equation (3.10) (the SrTiO₃ formation energy) we might think of expressions (3.35) and (3.31) as two straight line equations with $\mu_{\text{TiO}_2}^{\text{slab}}$ as the independent variable. Both straight lines are setting limits for $\mu_{\text{O}}(p_{\text{O}_2}, T)$. These limits are shown in Figure (3.3)

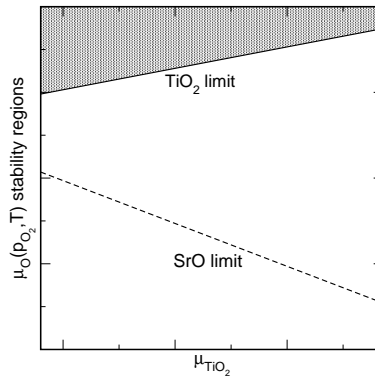


Figure 3.3: Schematic representation of the limits on $\mu_{\text{O}}(p_{\text{O}_2}, T)$. The dashed line represents expression (3.35), while the solid one accounts for equation (3.31). The shaded region shows the beginning of the allowed region of $\mu_{\text{O}}(p_{\text{O}_2}, T)$ values. The values of μ_{TiO_2} on the x axis go from equilibrium with TiO₂ (left limit) to equilibrium with SrO (right limit).

Figure (3.3) is only qualitative. Its purpose is to show that the limit imposed by equation (3.31) on $\mu_O(p_{O_2}, T)$ is the only one needed to define the stability region.

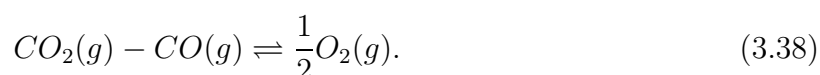
For every value of $\mu_{TiO_2}^{slab}$ we would have a corresponding $\mu_O(p_{O_2}, T)$ value. Equation (3.21) allows us to translate these $\mu_O(p_{O_2}, T)$ limits to the (p_{O_2}, T) plane.

3.1.3 Discussion: the UHV pressure.

So far, we have equated the UHV pressure with the oxygen pressure, assuming oxygen is all we have in the gaseous phase. This may not be necessarily true: the chemical procedure used to treat the $SrTiO_3$ surface is known to leave carbon-containing impurities [36, 7] if appropriate surface-cleaning procedures are not carried out properly. Therefore, we may very well have the presence of a reducing agent like carbon at the surface. This carbon presence makes it possible to obtain very low effective partial pressures of p_{O_2} , because the gaseous phase would now be a mixture of gases, namely CO_2 , CO and O_2 . This idea was first proposed by Johnston and coworkers [36]. However, they only calculated the oxygen partial pressure p_{O_2} at $T = 1000 K$, assuming that only CO_2 can be obtained from the chemical reaction between $C(s)$ and $O_2(g)$. In the following we present an extension of Johnston's idea to a *multi-variant reacting system* with the two independent reactions



and a third reaction which we get from subtracting equation (3.36) from (3.37)



For this system, the temperature dependence of the oxygen partial pressure for $T = 1000 K$ up to $T = 1500 K$ was calculated.

As we did with the oxygen, we can consider CO_2 and CO as ideal gases. The chemical potential of component k in an ideal gas mixture at temperature and pressure (T, P) is given by

$$\mu_k(T, P) = \mu_k^0(T, P) + RT \ln \left(\frac{p_k}{P} \right) \quad (3.39)$$

$\mu_k^0(T, P)$ is its chemical potential in a pure reference state and P_k is its partial pressure in the mixture. As we assume our gaseous system is in equilibrium, for a generic chemical

reaction at (T, P)

$$xX + yY = zZ. \quad (3.40)$$

The change in Gibbs free energy vanishes

$$\Delta G(T, P) = z\mu_Z(T, P) - x\mu_X(T, P) - y\mu_Y(T, P) = 0. \quad (3.41)$$

If we now combine equations (3.39) and (3.41) with (3.36) we have

$$\begin{aligned} \Delta G(P, T) = & \mu_{CO(g)}^0(P, T) + RT \ln \left(\frac{p_{CO}}{P} \right) - \mu_{C(s)}^0(P, T) - \\ & \frac{1}{2} \mu_{O_2}^0(P, T) - RT \ln \left(\frac{p_{O_2}}{P} \right)^{1/2} \end{aligned} \quad (3.42)$$

where $\mu_{CO(g)}^0(P, T)$, $\mu_{C(s)}^0(P, T)$ and $\mu_{O_2}^0(P, T)$ are chemical potentials of pure reference states. Since we assume CO and O₂ to be ideal gases, using the relation

$$\left(\frac{\partial G}{\partial P} \right)_T = V \quad (3.43)$$

we can reach by integration any pressure P starting from a reference pressure P^0 , which we take as 1 atm. Regarding $\mu_{C(s)}^0(P, T)$, since it is a solid, we can consider its variation with pressure as negligible. Using the relation in (3.43), we can recast equation (3.42) as

$$\begin{aligned} \Delta G(P, T) = & \underbrace{\mu_{CO(g)}^0(P^0, T) - \mu_{C(s)}^0(P^0, T) - \frac{1}{2} \mu_{O_2}^0(P^0, T)}_{\Delta G_1^0(T)} - \\ & RT \ln \left(\frac{p_{CO}}{\sqrt{p_{O_2}}} \right) \end{aligned} \quad (3.44)$$

Since we are in equilibrium $\Delta G(P, T)=0$

$$\exp \left(\frac{-\Delta G_1^0(T)}{RT} \right) = \frac{p_{CO}}{\sqrt{p_{O_2}}}. \quad (3.45)$$

Applying the same considerations to equations (3.37) and (3.38) gives

$$\exp \left(\frac{-\Delta G_2^0(T)}{RT} \right) = \frac{p_{CO_2}}{p_{O_2}} \quad (3.46)$$

and

$$\exp\left(\frac{-\Delta G_3^0(T)}{RT}\right) = \frac{\sqrt{p_{O_2}}p_{CO}}{p_{CO_2}}. \quad (3.47)$$

Finally, the UHV pressure is the sum of the partial pressures

$$P = p_{CO_2} + p_{O_2} + p_{CO}. \quad (3.48)$$

The $\Delta G_i^0(T)$ are functions only of temperature, and analytical expressions for them are obtained from the literature [56], namely:

$$\Delta G_1^0(T) = -26700 - 20.95T \quad (3.49)$$

$$\Delta G_2^0(T) = -94200 - 0.2T \quad (3.50)$$

$$\Delta G_3^0(T) = -67500 + 20.75T \quad (3.51)$$

where the units are $\frac{\text{cal}}{\text{mol K}}$. The combination of equations (3.45), (3.47) and (3.48) gives

$$P = p_{O_2} + \sqrt{p_{O_2}} \exp\left(\frac{-\Delta G_1^0(T)}{RT}\right) + p_{O_2} \exp\left(\frac{\Delta G_3^0(T) - \Delta G_1^0(T)}{RT}\right) \quad (3.52)$$

Equation (3.52) relates p_{O_2} and T and, given a value of T , has to be solved numerically for p_{O_2} . We solved this equation for five hundred T values in the 1000-1500 K range, with a UHV pressure of $P = 1 \times 10^{-12}$ atm. The values for $\log(p_{O_2})$ are plotted in Figure (3.4), which are the pressures of O_2 to be found in a sample where there is solid carbon present.

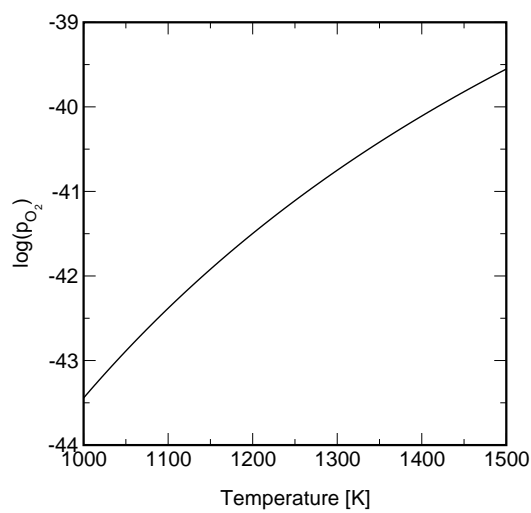


Figure 3.4: Temperature dependence of $\log(p_{O_2})$ within the stated temperature range at $P = 1 \times 10^{-12}$ atm.

Chapter 4

Total energy calculations with SIESTA

Our calculations were performed within the the local density approximation [57, 58] to density functional theory [59, 60] as implemented in the SIESTA program [61, 62]. The main reason why we chose SIESTA was because of the size of the systems we wanted to simulate.

A crucial step in computational science is the creation of a relevant geometric model. These models have to be small enough to be tractable by today's electronic structure methods yet still large enough to be physically meaningful. The geometry we adopted here is the repeated slab geometry. Thin films consisting of 7 layers, with a 3 layers spacing between them, are repeated in the direction perpendicular to the surface. The width is taken in order to have bulk-like behaviour near the centre of each layer and the spacing is taken large enough so that any artificial interactions across the vacuum region between the slabs are minimised.

Since the systems we are dealing with are slabs terminated in a free surface, the Hamiltonian is a square matrix of rank N_{orb} , where N_{orb} is the number of basis orbitals in the system. If we increase the size of the system, N_{orb} increases as well in proportion to the number of atoms or electrons (N). The computation time required scales with the cube of N . Most of the slabs simulated in this thesis have more than one hundred atoms and, although this is small enough to be treated in a first principles level with many of today's programs, SIESTA's localised orbital approach has some advantages. SIESTA implements a fully selfconsistent DFT based on a flexible linear combination of atomic orbitals. There

are no constraints either on the radial shape of these orbitals nor on the size of the basis. Due to the sparsity of the obtained Hamiltonian matrix, this methodology allows extremely fast simulations using a small number of basis functions. In our calculations, a basis of numerical atomic orbitals generated using the methods described in reference [63] was used to expand the one-electron Kohn-Sham orbitals.

SIESTA allows for both, the Local Density Approximation (LDA) [57] and the Generalised Gradient Approximation (GGA) [49]. It uses standard norm-conserving pseudopotentials [64] in their fully nonlocal form [65, 66].

The matrix elements of the Hartree and exchange and correlation parts of the Hamiltonian are evaluated numerically on a uniform real space grid [61]. The smoothness of the integrand determines how fine a grid is needed. It is worth mentioning here that the use of pseudopotentials, which eliminates the rapidly varying core charge, is essential to provide functions smooth enough to make the grid integration feasible. The grid fineness is measured by the energy of the shortest wave-length plane-wave that can be described with the grid, as in plane-wave calculations.

4.1 SIESTA basics

4.1.1 Numerical atomic orbitals (NAO)

In principle, we could use atomic orbitals themselves to construct our localised basis set, but their long-range tails are not desirable if we aim for fast simulations. The overlapping of the aforementioned tails among atoms in a solid increase the accuracy of the calculations while decreasing their speed, because the Hamiltonian matrix is less sparse. Therefore, through varying the orbitals' localisation range, a tradeoff between accuracy and speed have to be found. Atomic orbitals with small localisation ranges are more desirable: they are better suited to the final application. Many different procedures have been proposed for generation of compressed, short-range orbitals [67, 68]. *SIESTA* uses numerical atomic orbitals (NAO), which are obtained by finding the eigenfunctions of the isolated pseudo-atoms confined within spherically symmetric potential wells of different radii [69]. These schemes give strictly localised orbitals, i.e. orbitals that are strictly zero beyond a given cutoff radius r_c . For these bases of strictly localised orbitals, the problem is finding a balanced

and systematic way of defining all the different cutoff radii, since both the accuracy and the computational efficiency in the calculations depend on them. The scheme implemented in SIESTA to deal with this issue [63] is one in which all radii are defined by one single parameter: the energy increase imposed on the orbital when confined. This procedure allows us to obtain a well-balanced basis. The confinement energy (*energy shift* in SIESTA) used in all the total energy calculations performed in this thesis was 0.1 eV. We chose this value after comparing our results for the surface energy of the (1×1) and (2×1) surface reconstructions with previous calculations [36]. A value of 0.2 eV is enough for the lattice constant, bulk modulus, elastic constants and antiferrodistortive distortion of SrTiO₃ to be in good agreement with plane wave [70] and FP-LMTO [36] calculations. However, at the surface a longer range in the basis orbitals is needed in order to represent the decaying tail of the electronic density into the vacuum. A smaller energy shift accounts for this surface effect, without losing accuracy in the bulk tests [71].

4.1.2 Multiple- ζ and polarisation orbitals

NAO's are products of spherical harmonics with numerical radial functions centred on atoms. They are very flexible, can be strictly localised and few of them are needed for accurate results. For atom I located at R_I ,

$$\phi_{Ilmn}(r) = \phi_{In}(r_I)Y_{lm}(r_I) \quad (4.1)$$

where $r_I = r - R_I$. Usually, the quantum chemical literature distinguishes between core, valence and polarisation basis orbitals. In our case, core states are eliminated by the use of norm-conserving pseudopotentials [66]. If several basis orbitals with the same centre and angular momentum are used to expand the valence states, we label them following standard quantum chemical notation, i.e. first- ζ orbital, second- ζ orbital, etc. Radial flexibility in the *NAO*'s is achieved by combining different ζ orbitals for the same angular momentum channel. This is conventionally called *multiple- ζ* .

In the case of a minimal single- ζ basis set, we have only one radial function per angular momentum channel, and only for those angular momenta with substantial electronic population in the valence of the free atom. We start by having radial flexibility when we add a second radial function per channel: a second- ζ orbital. This second- ζ function is obtained using an implementation in SIESTA of the standard “split-valence” method [72].

The second- ζ orbital is split from the first- ζ basis orbitals. This second radial function reproduces exactly the tail of the original orbital from a given matching radius R_{DZ} outwards. The inner part goes smoothly towards the origin as $r^l(a - br^2)$, where a and b are chosen to ensure continuity of the function and its derivative at R_{DZ} . The radius R_{DZ} is set by fixing the norm of the first- ζ orbital in $r > R_{DZ}$. The value of this norm is set using the *split norm* parameter in SIESTA. In figure (4.1) we can see an example of a double- ζ basis set. As regards the angular flexibility, it is obtained by adding shells of higher

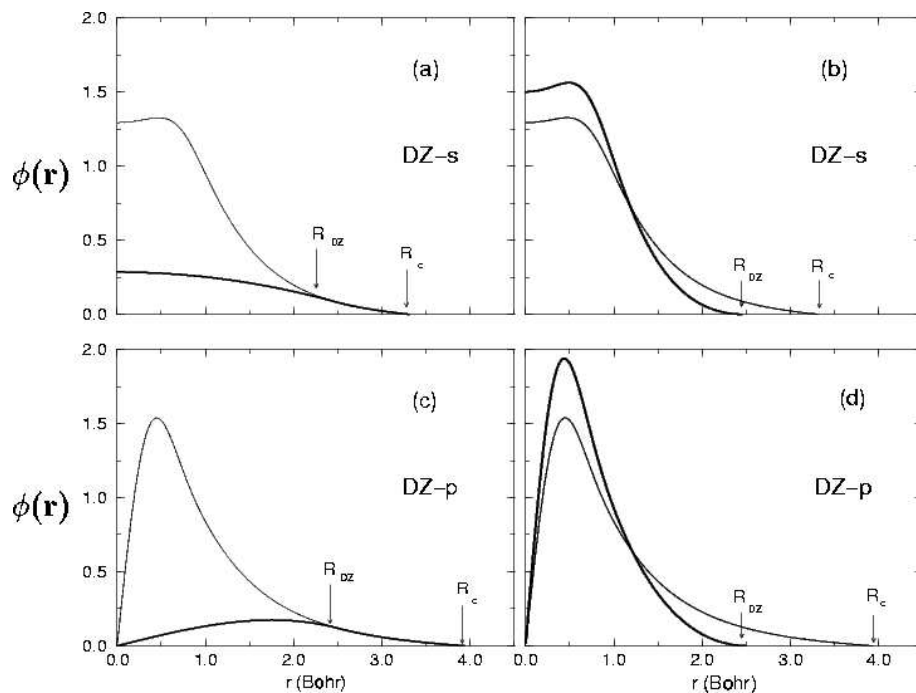


Figure 4.1: Figure produced by Sánchez[73]. It shows confined orbitals for the oxygen atom. s in (a) and (b), p in (c) and (d). In (a), R_c is the cutoff radii we obtain with a confinement energy of 0.1 eV. The thin line in (b) indicates a single- ζ basis. The second radial function is the solid line in (a). As we can see in (b), due to the action of the second radial function $r^l(a - br^2)$, the new double- ζ orbital, represented by a thick line, has a shorter tail than the single- ζ one, showed as a thin line. R_{DZ} indicates the new confinement radii for the double- ζ orbital. Figures (c) and (d) show the same for the p orbital.

angular momentum, the polarisation orbitals. Ways to generate this orbitals have been described in the literature [63]. The basic idea is to use a valence pseudoatomic orbital $\phi_{lm}(r) = \phi_l(r)Y_{lm}(r)$, such that there are no valence orbitals with angular momentum $l + 1$. This orbital is polarised with a small electric field. Using first-order perturbation theory we obtain a perturbed orbital with $l' = l + 1$. $\phi_{l+1,m}(r)$ is the polarisation orbital to be

added to the basis set.

4.1.3 SIESTA basis for the Strontium Titanate

The cutoff radii and reference configurations used to generate the pseudopotentials were taken from the work by Junquera and coworkers [74]. These configurations have been used successfully in the simulations of SrO/SrTiO₃ interfaces [74]. Core electrons were replaced by *ab initio* norm-conserving fully separable [65] Troullier-Martin [66] pseudopotentials. Due to the large overlap between semicore and valence states, the 3*s* and 3*p* electrons of Ti, 4*s* and 4*p* electrons of Sr were explicitly included in the calculation. The reference configuration and radii used to generate the pseudopotentials are shown in Table (4.1)

		Sr	Ti	O
Reference		$4s^2, 4p^6, 4d^0, 4f^0$	$3s^2, 3p^6, 3d^2, 4f^0$	$2s^2, 2p^4, 3d^0, 4f^0$
Core radius (a.u.)	<i>s</i>	1.50	1.30	1.15
	<i>p</i>	1.50	1.30	1.15
	<i>d</i>	2.00	1.30	1.15
	<i>f</i>	2.00	2.00	1.50

Table 4.1: Reference configuration and cutoff radii (in Bohr) of the pseudopotentials used in our study[74].

Junquera *et al.* used a single- ζ basis set for the semicore states of Ti and Sr, and a double- ζ plus polarisation for the valence states of all the atoms. For Sr an extra shell of 4*d* orbitals was added, and we used a minimal single- ζ set for it. All the polarisation shells were single- ζ as well. This amounts to a total of 20 orbitals for Ti, 12 orbitals for Sr and 11 orbitals for O. For all the orbitals, the cutoff radii were determined using an energy shift of 0.1 eV, and a split-norm [63] parameter of 0.2. In the generation of the basis set, the localisation radii and ionic charge for the oxygen were changed. Ordejón *et al.* [75] found it necessary to use longer radii than those determined by the parameters in Table (4.1). As in reference [75], we used 4.9 and 3.1 a.u. for first and second- ζ in the 2*s* shell, and 5.3 a.u. and 3.1 a.u. for first and second- ζ in the 2*p* shell. As the oxygen acquires a considerable ionic charge in the SrTiO₃ we used a slightly ionic configuration for that atom with a charge of -0.1*e*, as Ordejón and coworkers [75] did in the case of the BaTiO₃.

4.2 Tests for SrTiO₃

4.2.1 Lattice and elastic constants of SrTiO₃

We computed the value of the lattice constant by calculating the total energy of the bulk SrTiO₃ crystal for a range of volumes, keeping the ions fixed in the perfect cubic perovskite structure. The equilibrium lattice constant was obtained by finding the volume which minimises the total energy. The bulk modulus is calculated using

$$K_0 = V_0 \left(\frac{\partial^2 E}{\partial V^2} \right)_{V=V_0}. \quad (4.2)$$

Figure (4.2a) shows a fit to the energy as a function of the lattice constant. Our results are summarised in Table (4.2). The values obtained are in excellent agreement with those calculated with the FP-LMTO [26] method and the pseudopotential plane waves method (PWP) [70]. The first principles results are generally 1-2% smaller than the experimental values. This magnitude and sign of error are typical of total energy calculations, which tend to underestimate lattice constants as a consequence of LDA.

The C_{44} and C' elastic constants for SrTiO₃ were computed by examining the behaviour of the total energy as a function of strain. C' corresponds to a stretch along the z -axis and a contraction along the x and y directions and its strain tensor is given by

$$\alpha \begin{pmatrix} -1/2 & 0 & 0 \\ 0 & -1/2 & 0 \\ 0 & 0 & 1 \end{pmatrix}$$

where α is a real number. C_{44} corresponds to a stretch along the [111] direction of the cubic crystal and has a strain tensor given by

$$\alpha \begin{pmatrix} 0 & 1/2 & 1/2 \\ 1/2 & 0 & 1/2 \\ 1/2 & 1/2 & 0 \end{pmatrix}$$

.

¹In its cubic crystalline form, SrTiO₃ has three independent elastic constants, the so called C_{11} , C_{12} and C_{44} . C_{12} cannot be calculated using an expression like (4.3). However, we can obtain any linear combination of C_{11} and C_{12} we like. We calculated the combination $C' = \frac{1}{2}(C_{11} - C_{12})$.

The elastic constants were calculated by fitting the energy vs strain curves shown in Figure (4.2b) and using the expression

$$C = \frac{1}{3V_0} \left(\frac{\partial^2 E}{\partial \alpha^2} \right)_{\alpha=0}. \quad (4.3)$$

The values of the elastic constants and bulk modulus are presented in Table (4.2). The

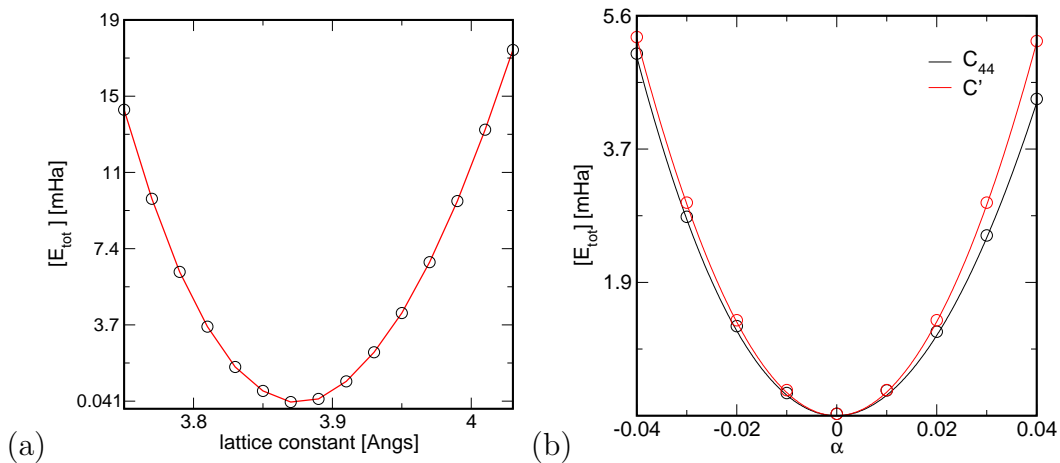


Figure 4.2: (a) fit of energy vs lattice constant. (b) shows the energy vs α curve for the elastic constants C' and C_{44} .

Method	a / Å	B / GPa	C_{44} / GPa	C' / GPa
Experimental	3.91	184	128	119
Present work	3.87	203	121	142
FP-LMTO(LDA)	3.85	200	125	140
PWP(LDA)	3.86	200	155	142

Table 4.2: Results obtained for the lattice constant (a), bulk modulus (B) and elastic constants (C_{44} and C') of bulk SrTiO_3 compared with existing results obtained from experiment [76], full-potential linear muffin tin orbitals method (FP-LMTO)[26] and the pseudo-potential plane waves method (PWP) [70]

elastic constants we have obtained for the perovskites appear to be in good agreement with previous theoretical results. Johnston [26] found a bulk modulus of 200 GPa which agrees to about 2% with the value of 203 GPa found here. King-Smith and Vanderbilt [70], using a PWP method, obtained a bulk modulus of 200 GPa, which is also about 2% smaller

than our value. The experimental values of the elastic constants for the SrTiO_3 are room temperature values obtained from the Landolt-Börnstein [76] tables. Overall, the level of agreement between theory and experiment is about 10% for the bulk modulus and C_{44} and about 25% for C' . However, we must remember that the cubic phase of SrTiO_3 is unstable. SrTiO_3 goes through an antiferrodistortive (AFD) transition at 105 K to a tetragonal phase in which the oxygen octahedra have rotated in opposite senses in neighbouring unit cells. Besides, as we can see in Figure (4.3) the measured elastic constants are quite strong functions of temperature. For example, according to the results obtained by Bell and Rupprecht [77] presented in Figure (4.3d), C_{11} increases by about 4% as temperature is lowered from room temperature to -160°C , before dropping sharply as the transition temperature is approached. The behaviour of the elastic constants near the transition temperature is depicted in Figure (4.3a) [78]. It is not clear whether a direct comparison of the theoretical and experimental elastic constants for the cubic symmetry structure is valid. In view of these uncertainties we were satisfied with the level of agreement of our calculations with previous theoretical results [26, 70].

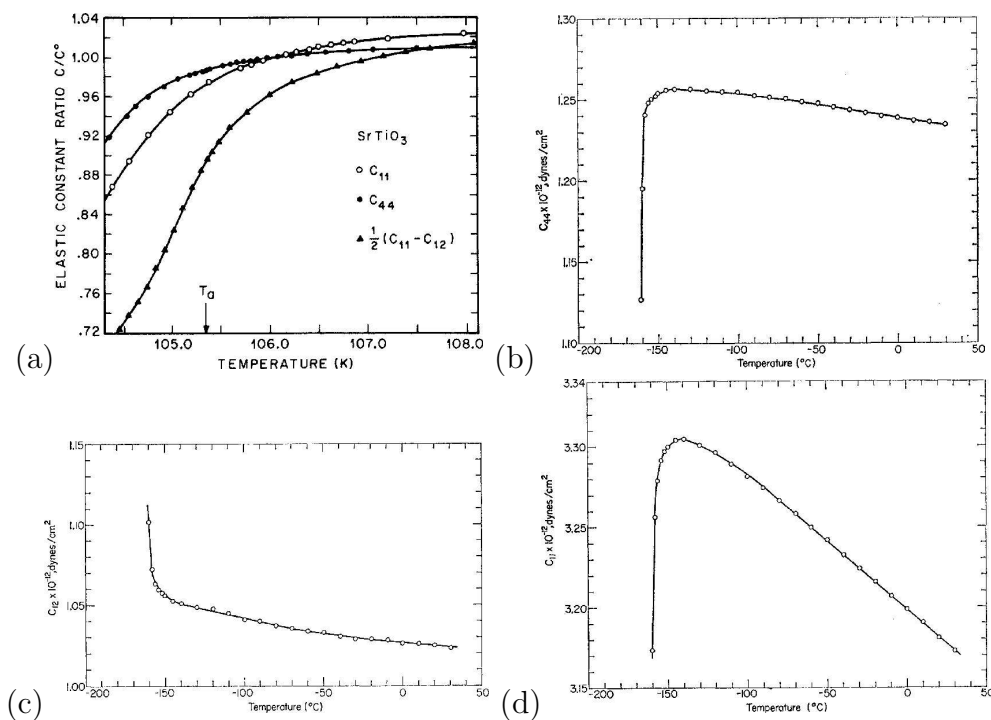


Figure 4.3: (a) temperature dependence of SrTiO_3 elastic constants in the phase transition region divided by their room temperature values C^0 [78]. (b), (c) and (d) temperature dependences of C_{11} , C_{12} and C_{44} in SrTiO_3 from -161 to 30°C [77].

4.2.2 Antiferrodistortive phase transition in SrTiO₃

The aforementioned AFD transition, obtained by freezing an AFD phonon mode at the $(111)\frac{\pi}{a}$ or R point of the Brillouin zone boundary, is showed in Figures (4.4a) and (4.4b). Sai and Vanderbilt[79] carried out a first-principles DFT study of FE and AFD instabilities

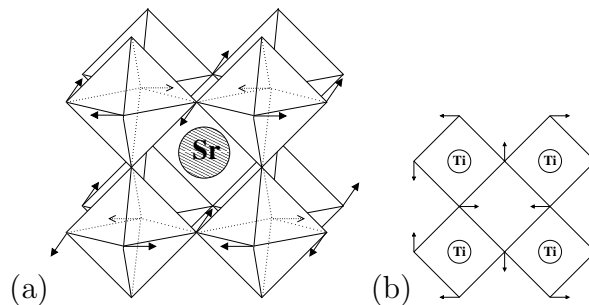


Figure 4.4: The antiferrodistortive transition of SrTiO₃ at 105 K. Consecutive oxygen octahedra tilt about the z -axis in a different sense. The figure on the right shows the transition viewed along the z -axis[26].

in tetragonal SrTiO₃. They performed calculations corresponding to the condensation of soft AFD mode at the $(110)\frac{\pi}{a}$ (or M point) and at the $(111)\frac{\pi}{a}$ (or R point) of the Brillouin zone (BZ) boundary. They found that the instability at the R point is much stronger than that at the M point. With the SrTiO₃ theoretical lattice constant, they found the equilibrium rotation angle at the R point to be $\theta_z = 5.5^\circ$, which is in excellent agreement with our results, as we can see from Figures (4.5a) and (4.5b).

4.2.3 Surface energies

As a test of the methodology, a comparison with previous calculations that used the FP-LMTO method has been made. Figure (4.6) shows the surface energies of the (1×1) and (2×1) reconstructed surfaces as a function of μ_{TiO_2} , with $T = 1000$ K and $p_{\text{O}_2} = 1$ atm. Figure (4.6a) shows calculations performed by Johnston and coworkers [36], while in Figure (4.6b) we show our calculations². Table (4.3) shows the excesses of TiO₂ and O

²The $(2\times 1)\text{TiO}_2$ surface reconstruction is not presented in Figure (4.6b). The model for this surface reconstruction was proposed by M. Castell[11] and, as we can see from Figure (4.6a), according to Johnston calculations it turned out to be very unstable. Johnston and coworkers carried out the atomistic relaxation using a Fletcher-Powell algorithm, converging the forces for the TiO₂-terminated to $0.05\text{mRy } au^{-1}$. They preserved the symmetry of the surface unit cell during the relaxation process. On the contrary, in our case no symmetry restrictions were used. This resulted in SIESTA finding a new surface unit cell for the $(2\times 1)\text{TiO}_2$, with a different symmetry for the surface unit cell and a lower surface energy. This particular

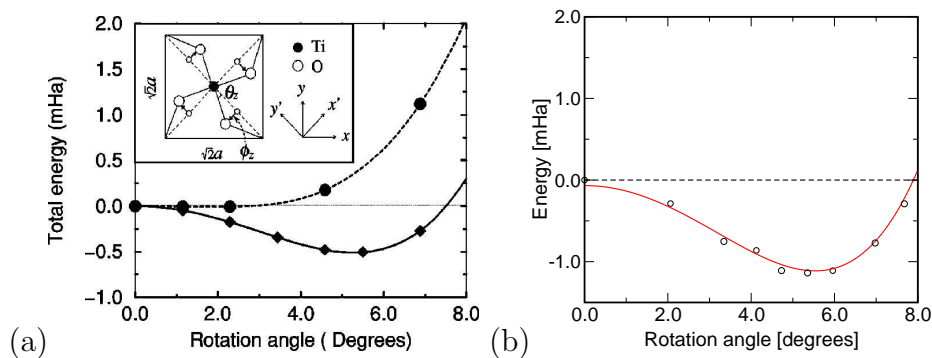


Figure 4.5: (a) Calculated values and fits of the total energy per unit cell as a function of the octahedral rotation angle θ_z , computed at the frozen theoretical cubic lattice constant, for both R point (diamonds) and M point (circles) octahedral rotation modes. θ_z is shown in the inset of Figure (a) indicating the rotation of the oxygen atoms in the TiO_2 layer[79]. (b) Our fitted values for the total energy per unit cell as a function of θ_z in the R point of the Brillouin zone.

Surface	$A_s^{(1 \times 1)} \Gamma_{\text{TiO}_2}$	$A_s^{(1 \times 1)} \Gamma_{\text{O}}$
$(1 \times 1) \text{ TiO}_2$	$\frac{1}{2}$	0
$(1 \times 1) \text{ SrO}$	$-\frac{1}{2}$	0
$(2 \times 1) \text{ TiO}_2$	0	0
$(1 \times 1) \text{ Ti}_2\text{O}_3$	$\frac{1}{2}$	$-\frac{1}{2}$
$(2 \times 1) \text{ DL-TiO}_2$	$\frac{3}{2}$	0

Table 4.3: Γ_{TiO_2} and Γ_{O} for the slabs representing the different (1×1) and (2×1) surface structures. $A_s^{(1 \times 1)}$ is the area of one of the surfaces of a (1×1) terminated slab.

with respect to SrO for the different (1×1) and (2×1) surface reconstructions considered here. The definition for these excesses are in Section (3.1.1).

The agreement between our surfaces energies and those calculated by Johnston and coworkers[36] is very good.

4.2.4 The right slab size

Figure (4.7a) shows the convergence of the unrelaxed (1×1) TiO_2 -terminated and (1×1) SrO-terminated surface energies with the number of layers in the slab. While increasing the number of layers, the number of vacuum layers was kept constant and equal to three surface reconstruction will be discussed later.

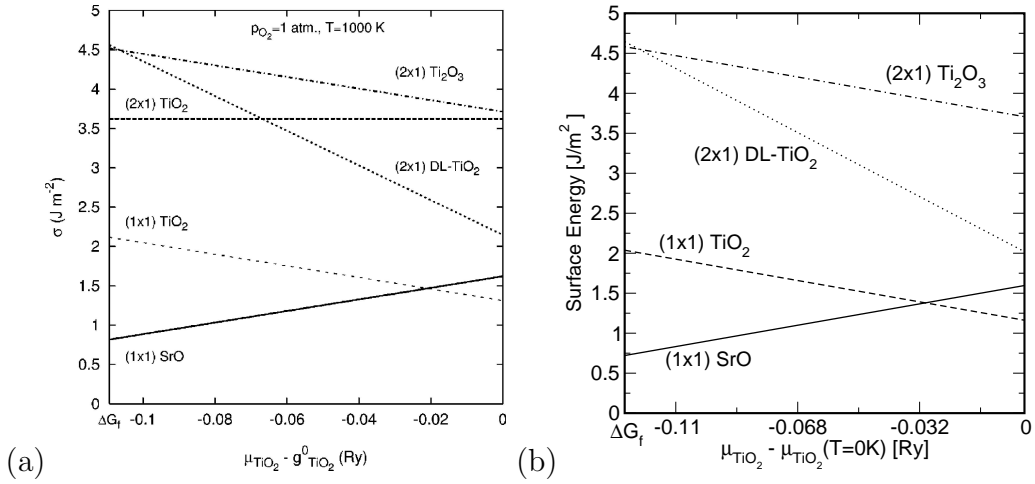


Figure 4.6: (a) Surface energies for the (1×1) and (2×1) surface structures as a function of μ_{TiO_2} at $T=1000$ K and $p_{\text{O}_2}=1$ atm, as calculated by Johnston *et al.*[36]. (b) Our results for the surface energy of the same (1×1) and (2×1) surface reconstructions under the same conditions.

because, as we can see in figure (4.7b), three vacuum layers is enough to avoid interaction between consecutive slabs. A slab with more than 7 layers would only make a difference in the surface energy of less than $0.04 \frac{\text{J}}{\text{m}^2}$ compared to 15 layers.

4.2.5 Bandstructure of SrTiO₃

Figure (4.8) shows the calculated band structure for SrTiO₃. In its stoichiometric form SrTiO₃ is a good insulator with a 3.2 eV band gap. The calculated band gap is found to be indirect from R to Γ and its value is 1.65 eV which compares very well with previous band structure calculations of Demkov *et al.* [35] 1.65 eV and Milman *et al.* [80] 1.79 eV. The LDA typically underestimates the band gap. The top of the valence band is dominated by O 2p states, and the bottom of the conduction band is due mainly to Ti 3d states. The band structure in Figure (4.8) is in excellent agreement with that calculated by Demkov *et al.* [35] and Milman *et al.* [80].

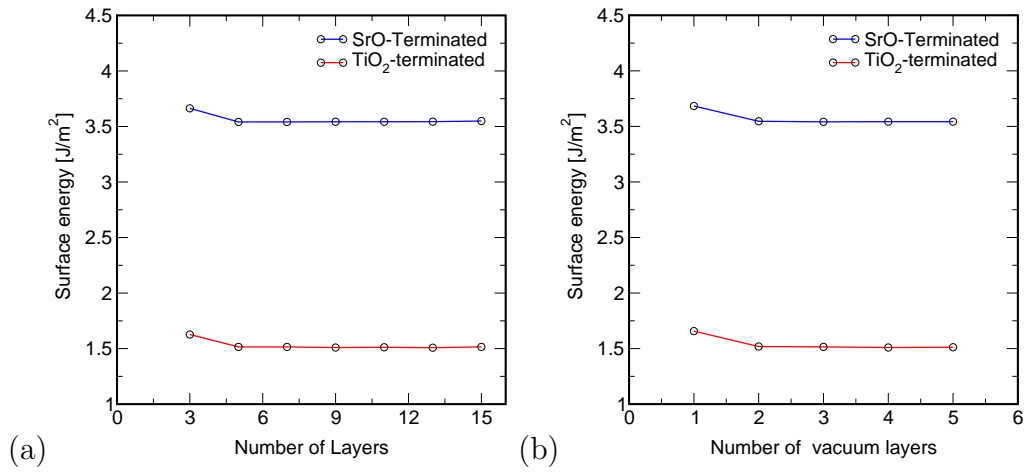


Figure 4.7: (a) Convergence of the unrelaxed (1×1) terminated surface reconstructions for SrTiO₃ with the number of layers in the slab. (b) Shows the convergence of the aforementioned surface reconstructions with the number of vacuum layers between slabs. Three vacuum layers is enough to ensure that no significant interaction between two neighbouring surfaces exists.

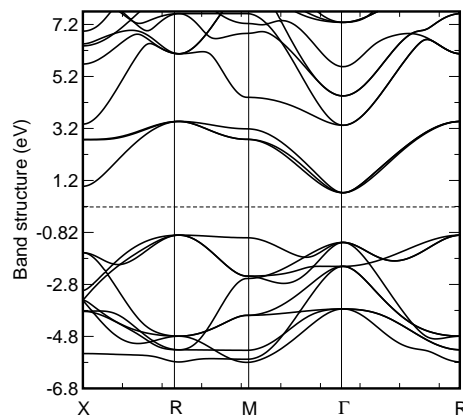


Figure 4.8: Electronic band structure of SrTiO₃ obtained with SIESTA. The dashed line indicates the Fermi level.

Chapter 5

Thermodynamics of the $\text{SrTiO}_3(001)$ surfaces

5.1 The Sr adatom model

The *Sr adatom model* was first proposed by Kubo and Nozoye in [13] as a model of the $(\sqrt{5} \times \sqrt{5})\text{-R}26.6^\circ$ surface reconstruction of $\text{SrTiO}_3(001)$ and, later, it was also used to explain almost every observed surface reconstruction on the $\text{SrTiO}_3(001)$ surface [12]. It consists of an ordered array of strontium adatoms at the oxygen four fold site of a TiO_2 -terminated layer. Figure (5.1) shows an example of the proposed Sr adatom structure for the (2×2) ($\theta=0.25$) surface reconstruction of $\text{SrTiO}_3(001)$.

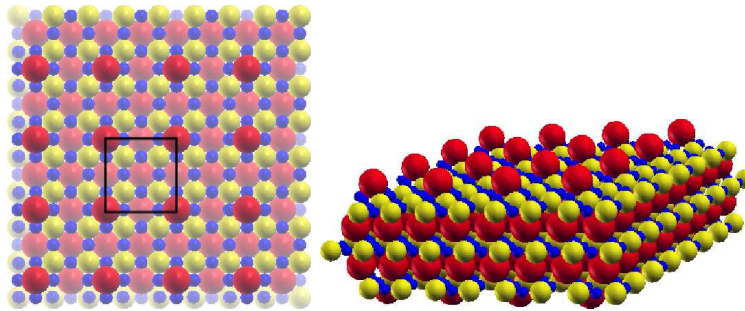


Figure 5.1: Sr adatom model for the (2×2) ($\theta=0.25$) surface reconstruction of $\text{SrTiO}_3(001)$. On the right we have an oblique view and on the left we have a top view of the proposed surface reconstruction. Ti ions are yellow, Sr ions are red and Oxygens are blue. In the top view the (2×2) surface unit cell is indicated with a black rectangle, and the atomic layer below the surface is shown with reduced depth of colour.

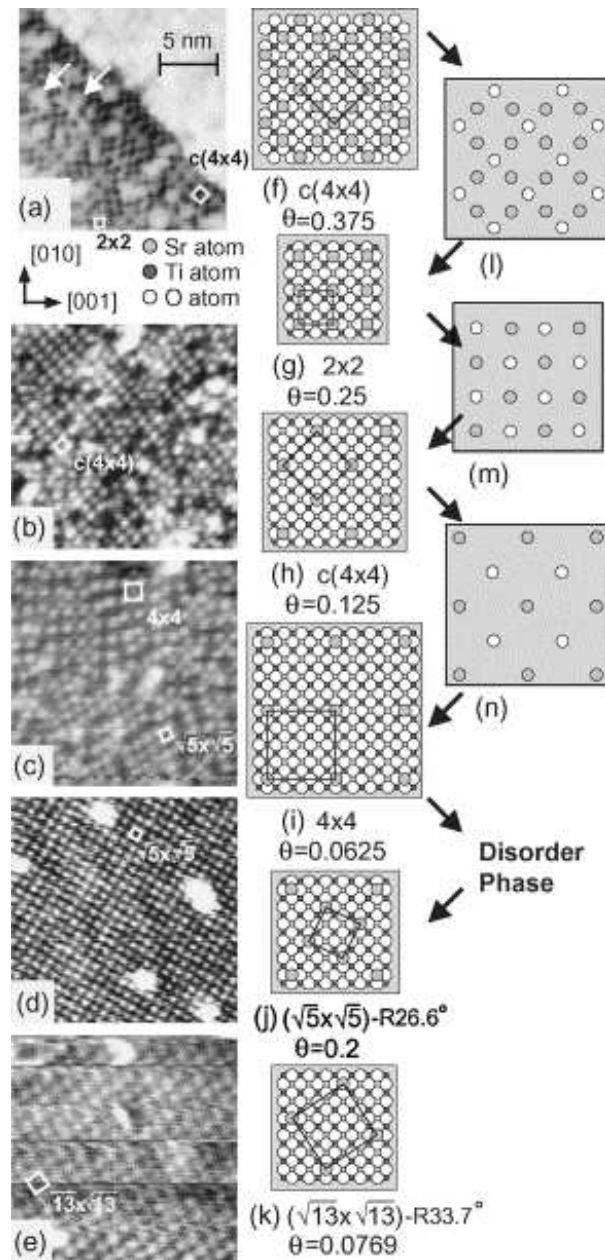


Figure 5.2: STM images of $\text{SrTiO}_3(001)$ after heating to: (a) 1000°C , (b) 1180°C , (c) 1180°C , (d) 1200°C and (e) 1250°C [12]. Proposed Sr adatom models of the $\text{SrTiO}_3(001)$ (f) $c(4\times 4)$ ($\theta=0.375$), (g) (2×2) ($\theta=0.25$), (h) $c(4\times 4)$ ($\theta=0.125$), (i) (4×4) ($\theta=0.0625$), (j) $(\sqrt{5}\times\sqrt{5})$ - $R-26.6^\circ$ ($\theta=0.2$) and (k) $(\sqrt{13}\times\sqrt{13})$ - $R-33.7^\circ$ ($\theta=0.0769$) phases[12]. (l)-(n) models to explain the structural phase transitions, all from reference[12].

The observed series of structural surface phase transitions presented in Figure (5.2), e.g., $c(4 \times 4)(\theta=0.375) \rightarrow (2 \times 2)(\theta=0.25) \rightarrow c(4 \times 4)(\theta=0.125) \rightarrow (4 \times 4)(\theta=0.0625) \rightarrow \text{disorder} \rightarrow (\sqrt{5} \times \sqrt{5})\text{-R-}26.6^\circ (\theta=0.2) \rightarrow (\sqrt{13} \times \sqrt{13})\text{-R-}33.7^\circ (\theta=0.0769)$ suggest that these reconstructions must be based on the same kind of structural model. In Figure (5.2), for the cascade of structural phase transitions from $c(4 \times 4)(\theta=0.375)$ to $(4 \times 4)(\theta=0.0625)$, Kubo and Nozoye proposed a rule to explain the decreasing in the coverage. Their model was based in the fact that the adsorption energy of alkali and alkaline-earth metals on a surface depends strongly on the amount of adsorbate present on the surface, i.e., on the surface's coverage, because of the strong dipole-dipole interaction [81]. In the case of the $c(4 \times 4)(\theta=0.375)$ phase, there are basically two kinds of Sr adatoms, e.g., atoms which have four nearest neighbor Sr adatoms, like the ones presented as open circles in Figure (5.21), and atoms which have two nearest neighbor Sr adatoms, like the ones presented as filled circles in the same Figure. The atoms, within the adsorbed layer, with four nearest neighbors Sr adatoms are the least stable ones and they desorb first. This results in the formation of the $(2 \times 2)(\theta=0.25)$ phase, as shown in Figure (5.2 m). When, in Figure (5.2 m), the atoms located at the open circle positions are removed, we are left with the $c(4 \times 4)(\theta=0.125)$ phase (Figure (5.2 n)). Finally, when the centered open-circle Sr adatoms of the $c(4 \times 4)(\theta=0.125)$ are removed in Figure (5.2 n), the $(4 \times 4)(\theta=0.0625)$ phase is formed. Therefore, this model explains all the phase transitions within non-rotated phases by only removing Sr adatoms. Rotated phases appear after heating the disordered phase at 1200°C . At first, Sr coverage increases with the formation of the $(\sqrt{5} \times \sqrt{5})\text{-R-}26.6^\circ (\theta=0.2)$ phase. Upon increasing the annealing temperature to 1250°C , Sr coverage decreased again with the formation of the $(\sqrt{13} \times \sqrt{13})\text{-R-}33.7^\circ (\theta=0.0769)$ phase. Kubo and Nozoye [12] suggested that Sr supply from the underlying bulk crystal, as well as surface migration of the Sr adatoms, played an important role in the formation of these rotated phases. Except for the $(4 \times 4)(\theta=0.0625)$ surface reconstruction, we have calculated the surface energies of all the surface reconstructions involved in the structural phase transitions. These surface structures are listed in Table (5.1) and an schematic top-view of them is presented in Figure (5.3).

With these structures, we have reproduced Kubo and Nozoye's calculations for the adsorption energies of Sr adatoms. At this point, for the sake of clarity, we introduce a new notation for the different surface reconstructions involved in the phase transitions. Since there is an ordering for the Sr coverage of each of the six structures involved, we label each surface with numbers from 0 to 5, 0 being the lowest Sr coverage and 5 the maximum.

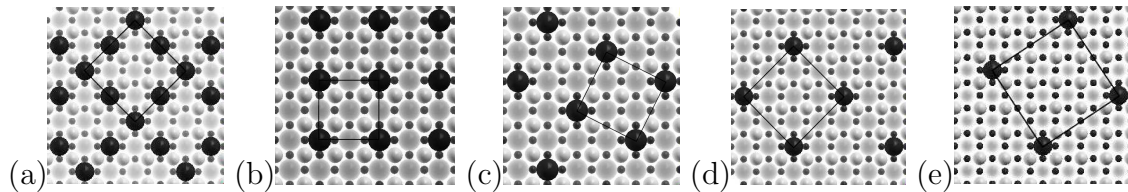


Figure 5.3: Top views of the Sr adatom model surface structures listed in Table 5.1. The black circles represent Sr adatoms and the surface unit cell is indicated in each reconstruction. The clean TiO_2 -terminated surface is the atomic layer below each reconstruction and is showed as a foggy background. (a) $c(4 \times 4)$ $\theta = 0.375$ (b) (2×2) $\theta = 0.25$ (c) $(\sqrt{5} \times \sqrt{5})$ $\theta = 0.20$ (d) $c(4 \times 4)$ $\theta = 0.125$ (e) $(\sqrt{13} \times \sqrt{13})$ $\theta = 0.0769$

Surface	N_{SrO}	$A_s^{(1 \times 1)} \Gamma_{\text{TiO}_2}$	$A_s^{(1 \times 1)} \Gamma_{\text{O}}$	θ_{Sr}	T^E [$^\circ\text{C}$]
(1×1) TiO_2	3	$\frac{1}{2}$	0	0	Not observed
$(\sqrt{13} \times \sqrt{13})$	28	$\frac{11}{26}$	$-\frac{1}{13}$	0.0769	1250
$c(4 \times 4)$	18	$\frac{3}{8}$	$-\frac{1}{8}$	0.125	1100
$(\sqrt{5} \times \sqrt{5})$	12	$\frac{3}{10}$	$-\frac{1}{5}$	0.2	1200
(2×2)	10	$\frac{1}{4}$	$-\frac{1}{4}$	0.25	1000
$c(4 \times 4)$	22	$\frac{1}{8}$	$-\frac{3}{8}$	0.375	1000

Table 5.1: N_{SrO} , Γ_{TiO_2} and Γ_{O} for the slabs representing the different surface structures. $A_s^{(1 \times 1)}$ is the area of one of the surfaces of a (1×1) terminated slab. θ_{Sr} is the coverage of Sr in the adatom model and T^E is the experimental temperature at which the surface reconstruction was observed in [12].

Table (5.2) shows this new notation. With the $\mathbf{5} \rightarrow \mathbf{4}$ phase transition we illustrate the formalism used in the calculation of the Sr adsorption energies:

$$E_d^{\mathbf{5} \rightarrow \mathbf{4}} = \frac{1}{2} [2E_{slab}(\theta = 0.25) + 2E_{Sr}^{atom} - E_{slab}(\theta = 0.375)] \quad (5.1)$$

where E_{Sr}^{atom} is the energy of an Sr atom. Table (5.3) shows the calculated adsorption energies, which are in excellent agreement with the results reported by Kubo and Nozoye in [12]. We can see from Table (5.3) that the adsorption energy shifts strongly towards lower adsorption energy values with increasing Sr coverage. This behaviour is typical for alkali and alkaline-earth-metal adsorbates on a surface [81] and is the basis for the model Kubo and Nozoye proposed to explain their experimental observations on the non-rotated surface reconstructions. The structural phase changes from high coverage phases

Surface	Sr Coverage	Label
$c(4 \times 4)$	0.375	5
(2×2)	0.25	4
$\sqrt{5} \times \sqrt{5}$	0.20	3
$c(4 \times 4)$	0.125	2
$(\sqrt{13} \times \sqrt{13})$	0.0769	1

Table 5.2: Labelling for the different surface reconstructions involved in the structural surface phase transitions.

Transition	adsorption energy [eV]	adsorption energy from[12] [eV]
$E_d^{5 \rightarrow 4}$	3.48	3.55
$E_d^{4 \rightarrow 3}$	4.73	4.80
$E_d^{3 \rightarrow 2}$	5.31	5.33
$E_d^{2 \rightarrow 1}$	6.23	not calculated

Table 5.3: Calculated Sr adsorption energies involved in the surface phase transitions.

to low coverage phases, with increasing annealing temperatures, and this indicates that the adsorption energies of Sr adatoms for the high coverage phases is lower than that for the low coverage phases.

5.1.1 Thermodynamics of the Sr adatom model

Using Equation (3.5) we calculated the surface energies of all of the Sr adatom structures listed in Table (5.1) for the allowed ranges of the variables $\mu_{\text{TiO}_2}^{\text{slab}}$, p_{O_2} and T . Phase diagrams were constructed by finding the most stable surface for each set of conditions. Limits on the $\mu_{\text{TiO}_2}^{\text{slab}}$ are set by equation (3.13). Figure (5.4a) shows the phase diagram with $\mu_{\text{TiO}_2}^{\text{slab}}$ in its lower limit. Figure (5.4b) shows the phase diagram with $\mu_{\text{TiO}_2}^{\text{slab}}$ in its upper limit. At the lower limit for $\mu_{\text{TiO}_2}^{\text{slab}}$, the value of $\mu_{\text{SrO}}^{\text{slab}}$ is at its maximum and the surface is in equilibrium with bulk SrO. As it can be seen from the figure, at high p_{O_2} and low T the clean TiO_2 terminated surface is the most stable. Upon increasing T or lowering the p_{O_2} , the Sr covered surfaces progressively decrease in surface energy, becoming more stable than the TiO_2 terminated surface. The equilibrium Sr coverage increases with increasing T and decreasing p_{O_2} . In the limit of stability of the slab, the most stable of the proposed surfaces is the one with a Sr coverage of $\theta = 0.25$ monolayers. The higher coverage structures are never stable in the allowed region, the $\theta = 0.375$ $c(4 \times 4)$ structure lying just within the

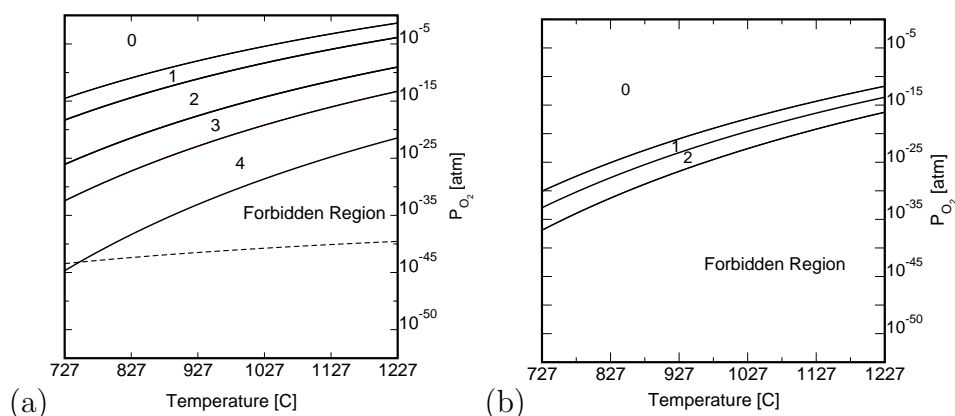
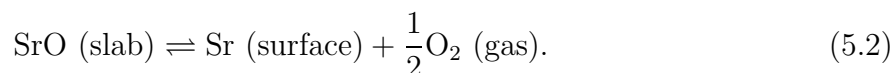


Figure 5.4: Surface phase diagram for the different Sr adatom structures as a function of temperature and partial oxygen pressure. Continuous lines separate the regions in which each structure is stable, the dashed line in figure (a) indicates the oxygen partial pressure in equilibrium with solid C. The surfaces are denoted as follows: (0) TiO_2 terminated (1×1) (1) $(\sqrt{13} \times \sqrt{13}) \theta = 0.0769$ (2) $c(4 \times 4) \theta = 0.125$ (3) $(\sqrt{5} \times \sqrt{5}) \theta = 0.20$ (4) $(2 \times 2) \theta = 0.25$.

border of the forbidden region. Figure (5.5) shows the phase diagram in a construction proposed by Van de Walle and Neugebauer [82]. In this case, the independent variables are $\mu_{\text{TiO}_2}^{\text{slab}}$ and μ_{O} . As μ_{O} decreases, it can be seen that Sr coverage increases. This ordering of stability can be explained by taking into account that SrO in the slab is in equilibrium with Sr atoms at the surface and O_2 in the gas phase:



Therefore, the chemical potentials of O_2 and Sr are related by:

$$\mu_{\text{SrO}}^{\text{slab}} = \mu_{\text{Sr}}^{\text{slab}} + \frac{1}{2} \mu_{\text{O}_2}. \quad (5.3)$$

Increasing the temperature or lowering the p_{O_2} lowers the μ_{O_2} . Similarly, a decrease in coverage of Sr in the surface lowers the $\mu_{\text{Sr}}^{\text{slab}}$. For a given $\mu_{\text{SrO}}^{\text{slab}}$, decreasing the μ_{O_2} increases the $\mu_{\text{Sr}}^{\text{slab}}$, allowing the appearance of higher coverage phases. In other words, lowering the p_{O_2} displaces the equilibrium in equation (5.2) to the right, increasing the Sr coverage. Upon decreasing the $\mu_{\text{SrO}}^{\text{slab}}$, the maximum value of $\mu_{\text{Sr}}^{\text{slab}}$ that can be achieved before reaching the forbidden region is lower and only the lower coverage surfaces are accessible. According to our results, high Sr adatom coverage can only be achieved when the surface is (or is

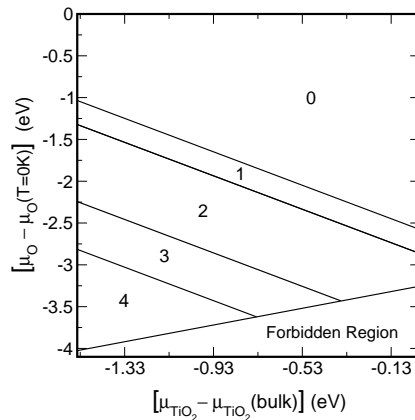


Figure 5.5: Surface phase diagram for the different Sr adatom structures as a function of μ_{O} and μ_{TiO_2} .

close to being) in equilibrium with SrO, near the lower limit of the TiO_2 chemical potential. Kubo and Nozoye's interpretation of the observed clusters being composed of SrO_x type compounds might suggest that this is the case. Another condition that our phase diagram indicates is the extremely low effective partial pressure of oxygen that can be achieved if the reducing agent carbon is present [36]. Kubo and Nozoye's preparation method uses a chemical etch that is known to leave a carbon residue [7]. In Figure (5.4(a)) the dashed line indicates the oxygen partial pressure in equilibrium with solid C as a function of temperature¹. At 726.85°C and for this oxygen pressure the $\theta = 0.25$ (2×2) structure is the most stable. At higher temperatures, but within the forbidden region, the $\theta = 0.375$ (4×4) would be in equilibrium with a metastable substrate. At temperatures above 726.85°C the lower coverage surfaces are only stable at oxygen pressures well above the 5×10^{-12} atm limit. Although the $\theta = 0.375$ $c(4 \times 4)$ and $\theta = 0.25$ (2×2) structures might be obtained at equilibrium or near-equilibrium, all lower coverage structures are unstable at the experimentally accessible conditions, with the exception of the $(\sqrt{5} \times \sqrt{5})$ $\theta = 0.20$ structure which is stable in a narrow pressure region below the ultra high vacuum (UHV) pressure at the temperatures reported by Kubo and Nozoye. Kubo and Nozoye proposed the evaporation of Sr from the surface with increasing temperature as an explanation of the decrease in coverage with temperature, and supported this by calculations of the energy

¹This pressure was calculated taking into account all equilibria between C, CO, CO_2 and O_2 , as stated in Section (3.1.3), using values for the gas reaction free energies obtained from reference [56]. A total pressure of 5×10^{-12} atm was used, which is the value reported as a higher limit during annealing in reference [12].

required to desorb Sr atoms. Our results are only consistent with their interpretation if we assume that the system is not in equilibrium [83].

5.1.2 Brief discussion on the kinetics of the Sr adatom model

A strong point in favour of the model is its ability to explain the kinetics of the observed surface phase transitions. Table (5.3) shows the adsorption energies for Sr adatoms, which are above $50 \frac{\text{KJ}}{\text{mol}}$ ($3.12 \frac{\text{eV}}{\text{atom}}$) and, therefore, we assume chemisorption is taking place at the surface. Kubo and Nozoye [12] interpreted their adsorption energies in terms of a Temperature Programmed Desorption (TPD) [32] process, although they did not actually carry out the corresponding experiment. TPD techniques are used for the determination of kinetic and thermodynamic parameters of desorption processes. A sample is heated using a temperature program, which usually vary T as a linear function of time, and the partial pressures of atoms and molecules that desorb from the sample are measured, e.g. by mass spectrometry. Thermal Desorption Spectroscopy (TDS) is when these experiments are performed, using surfaces of single-crystalline samples, in a ultra-high vacuum (UHV) chamber. The interpretation of the spectral data related with the pressure is commonly interpreted using the *Polanyi-Winger* equation

$$r_{des} = -\frac{d\Theta}{dt} = \nu_n(\Theta) \exp\left(-\frac{\Delta E_{des}(\Theta)}{RT}\Theta^{n(\Theta)}\right) \quad (5.4)$$

where r_{des} is the desorption rate, Θ is the Sr's instantaneous coverage, $\nu_n(\Theta)$ is the frequency factor, $n(\Theta)$ is the kinetic desorption order and $\Delta E_{des}^{PW}(\Theta)$ is the desorption energy. These are called the *activation parameters* and are usually dependent on the surface coverage Θ and can also depend on the temperature itself. Modern alternatives to the interpretation by means of the Polanyi-Wigner equation are based on the simulation of desorption spectra with complex statistical models for the interactions experienced by the adsorbate. As a first approximation, if we assume (as Kubo and Nozoye did [12]) that the activation parameters ν_n and n are independent of the coverage Θ and that the heating rate β is constant, we can calculate the temperature of the desorption rate maximum T_{max} using

$$\frac{\Delta E_{des}}{RT_{max}^2} = \frac{1}{\beta} \nu_n n \Theta^{n-1} \cdot \exp\left(-\frac{\Delta E_{des}}{RT_{max}}\right) \quad (5.5)$$

Kubo and Nozoye [12] used Redhead [84] analysis of Equation (5.5). Redhead assumed that desorption followed first order kinetics ($n = 1$), then Equation (5.5) can be written

$$\frac{\Delta E_{des}}{RT_{max}^2} = \frac{1}{\beta} \nu_n \exp\left(-\frac{\Delta E_{des}}{RT_{max}}\right). \quad (5.6)$$

Kubo and Nozoye solved this equation for T_{max} assuming $\beta = 0.1 \frac{\text{K}}{\text{s}}$ and $\nu = 1 \times 10^{-13} \frac{1}{\text{s}}$. The values for ΔE_{des} were taken from Table (5.3). For each of the surface phase transitions represented in Table (5.3) the values of T_{max} compare very well with experimental results [12].

5.2 The Double-layer model and the (2×1) and $c(4 \times 2)$ surface reconstructions

The *double layer model* was introduced by Erdman and coworkers to examine the (2×1) [15] and the $c(4 \times 2)$ [16] surface reconstructions of the $\text{SrTiO}_3(001)$ surface. In this model of the surface reconstruction there is a double layer TiO_2 termination. We might think of the surface reconstruction as a surface rearrangement of TiO_{6-x} units into edge-sharing blocks. This would determine the SrO-deficient surface structure of $\text{SrTiO}_3(001)$. The strong point in favour of this particular model is that, from the experimental methodology used by Erdman and coworkers, the surface structure can be partially solved, i.e. the type and (x, y) coordinates of the atoms on the first and second layer of the surface reconstruction can be obtained. The z positions were estimated using *ab initio* calculations. Figure (5.6) shows the double layer model of a $c(4 \times 2)$ surface reconstruction in the $\text{SrTiO}_3(001)$ surface.

5.2.1 Vibrational contributions in the double-layer model

Recalling the general expression for the surface energy (3.17)

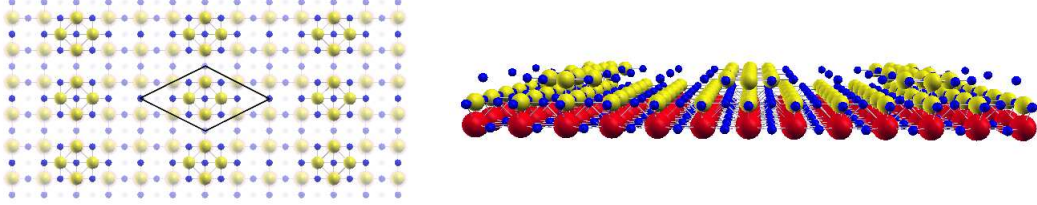


Figure 5.6: Double layer model for the $c(4 \times 2)$ surface reconstruction of $\text{SrTiO}_3(001)$. On the right we have an oblique view and on the left we have a top view of the proposed surface reconstruction. Ti ions are yellow, Sr ions are red and Oxygens are blue. In the top view the $c(4 \times 2)$ surface unit cell is indicated with a black rhombus. The atomic layer below the surface is shown with reduced depth of colour and it is a $(1 \times 1)\text{TiO}_2$ -terminated surface.

$$\begin{aligned}
\sigma(\mu_{\text{TiO}_2}, p_{\text{O}_2}, T) &= \\
&= \frac{1}{2A_s} \underbrace{\left(E_{0\text{K}}^{\text{slab}} - N_{\text{SrO}} E_{\text{SrTiO}_3}^{\text{bulk}} - \Gamma_{\text{TiO}_2} E_{\text{TiO}_2}^{\text{bulk}} \right)}_{\text{surface energy at 0K}} + \\
&\frac{1}{2A_s} \underbrace{\left(F_{\text{Vib}}^{\text{slab}}(T) - N_{\text{SrO}} F_{\text{SrTiO}_3}^{\text{bulk}}(T) - \Gamma_{\text{TiO}_2} F_{\text{TiO}_2}^{\text{bulk}}(T) \right)}_{\text{surface vibrational free energy}} + \\
&\frac{1}{2A_s} \left(p(V^{\text{slab}} - N_{\text{SrO}} V_{\text{SrTiO}_3}^{\text{bulk}}) - \Gamma_{\text{TiO}_2} V_{\text{TiO}_2}^{\text{bulk}} \right) - \\
&\Gamma_{\text{O}} \mu_{\text{O}}(p_{\text{O}_2}, T)
\end{aligned} \tag{5.7}$$

we might say that the term labelled *surface vibrational free energy* represents the relevant temperature-dependent vibrational contributions to the surface free energy. The experimental temperatures considered here are of the order of 1500 K, which is almost two thirds of the melting point of SrTiO_3 . In Section (3.1.1) we have estimated these vibrational contributions. With the exception of the $c(4 \times 2) DL - \text{TiO}_2 B$ surface reconstruction, it was concluded that, for the 1000-1500K temperature range, these contributions are negligible for the calculation of the surface free energy of the $\text{SrTiO}_3(001)$ reconstructions studied

here.

However, for the particular surface reconstructions studied with the double layer model it has been proposed that, as uncoordinated Ti is hardly avoidable near any surface, it may well be that it is the ability of the different types of surface oxygens to locally stabilise under coordinated Ti sites that decides the relative stability of competing reconstructions [16]. This “ability” is given by the structural flexibility of the surface reconstruction, which is largely provided by the so called “floating-type” oxygens at the surface. To estimate the contribution of these floppy oxygens to the surface vibrational free energy we have improved the Einstein model used in Section (3.1.1). As before, we treated these oxygens as Einstein oscillators but calculated their associated frequency in a different way.

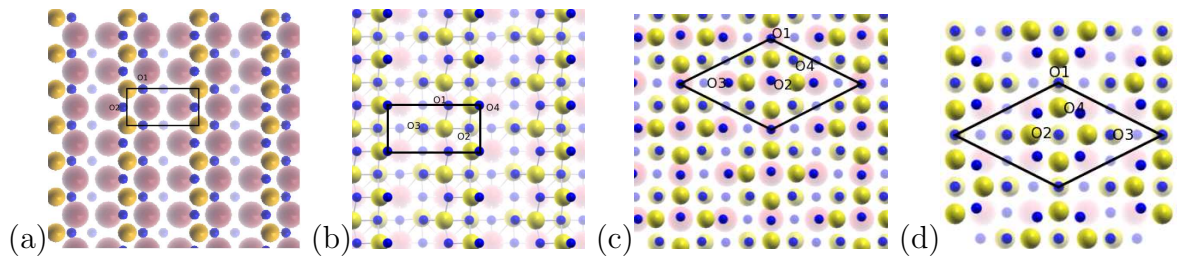


Figure 5.7: Top views of the studied surface reconstructions. (a) the (2×1) SL- TiO_2 surface reconstruction. This reconstruction was obtained by SIESTA when relaxing the (2×1) SL- TiO_2 proposed by M. Castell [11]. This surface reconstruction has two types of surface floppy oxygens. (b)-(d) Top views of the (2×1) DL- TiO_2 and $c(4\times 2)$ DL- TiO_2 -A/B double-layer surface reconstructions proposed by Erdman *et al.* [15, 16]. We have labelled each one of the four different surface floppy oxygens on each of these double layer reconstructions.

Starting from the equilibrium configuration, we displaced every type of surface oxygen, one at a time, along the three spatial directions a distance of $h=0.026 \text{ \AA}$, which was small enough to ensure we are within the harmonic regime. At each extreme point of these displacements, we calculated the forces acting on the displaced oxygen atom from first principles, and we used these forces to calculate the force constant matrix \mathbf{K}

$$\mathbf{K} = \begin{pmatrix} \frac{\partial F_x}{\partial x} & \frac{\partial F_x}{\partial y} & \frac{\partial F_x}{\partial z} \\ \frac{\partial F_y}{\partial x} & \frac{\partial F_y}{\partial y} & \frac{\partial F_y}{\partial z} \\ \frac{\partial F_z}{\partial x} & \frac{\partial F_z}{\partial y} & \frac{\partial F_z}{\partial z} \end{pmatrix}. \quad (5.8)$$

Equation (5.9) is an example of how we calculated each element of the force constant matrix \mathbf{K} at a generic point (x_0, y_0, z_0)

$$\frac{\partial F_x(x_0, y_0, z_0)}{\partial x} = \frac{F_i(x_0 + h, y_0, z_0) - F_i(x_0 - h, y_0, z_0)}{2h}. \quad (5.9)$$

Each floppy oxygen i in every proposed surface reconstruction have an associated \mathbf{K} matrix, which we use to obtain the Einstein vibrational modes with associated frequencies $\omega_{O_i}^j$ (See Appendix). As each oxygen O_i is treated as a three-dimensional Einstein oscillator with normal modes $\omega_{O_i}^j$, the total Helmholtz vibrational free energy at temperature T of N of these superficial floppy oxygens, is given by

$$F_{O_i}^{\text{Vib}}(T) = \sum_{i=1}^N \sum_{j=1}^3 \left[\frac{\hbar \omega_{O_i}^j}{2} + k T \text{Ln} \left(1 - e^{-\left(\frac{\hbar \omega_{O_i}^j}{kT}\right)} \right) \right]. \quad (5.10)$$

We have assumed that the vibrational contribution is due only to the oxygens and there are basically three different types of them, namely:

- Bulk SrTiO_3 oxygens: O_{SrTiO_3}
- Bulk TiO_2 oxygens: O_{TiO_2}
- Surface oxygens: O_{surf} .

The former ones were labelled in Figure (5.7). If we now take the *vibrational* contribution from (5.7), and express each of its components in terms of equation (5.10), we obtain an analytical expression for the vibrational contribution. For the $(2 \times 1)\text{TiO}_2\text{SL}$ this expression looks like

$$\begin{aligned} \sigma_{\text{Vib}}(T) &= \sum_{i=1}^4 F_{\text{Vib}}^{\text{O}_{\text{surf}}^i}(T) - 4F_{\text{Vib}}^{\text{O}_{\text{SrTiO}_3}}(T) = \\ &= \sum_{i=1}^4 \sum_{l=1}^3 \left[\frac{\hbar}{2} \omega_l^i + \ln \left(1 - e^{-\left(\frac{\hbar \omega_l^i}{kT}\right)} \right) \right] - \\ &4 \sum_{l=1}^3 \left[\frac{\hbar}{2} \omega_l^i + \ln \left(1 - e^{-\left(\frac{\hbar \omega_l^i}{kT}\right)} \right) \right]. \end{aligned} \quad (5.11)$$

We have calculated the vibrational contributions in the $c(4 \times 2)$ DL- TiO_2 -A/B, (2×1) DL- TiO_2 and (2×1) SL- TiO_2 surface reconstructions. In Figures (5.7a-d) we have labelled the

different surface floppy oxygens in each of the aforementioned surface reconstructions. The expressions for the $c(4\times 2)$ DL- TiO_2 -A/B and (2×1) DL- TiO_2 are in the Appendix. Figure (5.8) shows the temperature dependence of the vibrational contributions for all the double layer surface reconstructions studied in this dissertation.

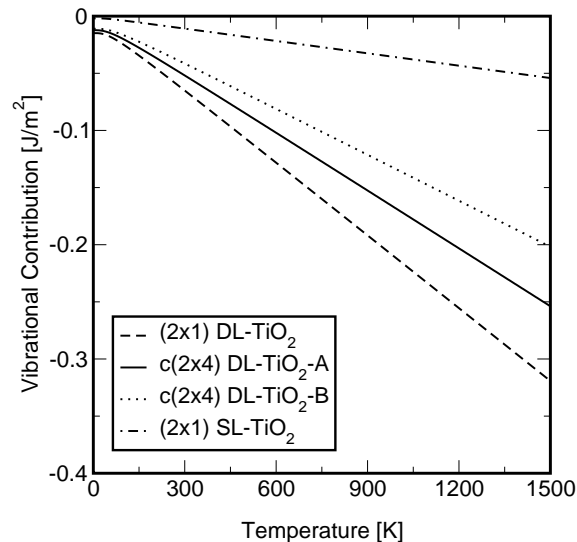


Figure 5.8: Temperature dependence of the vibrational contributions due to the floppy oxygens of each of the surface reconstructions studied here.

Discussion on the vibrational contribution

If we compare the vibrational contributions to the surface energy of reconstructions $c(4\times 2)$ DL- TiO_2 -A, (2×1) DL- TiO_2 and (2×1) SL- TiO_2 from Figures (3.1) and (5.8), we note that in Figure (3.1) these contributions are all positive, while in Figure (5.8) they are all negative. The approximations used in Figures (3.1) and (5.8) are both Einstein models: we approximate the Ti, Sr and O vibrational modes by characteristic frequencies. In Figure (3.1) the characteristic frequencies are estimated following the procedure explained in the Appendix. This procedure is an improvement of the methodology proposed by K. Reuter and M. Scheffler [38]: we pick the values of the characteristic bulk frequencies of Sr, Ti and O from phonon dispersion curves of bulk TiO_2 rutile and SrTiO_3 , and allow a 50% variation of these values at the surface layer². In Figure (5.8), the vibrational contributions to the surface energy are shown, which were calculated with the procedure explained in

²These particular values for the characteristic frequencies are not well justified, they should be considered as rough estimates of the vibrational contributions. see the Appendix for more details.

Section (5.2.1).

According to Table (3.1), vibrational contributions are negative and this is a general feature of vibrational contributions to the surface energy. Moreover, these vibrational contributions decrease (negatively increase) linearly with temperature [85]. Therefore, we could say that the vibrational contributions depicted in Figure (5.8) are more realistic, compared with the correspondent ones in Figure (3.1). One of the reasons for this could be that the model used in Figure (5.8) takes into account the symmetry of the atoms in the slab. This can be seen in the Tables at the Appendix, where the Einstein frequencies of some of the surface oxygens are clearly lower than the frequencies of bulk oxygens.

5.2.2 The (2×1) and $c(4 \times 2)$ surface reconstructions

In Section (5.1) we studied different surface reconstructions that were explained using patterns of Sr adatoms on a TiO_2 terminated (1×1) surface. In this Section, we focus on the possible origin and atomic structure of the (2×1) and $c(4 \times 2)$ surfaces. We also discuss the possibility that there may be more than one reconstruction with a (2×1) or $c(4 \times 2)$ surface unit cell.

The (2×1) reconstruction

In Figure (5.9) we can see the four candidate structures for the (2×1) surface reconstruction. Figure (5.9a) shows the double layer model of the (2×1) surface proposed by Erdman *et al* [15]. The top layer has a TiO_2 stoichiometry, with half of the TiO_5 displaced along the $[110]$ direction. The result is a row of 5-coordinated TiO_5 that shares edges between them as well as with the layer underneath, which is a part of the first full intact TiO_2 layer of SrTiO_3 with 6-coordinated Ti atoms. In the surface layer we can distinguish (See Figure (5.7b)) between two different types of oxygen atoms: (1) *internal* O atoms (O1, O2) tightly bound inside the surface rows and shared between the octahedra; and (2) *external* O atoms (O3, O4), not shared between the octahedra.

In Figure (5.9b) we see the proposed (2×1) Sr adatom structure proposed by Kubo and Nozoye [12]. This surface structure was not experimentally observed by Kubo and Nozoye, they proposed it to explain the structural surface phase transition from the (2×1) to the

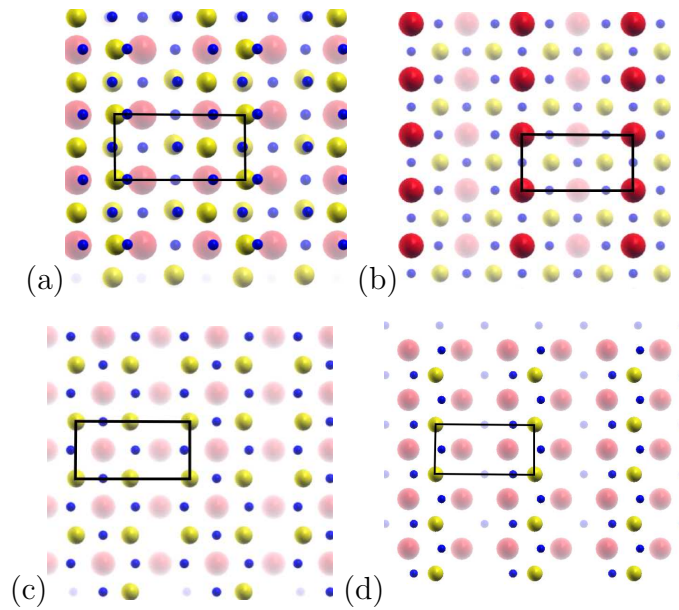


Figure 5.9: Four candidate structures proposed for the (2×1) surface reconstruction. (a) the double layer model of the (2×1) surface reconstruction proposed by Erdman *et al*[15]. (b) the Sr adatom model for (2×1) surface reconstruction proposed by Kubo and Nozoye[12]. (c) M. Castell's proposed structure of the (2×1) reconstructed surface with Ti_2O_3 stoichiometry [11]. (d) the (2×1) surface reconstruction proposed by me. This structure has TiO_2 stoichiometry.

$c(4 \times 4)$ surface reconstructions -observed by Castell [11]- using the Sr adatom model. The aforementioned phase transition was observed by M. Castell, and occurred on annealing the (2×1) surface reconstruction at a temperature of around 900°C for 30 min.

Figure (5.9c) shows one of the (2×1) reconstructions proposed by Castell [11]. It was created by removing a $[010]$ row of O ions from the TiO_2 -terminated (1×1) surface. This reconstruction has a reduced surface stoichiometry of Ti_2O_3 . The reconstruction in Figure (5.9d) has TiO_2 stoichiometry with half the Ti and O coverage of the TiO_2 -terminated (1×1) surface. A surface reconstruction with identical stoichiometry but different symmetry was proposed by Castell [11]. When we performed the atomistic relaxation of this (2×1) surface reconstruction proposed by Castell, we found that the relaxation process led us to the surface geometry showed in Figure (5.9d).

The surface structure models proposed by Castell and Erdman *et al* were based on experimental evidence. Figure (1.2) in Section (1) is a STM image of the (2×1) reconstructed surface obtained by Castell [11]. As regards the experimental evidence obtained by Erdman *et al*, it is worth describing in more detail experimental methodology they used, which

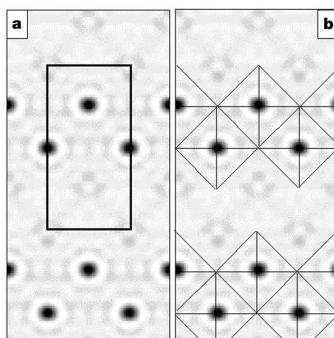


Figure 5.10: Theoretical direct methods solution of the (2×1) structure. (a) the calculated scattering potential map and the primitive unit cell is indicated with solid lines. (b) an interpretation of the map in terms of TiO_x units, where the black spots are regions of high potential -that is possible atomic sites- which subsequent analysis demonstrated were Ti atoms[15].

was already mentioned in Section (5.2). The aforementioned experimental methodology consists in a combination of high-resolution electron microscopy and theoretical crystallographic direct methods for surfaces [86]. These methods referred as direct methods are diffraction techniques which provide a powerful tool for the solution of surface structures and refinement of atomic positions. In a diffraction experiment, the amplitude of the reflections are recorded, but the phase information is lost, preventing a direct Fourier inversion of the data. The approach proposed by Erdman *et al* solves the phase problem [86, 87], generating a set of plausible solutions for the structures starting only from the intensity data. Effectively, this methodology produces an estimate two-dimensional map of the scattering potential that originated the surface electron diffraction. Peaks in this map correlate with the true atomic positions with relatively small errors, typically less than 0.1 \AA . Figure (5.10) shows an example of this for the (2×1) surface reconstruction.

Finally, in Figure (5.11) we have another double layer surface reconstruction called $(\sqrt{2} \times \sqrt{2})R45^\circ$. This reconstruction has a surface unit cell with TiO_2 stoichiometry in which Ti atoms are arranged in diagonal rows. It is clear from the picture that this surface reconstruction does not have a unit cell with a (2×1) periodicity. However, this reconstruction turned out to be very stable, and we will see that due to electronic structure effects, the geometric pattern of bright spots obtained by STM is very different from the physical geometry of the reconstruction.

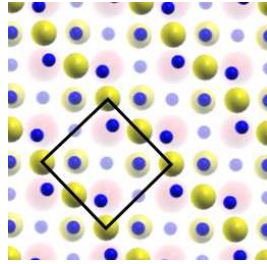


Figure 5.11: Top view illustrating the $(\sqrt{2} \times \sqrt{2})R45^\circ$ surface reconstruction.

The $c(2 \times 4)$ reconstruction

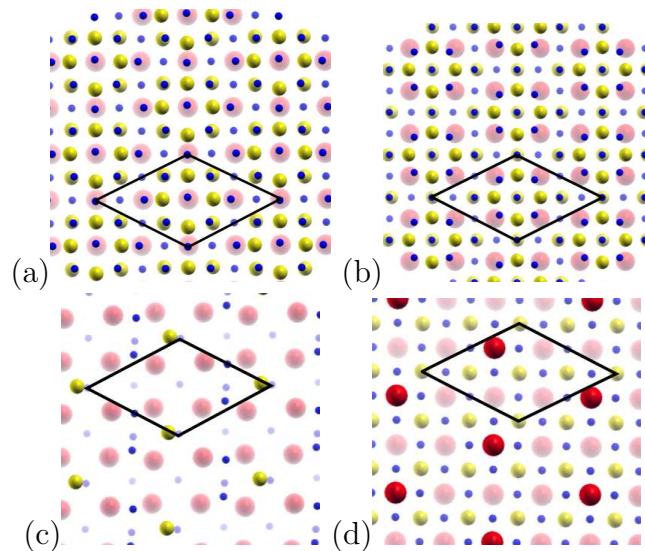


Figure 5.12: Four candidate structures proposed for the $c(2 \times 4)$ surface reconstruction. (a) and (b) are the two double layer model proposed by Erdman *et al*[16]. (c) is the model proposed by Castell[11] and (d) is the Sr adatom model.

Figure (5.12) shows the four proposed structures for the $c(4 \times 2)$ surface reconstruction that we studied in this work.

Figures (5.12a) and (5.12b) are the $c(4 \times 2)$ surface reconstructions proposed by Erdman *et al.* [16]. Figure (5.13) shows the two-dimensional map of the scattering potential that originated the surface electron diffraction, obtained through crystallographic direct methods [16]. Again, the black spots in this figure are regions of high potential and are correlated with the Ti atoms. These surface structures consist of a combination of edge sharing TiO_x

units with four Ti atoms in each unit. However, this surface layer could be attached to the underlying bulk layer in two different ways. Bearing in mind the coordination requirements for perovskite structures, as well as the (2×1) surface reconstruction previously mentioned, these two possible configurations of the over-layer with respect to the bulk are the ones schematically illustrated in Figures (5.12a) and (5.12b).

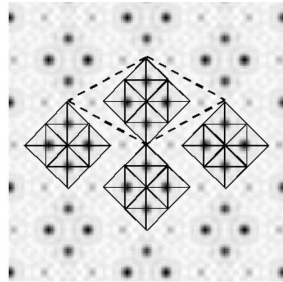


Figure 5.13: Theoretical direct-method solution of the $c(4 \times 2)$ structure[16]. It shows the scattering potential map and the primitive unit cell is indicated with solid lines. The dark features were determined to be Ti sites. The scattering potential map is interpreted in terms of TiO_x pseudo-octahedral units.

Figure (5.12c) is the surface structure for the $c(4 \times 2)$ reconstruction proposed by Castell [11].

The Sr adatom model for the $c(4 \times 2)$ surface reconstruction is shown in Figure (5.12d). This surface reconstruction was observed by Kubo and Nozoye after annealing the sample at 800°C for one hour in UHV, exposed it to air for several minutes, and annealing again in UHV, at 1000°C , for several seconds [12].

5.2.3 Thermodynamics of the (2×1) and $c(4 \times 2)$ surface reconstructions

Table (5.4) lists all the proposed model for the $c(4 \times 2)$ and (2×1) surface reconstructions. Using expression (3.17), the surface energies of all the listed structures were calculated for the allowed ranges of the variables $\mu_{\text{TiO}_2}^{\text{slab}}$ and p_{O_2} , while T was kept constant and equal to 1000 K . Table (5.4) shows that Γ_{O} is zero for almost all the surface reconstructions. This means that the surface energy of those reconstructions does not depend on either p_{O_2} or T . Therefore, constructing phase diagrams -like the ones showed in Figure (5.4)- would have been inappropriate, because only the most stable of all the reconstructions with $\Gamma_{\text{O}} = 0$

would have been observed in those diagrams. To properly account for the changes on the surface energy of all the structures depicted in Table (5.4), we chose to plot the surface energies with $T = 1000 \text{ K}$, for $\mu_{\text{TiO}_2}^{\text{slab}}$ on its lower and upper limits and with p_{O_2} ranging from 1 atm to $1 \times 10^{-40} \text{ atm}$.

Surface	$A_s^{(1 \times 1)} \Gamma_{\text{TiO}_2}$	$A_s^{(1 \times 1)} \Gamma_{\text{O}}$
(1×1) SrO	$\frac{1}{2}$	0
(1×1) TiO ₂	$-\frac{1}{2}$	0
c(4×2) TiO ₂ -DL(A)	$\frac{3}{2}$	0
c(4×2) TiO ₂ -DL(B)	$\frac{3}{2}$	0
c(4×2) TiO ₂ -SL	$-\frac{1}{4}$	0
c(4×2) Sr adatom	$\frac{1}{4}$	$-\frac{3}{2}$
(2×1) TiO ₂ -DL	$\frac{3}{2}$	0
(2×1) TiO ₂ -DL1	$\frac{3}{2}$	0
(2×1) TiO ₂ -SL	0	0
(2×1) Ti ₂ O ₃	$\frac{1}{2}$	$-\frac{1}{2}$
(2×1) Sr adatom	0	2

Table 5.4: Γ_{TiO_2} and Γ_{O} for the slabs representing the different surface structures. $A_s^{(1 \times 1)}$ is the area of one of the surfaces of a (1×1) terminated slab. (2×1) TiO₂-DL1 labels the $(\sqrt{2} \times \sqrt{2})R45^\circ$ reconstruction.

The (2×1) reconstruction

Figures (5.14a) and (5.14b) show the surface energies for the (2×1) surface reconstructions. In Figure (5.14a) the surface reconstructions are in equilibrium with SrO - $\mu_{\text{TiO}_2}^{\text{slab}}$ is in its lower limit. Figure (5.14b) shows the surface reconstructions with $\mu_{\text{TiO}_2}^{\text{slab}}$ in its upper limit: the reconstructions are in equilibrium with TiO₂. Limits on $\mu_{\text{TiO}_2}^{\text{slab}}$ are set up by Equation (3.13). Equation (3.3) relates $\mu_{\text{TiO}_2}^{\text{slab}}$ with μ_{O_2} . Therefore, there are limits for the μ_{O_2} and these limits are transformed into p_{O_2} limits through Equation (3.19). Thus, in equilibrium with SrO, p_{O_2} can be as low as 10^{-45} atm . On the other hand, in equilibrium with TiO₂, p_{O_2} can not be below 10^{-37} atm .

As was observed by Johnston and coworkers [36], the (1×1) surfaces are very stable ones. In equilibrium with TiO₂ the (1×1) SrO and TiO₂ terminated surfaces are more stable

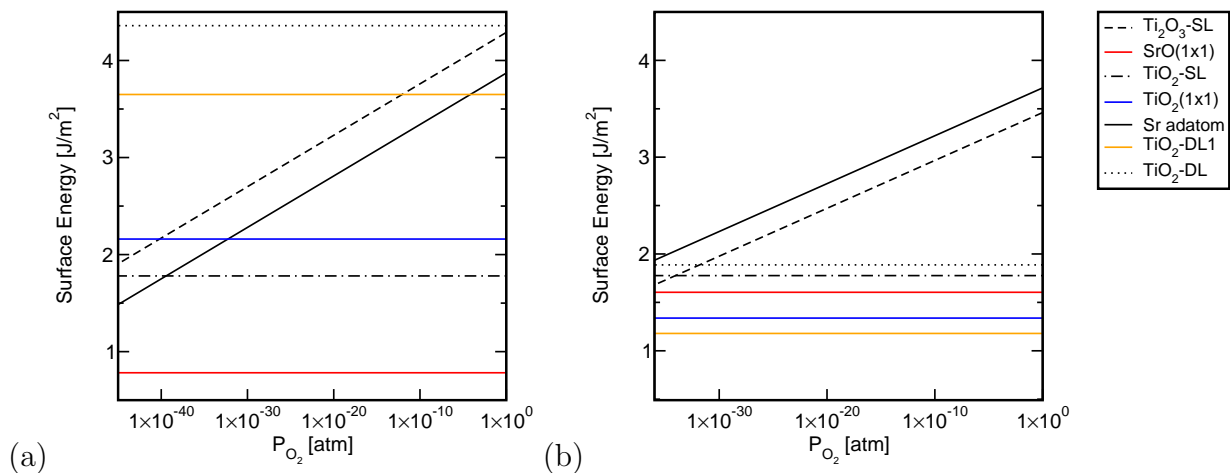


Figure 5.14: Surfaces energies for all the proposed atomic scale models of the (2×1) surface reconstructions. Surface energies are expressed as functions of p_{O_2} at $T = 1000\text{ K}$. In (a) the reconstructions are in equilibrium with SrO and in (b) with TiO_2 . The labelling is as follows: $\text{TiO}_2\text{-DL}$ → Figure (5.9a), Sr adatom→ Figure (5.9b), $\text{Ti}_2\text{O}_3\text{-SL}$ → Figure (5.9c), $\text{TiO}_2\text{-SL}$ → Figure (5.9d), $\text{TiO}_2\text{-SL1}$ → Figure (5.11).

than any of the (2×1) reconstructions for all the allowed values of p_{O_2} at $T = 1000\text{ K}$. In equilibrium with SrO, the (1×1) TiO_2 terminated surface is not as stable as before -for instance, the (2×1) $\text{TiO}_2\text{-SL}$ reconstruction is more stable-. However, the most stable reconstruction in equilibrium with SrO, for all the allowed values of p_{O_2} at $T = 1000\text{ K}$, is the (1×1) SrO terminated surface. Despite the stability of the (1×1) surfaces there are no atomic resolution STM images. According to Johnston *et al.* [36] the (1×1) SrO terminated surface is too electronically flat to allow atomic resolution STM imaging. Their density of states plots suggest that it is easier to obtain atomic resolution STM images from the (1×1) TiO_2 terminated surface. Alternatively, Johnston *et al* [36] also suggest that is quite possible that a perfect (1×1) reconstruction is stable in UHV conditions, but as soon as an oxygen atom is lost into the vacuum this results in local (2×1) ordering.

Figure (5.14) show a particular surface reconstruction in equilibrium with TiO_2 : the $(\sqrt{2}\times\sqrt{2})R45^\circ$ reconstruction. As we already mentioned, this surface reconstruction does not have the required geometrical periodicity, but its simulated STM image is close to the experimentally observed one. The surface energy of this reconstruction is independent of both T and p_{O_2} and its stability does not depend on neither of these environmental parameters.

The $c(4 \times 2)$ reconstruction

In Figures (5.15a) and (5.15b) we have the surface energies for the $c(4 \times 2)$ surface reconstructions. Limits for the $\mu_{\text{TiO}_2}^{\text{slab}}$ and p_{O_2} are as stated for the (2×1) surface reconstruction. Again, the (1×1) surfaces are very stable. In both equilibria, it is a (1×1) unrecon-

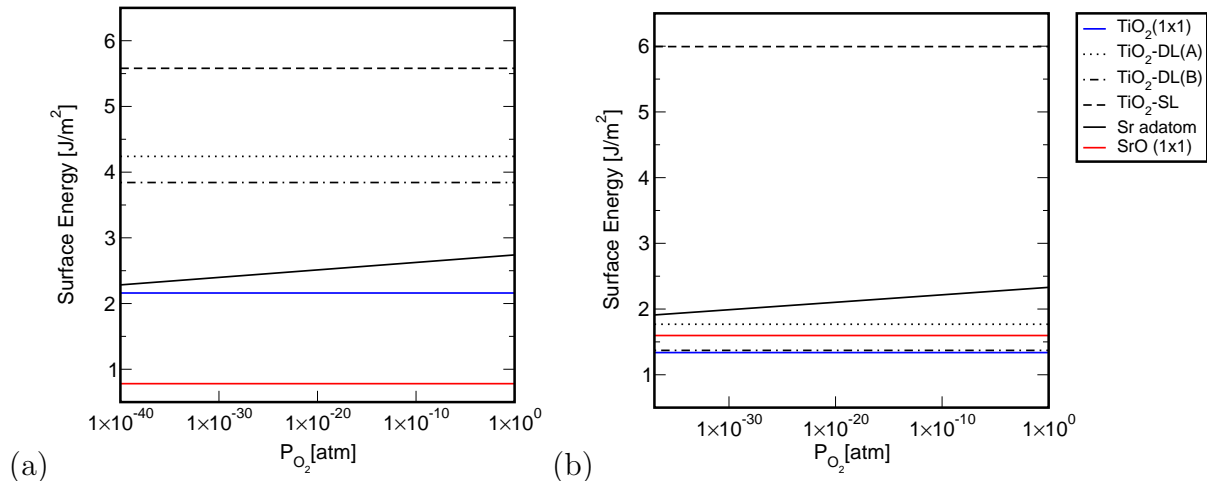


Figure 5.15: Surfaces energies for all the proposed atomic scale models of the $c(4 \times 2)$ surface reconstructions. Surface energies are expressed as functions of p_{O_2} at $T = 1000 \text{ K}$. In (a) the reconstructions are in equilibrium with SrO and in (b) with TiO₂. The labelling is as follows: TiO₂-DL(A) → Figure (5.12a), TiO₂-DL(B) → Figure (5.12b), TiO₂-SL → Figure (5.12c), Sr adatom → Figure (5.12d).

structed surface the one with the lowest surface energy for all the allowed values of p_{O_2} at $T = 1000 \text{ K}$. Only the surface energy of the Sr adatom model depends on p_{O_2} , and for no values of the environmental parameters p_{O_2} and $\mu_{\text{TiO}_2}^{\text{slab}}$ this surface becomes more stable than the unreconstructed (1×1) surfaces. In fact, in equilibrium with TiO₂, the Sr adatom model is not even more stable than any of the proposed double layer models for the $c(4 \times 2)$ surface reconstruction.

As regards the $c(4 \times 2)$ model proposed by Castell [11] (labelled as TiO₂-SL), it turned out to be very unstable. Its surface energy is independent of p_{O_2} and T and, for all the allowed values of $\mu_{\text{TiO}_2}^{\text{slab}}$, is the highest among the $c(4 \times 2)$ proposed models.

Finally, we have the double layer models. In equilibrium with TiO₂, the reconstruction labelled as TiO₂-DL(B) is as stable as the (1×1) TiO₂ terminated surface. All the surface energies in Figures (5.14) and (5.15) were calculated considering the vibrational contri-

bution as negligible. Thus, if we recall Figure (5.8), the vibrational contribution to the surface energy for the $\text{TiO}_2\text{-DL(B)}$ at $T = 1000\text{ K}$ is approximately $-0.15 \frac{\text{J}}{\text{m}^2}$. This contribution lowers the $\text{TiO}_2\text{-DL(B)}$'s surface energy to the point it becomes more stable than the (1×1) TiO_2 -terminated surface.

Chapter 6

STM images

6.1 Theory of Tunnelling Microscopy.

A result of the quantum mechanical tunnelling between the microscope's tip and the studied sample is the inherent resolution of the STM. The tunnelling current depends on the tunnelling barrier as well as on the electronic structure of the tip and surface [88, 89]. Following the model proposed by Tersoff and Hamman [89], in the STM images simulated on this work, the contributions from the tip's electronic structure have been ignored.

6.1.1 Tunnelling physics

Figure (6.1a) shows an idealised potential energy diagram for the electrons in a metal sample and tip a distance s apart. The respective work functions are ϕ_s and ϕ_t . In this example it is assumed that a positive bias voltage V is applied to the sample. The potential barrier, which the tip electrons have to tunnel through in order to have a current between the tip and the sample, is mainly due to the work functions of tip and sample [88, 89]. This is because the work function is what prevents electrons at the surface and tip to move from the Fermi level (E_f) into the vacuum [88]. To simplify the mathematical treatment without losing conceptual clarity, the potential energy barrier is treated as a trapezoid, whose height is approximated by the average work function of tip and sample. Within this model, the probability for an electron on the tip at energy E with respect to E_f to tunnel to the surface can be written as

$$T \approx \exp \left[-2s \left[\frac{2m}{\hbar^2} \left(\bar{\phi} - E - \frac{eV}{2} \right) \right]^{1/2} \right] \quad (6.1)$$

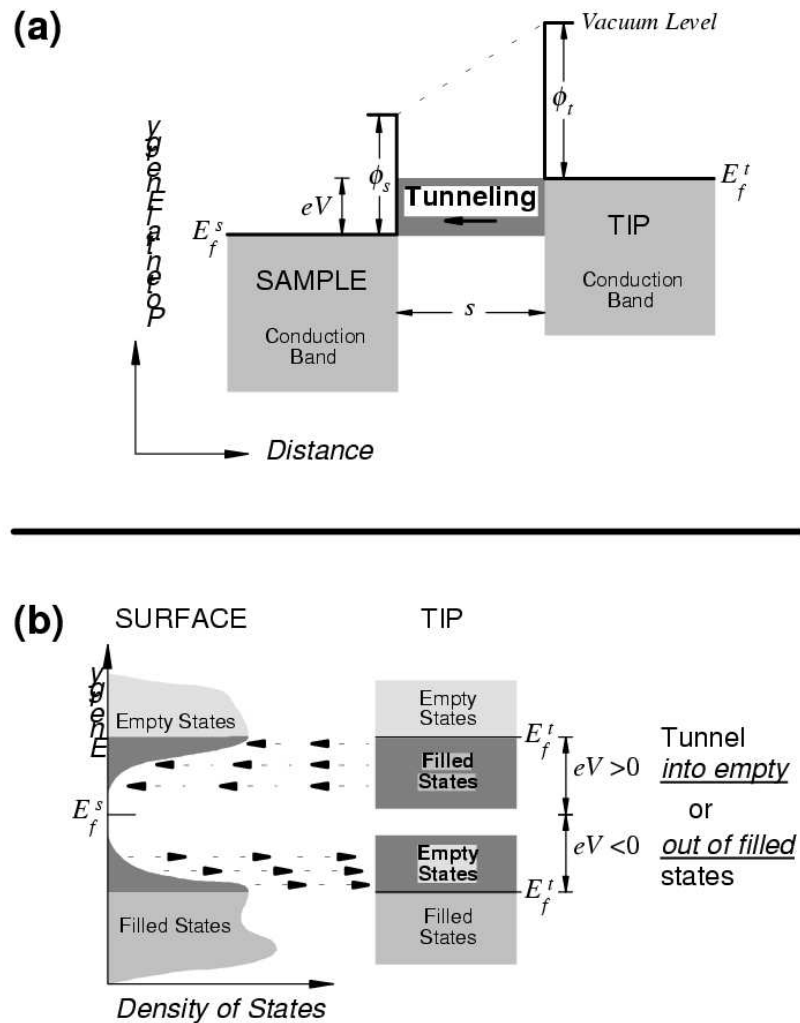


Figure 6.1: (a) Schematic of quantum-mechanical tunnelling between a metal tip and a metal surface a distance s apart. The tunnelling barrier is determined by the work functions of the surface and tip, ϕ_s and ϕ_t , respectively, and the bias voltage applied between the two, V . For the case shown, surface positive with respect to the tip, electrons tunnel from bands below the Fermi level of the tip to those above the Fermi level of the surface. (b) Detailed schematic of the role of the density of states near E_f on the tunnelling process both into and out of empty and filled states, respectively, on a semiconductor surface. This figure was extracted from L. J. Whitman [88].

where $\bar{\phi}$ is the average work function of the tip and sample, m is the electron mass and e is the electron charge.

6.1.2 Density of states (DOS) effects

In Figure (6.1b) it is shown how the net tunnelling current depends on the number of sample and tip surface electronic states that overlap in an energy range determined by the applied bias voltage. If the applied bias voltage is positive (as for the samples studied here), electrons in occupied states on the tip can tunnel into the energy equivalent empty states in the conduction band on the sample. If a negative sample bias is applied, electrons in the filled states on the surface tunnel into empty states on the tip. The probability for each of these tunnelling events is given by Equation (6.1) [88].

For an energy window of eV , the net tunnelling current, at a point r , can be approximated as

$$I(\mathbf{r}) \propto \int_E^{E+eV} \rho_t(E, \mathbf{r}) \rho_s(eV + E, \mathbf{r}) T(E, eV) dE \quad (6.2)$$

where ρ_s and ρ_t are the energy and position-dependent local density of states¹ for the sample and tip, respectively. In a metallic surface E is the Fermi energy, while for a semiconductor surface E is the energy of the conduction band edge [36, 88].

¹A general expression for the total density of states is as a sum of delta functions

$$g(\varepsilon) = \sum_{\varepsilon_i} \delta(\varepsilon - \varepsilon_i) \quad (6.3)$$

The local density of states, associated with a particular position in space, can be obtained by *projecting* the contributions to the total density of states on the particular position in space. This is achieved by weighting each contribution, at ε_i , by a coefficient, $dP_i(r)$, that is the *probability of finding an electron*, with energy ε_i , in a volume element d^3r situated at the point r . If $\psi_i(r)$ is the eigenstate associated with energy ε_i , $|\psi_i(r)|^2$ is then interpreted as the *probability density*, with

$$dP_i(r) = C |\psi_i(r)|^2 d^3r \quad (6.4)$$

where C is a normalisation constant. We then have

$$\rho(\varepsilon, r) = \sum_{\varepsilon_i} dP_i(r) \delta(\varepsilon - \varepsilon_i) \quad (6.5)$$

as the final expression for the local density of states.

6.1.3 Imaging mode

Constant current imaging is the main operational mode of STM. In that mode, the height of the tip is recorded as it is moved over the surface while the tunnelling current is kept constant. When electrons tunnel from the sample's surface to the tip, the so called *filled-state* topographic image is obtained; tunnelling from tip to sample results in an *empty-state* image. For the case of a perfectly crystalline surface, the electronic corrugation of the topography from peak-to-valley height ranges from 0.001 to 0.01 nm on metals and 0.01 to 0.1 nm on semiconductors [36, 88]. For the case when the density of states is regular enough across the sample's surface and modulated only by the location of surface irregularities (like adatoms, steps, etc), the electronic topography will represent a simple contour line of constant height of the tip above these surface irregularities. However, usually $\rho_s(E, r)$ varies across the surface, and at some energies may not even be a maximum over the aforementioned irregularities. In such cases the images may look different at different bias voltages (we may have a shift in the positions of the topographic maxima), making interpretation difficult. This leads to a central principle in STM: *constant current topography measures the surface of constant integrated density of states. This surface generally depends on the bias voltage and may not be correlated with the positions of the surface atoms* [88].

6.2 STM images of the Sr adatom model.

The calculated density of states of bulk SrTiO₃, clean (1 × 1) TiO₂-terminated and the Sr adatom surface reconstructions involved in the studied surface phase transitions are shown in Figure (6.2). If we compare the DOS of bulk SrTiO₃ with the DOS of clean (1 × 1) TiO₂-terminated surface, we can see the localised surface states on the (1 × 1) TiO₂ terminated that appeared in the band gap region of bulk SrTiO₃. Regarding the Sr adatom reconstructions we note that the conduction bands were lowered and the surface became metallic. This is because Sr adatom donated its outermost 5s electrons to the surface, partially filling the conduction band of the clean TiO₂ terminated (1 × 1) surface.

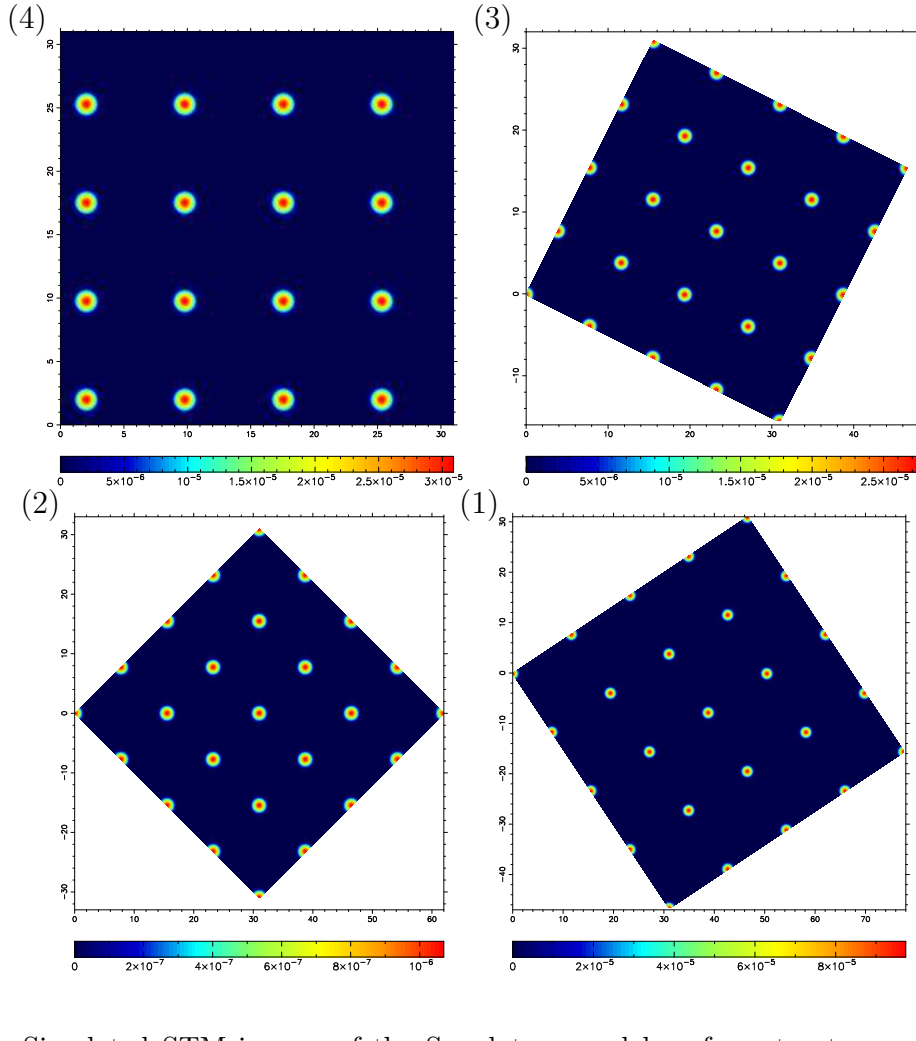


Figure 6.2: Simulated STM images of the Sr adatom model surface structures. Surfaces are denoted as follows: (1) $(\sqrt{13} \times \sqrt{13}) \theta = 0.0769$ (2) $c(4 \times 4) \theta = 0.125$ (3) $(\sqrt{5} \times \sqrt{5}) \theta = 0.20$ (4) $(2 \times 2) \theta = 0.25$. Scales in the x and y axis are in \AA . These plots shows the local density of electronic states in the horizontal plane 4\AA above the surface. In rough correspondence with the experimental bias conditions, we summed the density of conduction band states from E to $(E + eV)$ eV above the Fermi level. The colour scale indicates $\frac{\text{(number of electronic states)}}{(\text{\AA})^3}$.

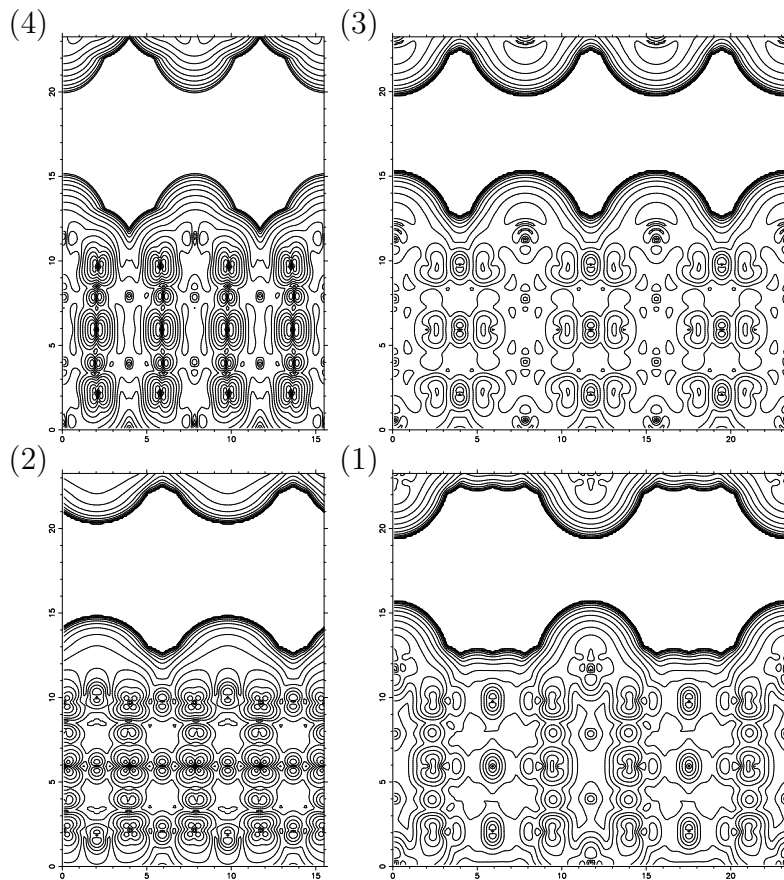


Figure 6.3: Contour plots of the spatially resolved density of electronic states of the Sr adatom model surface structures. Scales in the axis are in Å. The density of states was integrated in an energy window that corresponded to the experimental bias voltage. The value of the LDOS for the contour level at the surface is $1 \times 10^{-8} \frac{\text{(number of electronic states)}}{(\text{Å})^3}$ in correspondence with the experimental tunnelling current[90]. Surfaces are denoted as follows: (1) $(\sqrt{13} \times \sqrt{13}) \theta = 0.0769$ (2) $c(4 \times 4) \theta = 0.125$ (3) $(\sqrt{5} \times \sqrt{5}) \theta = 0.20$ (4) $(2 \times 2) \theta = 0.25$.

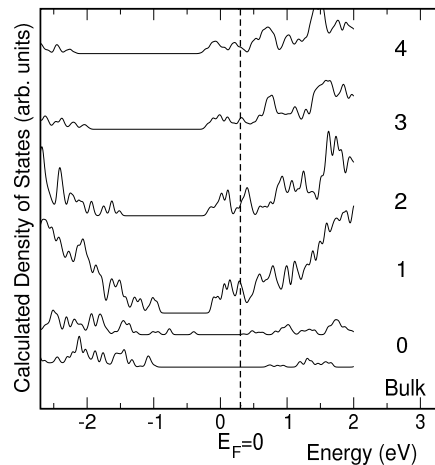


Figure 6.4: Calculated density of states for bulk SrTiO_3 and the Sr adatom surface reconstructions involved in the phase transition. All the density of states are divided by the number of atoms in each supercell. As before, the surfaces are denoted as follows: (0) $(1 \times 1)\text{TiO}_2$ -terminated (1) $(\sqrt{13} \times \sqrt{13}) \theta = 0.0769$ (2) $c(4 \times 4) \theta = 0.125$ (3) $(\sqrt{5} \times \sqrt{5}) \theta = 0.20$ (4) $(2 \times 2) \theta = 0.25$. The vertical dashed line indicates the Fermi level, which is set at the zero of energy. All the surface reconstructions are metallic ones.

If we recall expression (6.2) for the tunnelling current in Section (6.1.2)

$$I(\mathbf{r}) \propto \int_E^{E+eV} \rho_t(E, \mathbf{r}) \rho_s(eV + E, \mathbf{r}) T(E, eV) dE \quad (6.6)$$

we see that it depends on the the tip and sample density of states, ρ_t and ρ_s , the applied voltage bias V , and the tunnelling probability T . Tersoff and Hamann [89] approximated the tip as a piece of Sommerfeld metal with a finite radius of R . In our approximation, we have considered the tip as an ideal mathematical point. Within this framework, the tunnelling current, under conditions of positive bias voltage, is proportional to the density of sample states within the energy gap ranging from E to $(E + eV)$

$$I(\mathbf{r}) \propto n(\mathbf{r}) = \int_E^{E+eV} \rho_s(E, \mathbf{r}) dE \quad (6.7)$$

In principle, the calculation of the tunnelling current can be made more accurate if the tip electronic structure is explicitly included. However, Equation (6.7) captures all the first-order contributions to the tunnelling current with a minimum amount of computation. With these assumptions, for any surface the spatially resolved integral of the electronic density of states energetically relevant to tunnelling is a first order approximation of a

STM image of that surface.

For our simulations of the STM images in the Sr adatom models, the spatially resolved density of states of the samples was integrated over the energy window relevant for tunnelling. Table (6.1) shows the experimental bias voltages and tunnelling currents for the surface reconstructions observed by Kubo and Nozoye [12]. The energy window is usually assumed

Surface reconstruction	Bias [V]	Tunnelling current [nA]
c(4×4)	0.5	0.05
(2×2)	0.7	0.03
($\sqrt{5} \times \sqrt{5}$)	0.7	0.01
c(4×4)	0.5	0.05
($\sqrt{13} \times \sqrt{13}$)	0.5	0.01

Table 6.1: Experimental tunnelling currents and bias voltages for the Sr adatom surface reconstructions. These are the reconstructions involved in the phase transitions depicted in Figure (5.2).

to correspond to the sample bias [91, 92] and sometimes is even smaller than the sample bias [93]. The bias voltage used by Kubo and Nozoye [12] varied from 0.5V to 0.7V and, for each surface reconstruction, we choose an energy window that corresponds to its bias voltage. Although these values for the energy window are always approximate, because band energies from density functional theory differ from physical excitation energies, the use of the aforementioned values for the energy window has led to successful STM image simulations for a large number of different surfaces [36, 94].

Figure (6.2) shows top-views of $n(\mathbf{r})$. The vector r is in a plane parallel to the surface, for a tip-sample distance of approximately 4 Å above the topmost atom on the relaxed surface structure. Although the tip-sample distance involved in UHV-STM experiments could be longer (between 4-6 Å), the $n(\mathbf{r})$ plots calculated for larger values of the tip-sample distance are unreliable because the values of $n(\mathbf{r})$ are very small at large tip-sample distances. The use of the aforementioned tip-sample distances has been found to provide partial density plots consistent with UHV STM images recorded for a number of surfaces [93, 95, 96]. To complement the top views, we have also plotted contour plots of the spatially resolved density of states for slices that start at the surface of the slab, passing through the Sr adatoms and cutting down to the bottom surface of the slab. These lateral views are showed in

Figure (6.3). The most relevant contour plots are the ones at the surface, because the electrons from the tip will tunnel there.

Contour levels are plotted within a density of states range that depends on the surface reconstructions. The separation between consecutive contour levels within this range can be understood through the following expression

$$[n_{\max}(\mathbf{r})]^{(\alpha \text{ ncont})} = n(\mathbf{r})_{\text{ncont}} \quad (6.8)$$

Equation (6.8) gives the local density of states (LDOS) at each contour level. n_{cont} labels the contour levels and we plot 15 of them in the density of states range. $n_{\max}(\mathbf{r})$ happens at $n_{\text{cont}} = 1$ and $n_{\min}(\mathbf{r})$ happens at $n_{\text{cont}} = 15$. Equation (6.8) indicates a power law decay in the density of electronic states as n_{cont} increases. This power law decay starts from $n_{\max}(\mathbf{r})$, which is the maximum density of states in the slice we are studying. The value of α is given by

$$\alpha = \frac{\log(n_{\min}(\mathbf{r}))}{n_{\text{cont}_{\max}} \log(n_{\max}(\mathbf{r}))} \quad (6.9)$$

$n_{\min}(\mathbf{r})$ in Equation (6.9) is the value of the minimum density of states that we plotted, which happens in the outmost contour level, where ($n_{\text{cont}} = 15$). According to Tersoff and Hamman's model [89] (which uses Bardeen's application of perturbation theory to the tunnelling problem [90]), the tunnelling current at this outmost contour level can be written as

$$I(\mathbf{r}) = \frac{2\pi e^2}{\hbar} V n_{\min}(\mathbf{r}) \quad (6.10)$$

The value of $n_{\min}(\mathbf{r})$ in Equation (6.10) is chosen such that $I(\mathbf{r})$ gives an approximation of the experimentally observed tunnelling current for the particular surface reconstruction which STM image we are simulating. Thus, α is obtained by means of Equation (6.9), where $n_{\max}(\mathbf{r})$ is the maximum local density of states in the slice we are studying, $n_{\text{cont}_{\max}} = 15$ and $n_{\min}(\mathbf{r})$ is calculated using Equation (6.10).

The experimentally observed currents for the Kubo and Nozoye model are shown in Table (6.1), and were in the range of 0.01 nA to 0.05 nA . These currents correspond to a density of states of the order of $n_{\min}(\mathbf{r}) = 1 \times 10^{-8}$, and that is the uppermost density of states isoline we have plotted.

Under constant current tunnelling conditions, the STM tip is expected to follow one of the equal-density contours a couple of angstroms above the surface. Figure (6.3) clearly shows that the contours of constant density of states extend higher above the Sr adatoms. Therefore, the expected geometric corrugation at the surface (due to Sr adatoms) is not changed by electronic structure effects. We can then conclude that Sr adatoms are imaged as bright spots, which is in agreement with the STM observation performed by Kubo and Nozoye [12].

6.3 STM images for the (2×1) and $c(4\times 2)$ surface reconstructions

6.3.1 The (2×1) reconstruction

Figure (6.5) is a high resolution STM image of the (2×1) reconstructed surface obtained

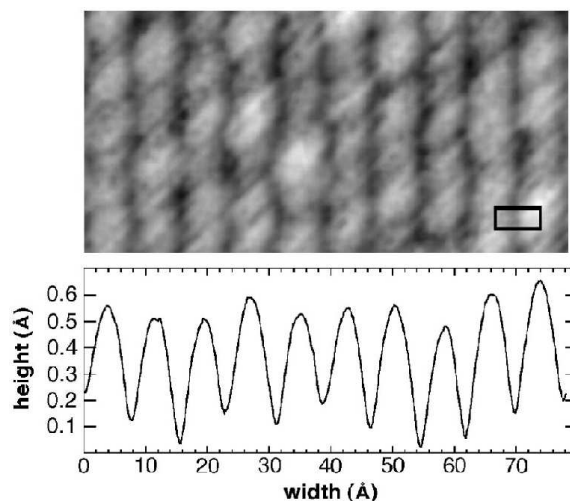


Figure 6.5: STM image (2 V bias voltage, 0.5 nA tunnelling current) of the (2×1) reconstructed surface [36]. By averaging vertically through the image a plot of the average row heights is created as shown in the lower panel. The typical corrugation height is between 0.4 and 0.5 Å.

by Castell [36]. In the picture we can clearly see bright lines separated by around 0.8 nm, which is equivalent to two unit cells. Moreover, these bright rows are wider than the gaps between them. LEED patterns revealed a single unit cell periodicity along the rows [11], but this cannot be discerned in the STM images. The typical corrugation height perpendicular to the rows is 0.05 nm.

Figure (6.6) shows the calculated density of states for all the proposed models for the (2×1) surface reconstruction. The labelling of these reconstructions is as explained in Section (5.2.3). Of these proposed models, only the ones labelled as Ti_2O_3 -SL -proposed by Castell [11]- and Sr adatom -proposed by Kubo and Nozoye [12]- are metallic ones. In Section (6.2), it is explained why the Sr adatom models are metallic. As regards the Ti_2O_3 -SL reconstruction, we conclude it is metallic due to the oxygen vacancies in its initially TiO_2 - (1×1) terminated surface. One vacant oxygen site can produce two electrons which will occupy the Ti 3d states near the conduction band bottom, transforming the surface into a metallic one.

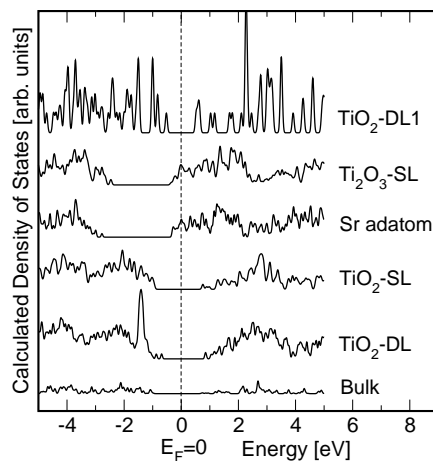


Figure 6.6: Calculated density of states for the (2×1) surface reconstructions

Constant current imaging is used to observe the (2×1) surface reconstructions, with electrons tunnelling from the tip to the sample. Again, we consider the tip as an ideal mathematical point and use Equation (6.7) to express the tunnelling current. Table (6.2) expresses the experimental tunnelling currents and bias voltages for the surface reconstructions observed with STM.

The reconstructions proposed by Erdman [15, 16] and Kubo and Nozoye [12] were not observed by STM. In order to simulate their STM images, we adopted an energy window that correspond to the bias voltage used for the TiO_2 -SL reconstruction. The tunnelling current is also assumed to be as the one observed in the TiO_2 -SL reconstruction.

We use Equation (6.7) to calculate the spatially resolved density of states $n(\mathbf{r})$. As before, we integrate the empty electronic states over an energy window going from E to $E + eV$,

Surface reconstruction	Bias [V]	Tunnelling current [nA]
Ti ₂ O ₃ -SL[11]	2.3	0.1
TiO ₂ -SL[11]	2.3	0.1
TiO ₂ -DL[15]	Not observed by STM	Not observed by STM
Sr adatom[12]	Not observed by STM	Not observed by STM
TiO ₂ -DL1[16]	Not observed by STM	Not observed by STM

Table 6.2: Experimental tunnelling currents and bias voltages for the (2×1) surface reconstructions. The reconstructions proposed by Erdman[15, 16] and Kubo and Nozoye[12] were not observed by STM.

eV being related with the experimental bias voltage. For the metallic surfaces E is the Fermi energy, while in all the other cases is the conduction band edge.

TiO₂-DL reconstruction

Figure (6.7) shows the top and lateral views for the TiO₂-DL reconstruction. Figure (6.7a) shows a top view of $n(\mathbf{r})$ in a plane parallel to the surface that is 2Å above the topmost atom on the relaxed surface structure. The atom that had the outmost relaxation in this surface reconstruction is an oxygen labelled as O4 in Figure (5.7b). In order to have a tunnelling current of 0.1 nA , we need a density of states of the order of $\approx 10^{-7}$. The observed rows of bright spots are sites where the density of states is highly corrugated and, therefore, they would be easier to image in an STM. Figure (6.7c) shows the density of states for a slice passing through the aforementioned topmost oxygen.

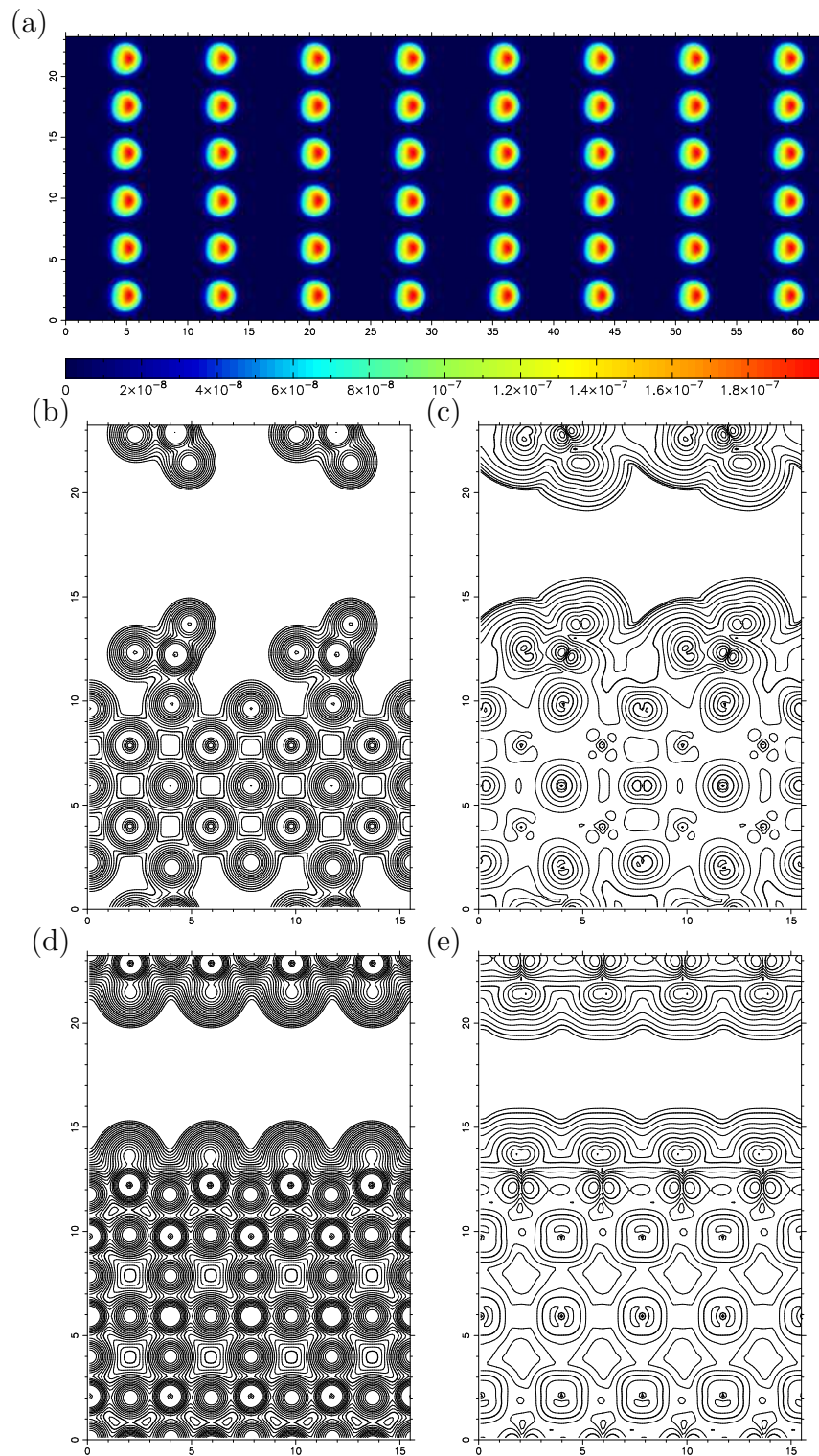


Figure 6.7: Contour plots of the spatially resolved density of states and electronic density in the model proposed by Erdman *et al* [15] for the (2×1) surface reconstruction. Scales in the axis are in \AA . The density of states was integrated in an energy window of 2.3 eV above the conduction band edge. Figure (a) shows a top view of $n(\mathbf{r})$ in a plane parallel to the surface that is 2 \AA above the topmost atom on the relaxed surface structure. Figures (b) and (c) show the electronic density and the density of states for a slice running along the length of the rectangular unit cell showed in Figure (5.9b). Figures (d) and (e) show the same, but for a slice running along the width of the aforementioned rectangle.

This slice runs along the length of the rectangular unit cell showed in Figure (5.9b). Figure (6.7b) shows the electronic density on the same slice. The maximum electronic density depicted in this figure is $\approx 10^{-2}$. The purpose of this picture is to complement Figure (6.7c) in showing the positions of the surface atoms in the slab, and compare the density of states corrugation at the surface with the geometric one. On the surface of Figure (6.7b), the topmost atoms are oxygens, and they appear as small white circles with a dot in the centre. Below the topmost oxygens, a bit off-centre towards the left, there are the titaniums, which appear as a slightly larger white circle with a dot in the centre as well. To the left of the Ti there are surface oxygens labelled as O1 in Figure (5.7b). Finally, in the bulk of the slab we have a SrO plane, where strontiums are the large circles and oxygens the smaller ones. Figures (6.7d) and (6.7e) show the electronic densities and the densities of states for a slice perpendicular to the previous one. This slice runs along the width of the rectangular surface unit cell of Figure (5.7b), through a plane that is midway between the bulk TiO_2 plane and the topmost oxygens O4. On Figure (6.7d), we can see the surface oxygens atoms O4 as small white open ovals. Below the surface oxygens are the Ti, represented by a white circle with a black dot in the centre. In between these Ti, there are the oxygens labelled as O2 in Figure (5.7b). Further down inside the bulk we can see the TiO_2 plane.

The density of states corrugation in Figure (6.7c), along the length of the rectangular unit cell, is significantly larger than in Figure (6.7e), along the width of the rectangular unit cell. This indicates that it would be easier to image the corrugation along the length of the rectangular unit cell, obtaining the bright rows of Figure (6.5). Except for the fact that it would be difficult to obtain STM resolution along the rectangular unit cell's width, the STM topography is not too different from the physical one.

TiO_2 -SL reconstruction

Figure (6.8) follows the same scheme as Figure (6.7). Figure (6.8a) shows a top view of $n(\mathbf{r})$ in a plane parallel to the surface that is 3\AA above the topmost atom on the relaxed surface structure, which is oxygen O1 in Figure (5.7a). The values for the density of states observed in the top view are related with the tunnelling current as explained for Figure (6.7a). Figures (6.8b) and (6.8c) show the electronic density and the density of states for a slice that runs along the length of the rectangular unit cell in Figure (5.7a).

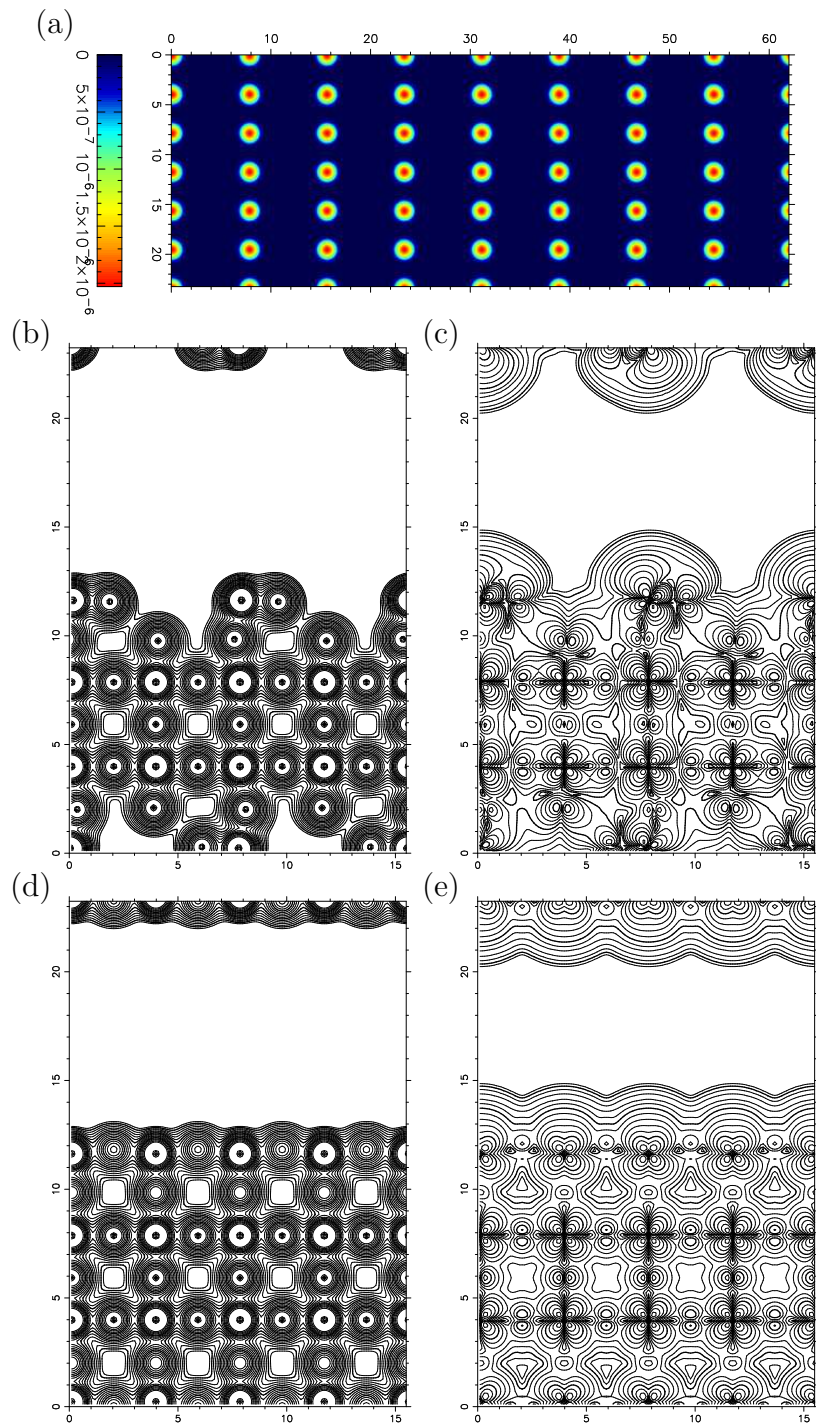


Figure 6.8: Contour plots of the spatially resolved density of states and electronic density in the model proposed by me for the (2×1) surface reconstruction. Scales in the axis are in \AA . The density of states was integrated in an energy window to 2.3 eV above the conduction band edge. Figure (a) shows a top view of $n(\mathbf{r})$ in a plane parallel to the surface that is 2\AA above the topmost atom on the relaxed surface structure. Figures (b) and (c) show the electronic density and the density of states for a slice running along the length of the rectangular unit cell showed in Figure (5.9a). Figures (d) and (e) show the same, but for a slice running along the width of the aforementioned rectangle.

This slice passes through a TiO_2 plane in the bulk. The large white circles on the surface layer are titanium atoms, to their right there are oxygens O1. Below the surface titaniums there are oxygens, and further down in the bulk we can see the titanium and oxygens of the TiO_2 bulk plane.

Figures (6.8d) and (6.8e) show the electronic density and the density of states for a slice that runs parallel to the width of the rectangular unit cell in Figure (5.7a). Oxygens labelled as O2 in Figure (5.9a) are slightly off that slice, but we can see them in Figure (6.8d). Oxygens O2 are the small white circles at the surface layer, in between two medium white circles with a black spot in the centre representing the Ti atoms. Below this first layer we can see the bulk TiO_2 plane, where Ti are described as before, but oxygens are smaller white circles with a black spot in the centre.

As for the model proposed by Erdman *et al* [15], the density of states' corrugation along the length of the rectangular unit cell is significantly larger than along the width. Therefore, the STM image for this model would also be given by a set of wide bright rows separated by 0.8 nm . The density of states' corrugation is higher over the titaniums and oxygens at the surface, indicating that the vertical rows, composed of titanium and oxygens, in Figure (5.7a) would be imaged by the STM.

Ti_2O_3 reconstruction

The top view in Figure (6.9a) shows $n(\mathbf{r})$ in a plane 3Å above the topmost atom in the surface. We can see rows of bright large spots separated by 0.8 nm , with smaller spots in-between these rows. Figures (6.9b) and (6.9c) show the electronic density and the density of states for a slice that runs along the length of the rectangular unit cell in Figure (5.9c). This slice passes through a TiO_2 plane in the bulk. The large white circles with the black spot on the centre on the surface layer are titanium atoms, in-between there are the oxygens. We can clearly see the missing oxygen rows. Figures (6.9b) and (6.9c) are the electronic density and the density of states in a direction parallel to the width of the rectangular surface unit cell in Figure (5.9c). Further down in the bulk we can see the titanium and oxygens of the TiO_2 bulk plane. The corrugation in the two perpendicular directions in the surface unit cell is similar and is large enough to be imaged. However, in Figure (5.9c), we see that corrugation is slightly higher above the titanium atoms and this is reflected in the top view of Figure (6.9a), where the brightest spots are above the titanium atoms.

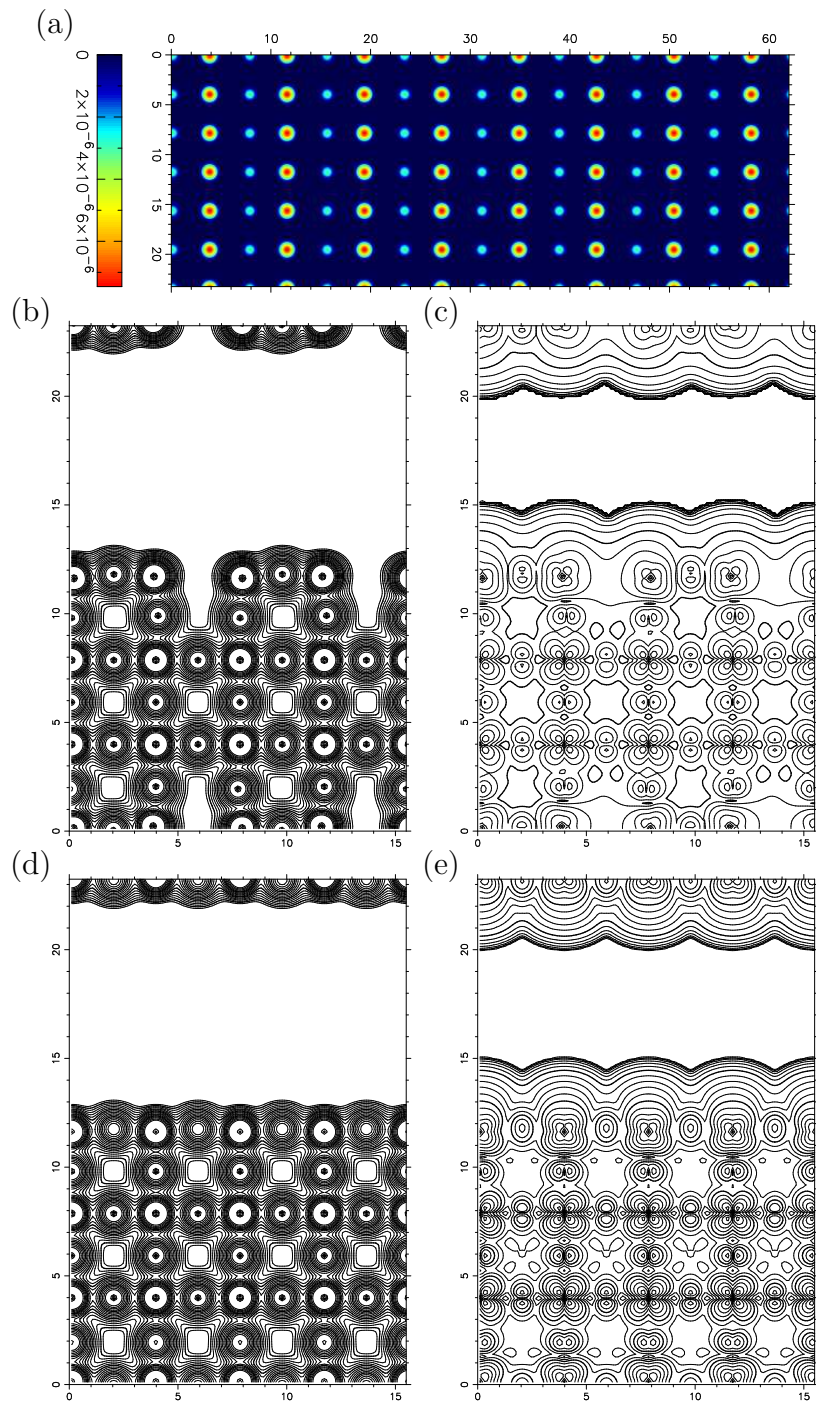


Figure 6.9: Contour plots of the spatially resolved density of states and electronic density in the model proposed by Castell [11] for the (2×1) surface reconstruction. Scales in the axis are in Å. The density of states was integrated in an energy window to 2.3 eV above the Fermi energy. (a) a top view of $n(\mathbf{r})$ in a plane parallel to the surface that is 3 Å above the topmost atom on the relaxed surface structure. (b)-(c) the electronic density and the density of states for a slice running along the length of the rectangular unit cell showed in Figure (5.9a), (d) (e) the same but for a slice running along the width of the aforementioned rectangle.

Therefore, the STM image we would obtain could be one of bright rows, just like the experimental one.

Sr adatom reconstruction

The set of Figures (6.11) are related with the Sr adatom model. The top view is for a plane 4\AA above the Sr adatoms at the surface. The lateral views are as explained for the previous models, but in relation with Figure (5.9b). The density of states' corrugation in Figure (6.11c), along the length of the rectangular unit cell, is significantly larger than in Figure (6.11e), along the width of the rectangular unit cell. Therefore, it would be easier to image the corrugation along the length of the rectangular unit cell, obtaining the bright rows of Figure (6.5). There is no distortion of the physical topography due to electronic structure effects and the simulated STM images agree very well with the experimental ones.

TiO₂-DL1 reconstruction

Finally, Figure (6.13) shows the simulated STM images for the $(\sqrt{2} \times \sqrt{2}R45^\circ)$ -label as TiO₂-DL1- model for the (2×1) surface reconstruction. From Figure (6.10) we know that this reconstruction has not a (2×1) periodicity. Figure (6.13a) is a top view of $n(\mathbf{r})$ in a plane 2\AA above the outermost relaxed atom in the surface. The rectangular window showing this top view is oriented as the square unit cell depicted in Figure (5.11), with its width parallel to the titanium rows. Figures (6.13b) and (6.13c) show the electronic density and the density of states for one slice that runs along the dotted line in Figure (6.10). This line passes through oxygen O1 and is parallel to the titanium rows.

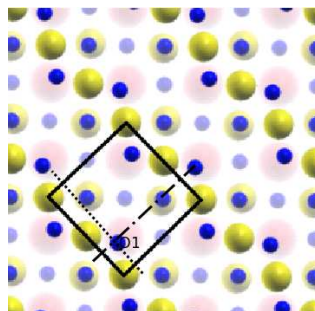


Figure 6.10: Top view of the $(\sqrt{2} \times \sqrt{2}R45^\circ)$ surface reconstruction.

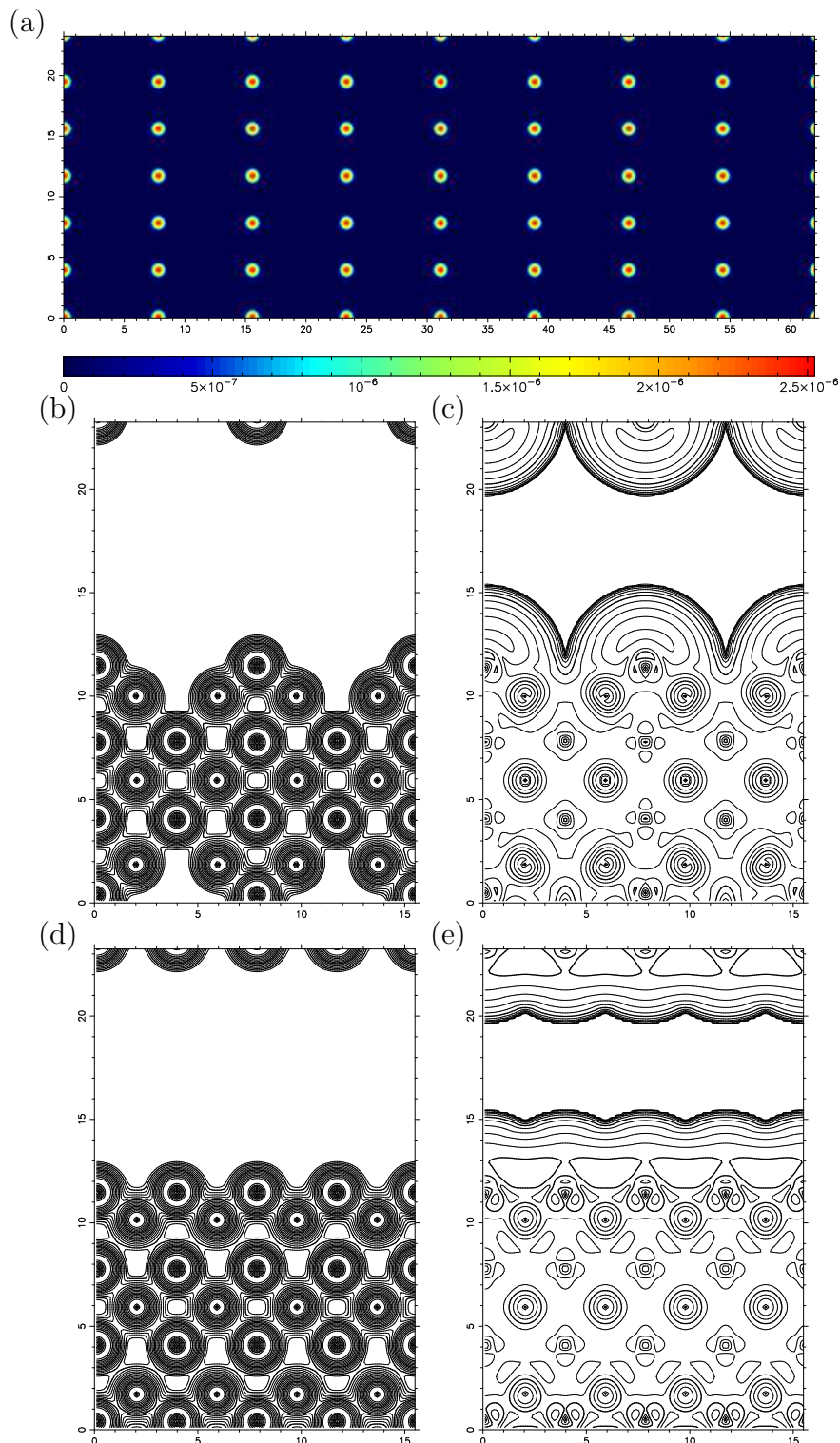


Figure 6.11: Contour plots of the spatially resolved density of electronic states of the Sr adatom model for the (2×1) surface reconstruction. Scales in the axis are in Å. The density of states was integrated in an energy window to 2.3 eV above the Fermi level. (a) a top view of $n(\mathbf{r})$ in a plane parallel to the surface that is 4 \AA above the topmost atom on the relaxed surface structure. (b)-(c) the electronic density and the density of states for a slice running along the length of the rectangular unit cell shown in Figure (5.9b), (d)-(e) the same, but for a slice running along the width of the aforementioned rectangle.

O1 is the topmost relaxed atom in the reconstruction and we found that the density of states corrugation, along this dotted line, is higher over these atoms.

Figures (6.13d) and (6.13e) are the electronic density and the density of states for the slice that runs along the dash-dotted line. Like in the dotted line, the high corrugation occurs over the oxygens O1. The corrugation height is higher along the dash-dotted line than along the dotted line. This suggests that it is easier to obtain atomic resolution STM images along the dash-dotted line. Therefore, the STM image would be one of bright rows running in the direction of the dotted line. The width of the rectangles in Figures (6.12a)

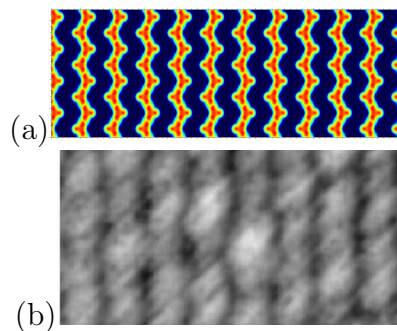


Figure 6.12: (a) Top view of the simulated STM image for the TiO_2 -DL1 model of the (2×1) reconstruction. (b) a closer view of the experimentally observed STM image of the (2×1) reconstruction.

and (6.12b) is 60\AA . These Figures allow a close comparison between the (2×1) 's experimental STM image and its simulation. In experiment, the STM tip's height z is varied so as to keep the tunnelling current constant and the variation in z is displayed as the STM image. The image brightness is proportional to the z protrusions of this iso-surface. Figure (6.12a) shows the density of states $n(\mathbf{r})$ in a plane 2\AA above the oxygens O1. In Figure (6.13e), this plane would be placed as a horizontal line at 15\AA , cutting through the iso-surfaces of constant density of states. Therefore, the brightness in this top view is related with the corrugation of the iso-surface. Thus, the vertical zigzag lines on Figure (6.12a) indicate the region on the surface with the highest corrugation. Corrugation in the lateral view of Figure (6.13e) indicates that the bright rows are likely to be wider than the gaps between the rows, just as it is observed in Figure (6.12b). Besides, on close scrutiny of Figure (6.12b) we can see that the rows have the zigzag shape observed on Figure (6.12a).

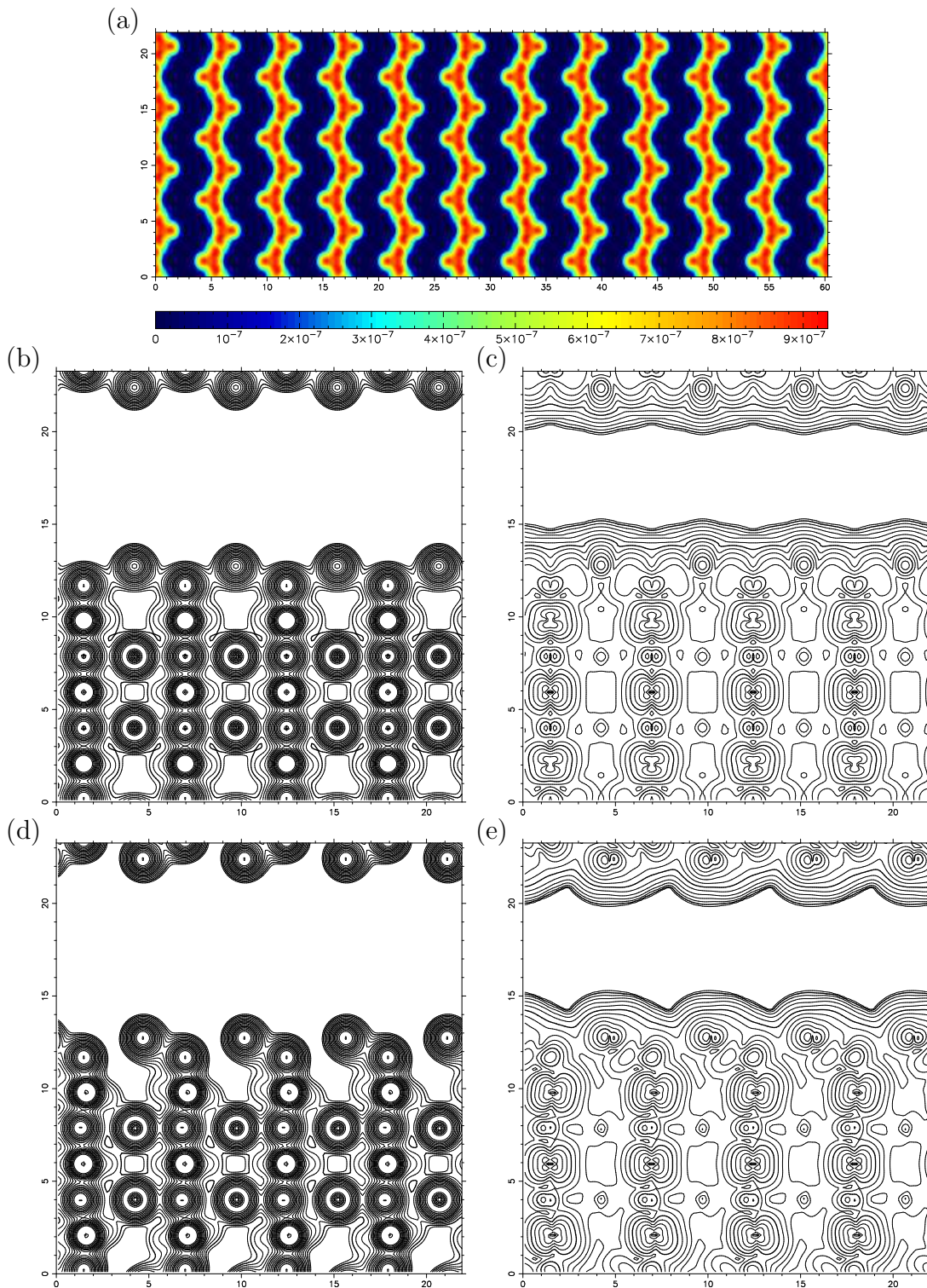


Figure 6.13: Contour plots of the spatially resolved density of electronic states of the TiO_2 -DL1 model for the (2×1) surface reconstruction. The density of states was integrated in an energy window to 2.3 eV above the conduction band edge. Scales in the axis are in Å. (a) a top view of $n(\mathbf{r})$ in a plane parallel to the surface that is 2 \AA above oxygens O1. (b)-(c) the electronic density and the density of states for a slice running along the dotted line shown in Figure (6.10). (d)-(e) the same, but for a slice running along the dash-dotted line in Figure (6.10)

6.4 The $c(4\times 2)$ reconstruction

Figure (6.14) is a STM image of the $c(4\times 2)$ surface reconstruction obtained by Castell [11]. The slow scan direction in Figure (6.14a) is from the top to the bottom of the image. Half-way through taking the image (indicated by the black arrows), and without changing any imaging conditions, the tip is changed and the atomic contrast changes, changing the corresponding STM image. In the top part of Figure (6.14a) there is one spot per $c(4\times 2)$ surface unit cell, while in the bottom part of Figure (6.14a) there are two spots per $c(4\times 2)$ surface unit cell.

A close up of a region from a different part of the sample taken under different imaging conditions with one spot per unit cell is shown in

Figure (6.14b) shows an amplified image of a different region of the sample, where a $c(4\times 2)$ surface unit cell with one spot per unit cell can be observed. The panel next to it, Figure (6.14c), shows an image with two spots per unit cell, while Figure (6.14d) shows an image where both types of unit cell are seen in the same image. Castell [11] stressed that whether one or two spots per unit cell are seen, it does not depend on imaging conditions like bias voltage or tunnelling current, but instead on the type of atom at the tip apex. He also suggested that the change in tip apex atom allows different surface sub-lattices to be observed. Thus, as the sample surface is assumed to be Ti and O terminated, Figure (6.14b) could be showing the Ti surface lattice and Figure (6.14c) the O lattice. His atomic scale model for the $c(4\times 2)$ surface reconstruction showed in Figure (5.12c) is based on this qualitative interpretation of the STM images.

The calculated density of states of bulk SrTiO_3 , relaxed TiO_2 (1×1) terminated surface and all the proposed models for the $c(4\times 2)$ surface reconstruction are shown in Figure (6.15). The labelling of the reconstructions is as explained in Section (5.2.3). Of the proposed models, only the Sr adatom structure is a metallic one. As for the (2×1) surface reconstructions, constant current imaging is used, with electrons tunnelling from the tip to the sample assuming the tip is an ideal mathematical point. Equation (6.7) is used to express the tunnelling current. Table (6.3) shows the experimental STM parameters for the observed reconstructions. Equation (6.7) is used to calculate the spatially resolved density of states. The adopted energy window, used for the integration in Equation (6.7), corresponds to the experimental bias. The lower integration limit in Equation (6.7) is the Fermi energy for the Sr adatom model, while for all the other models is the conduction band edge.

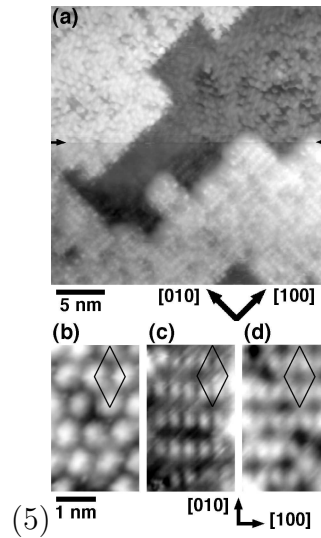
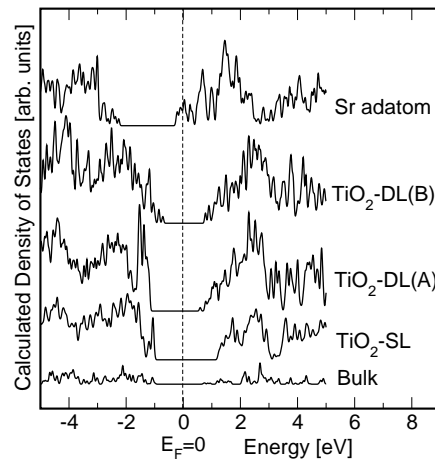


Figure 6.14: STM images of the $c(4 \times 2)$ reconstruction observed by Castell [11]. In (a) (0.87 V bias, 0.15 nA current) the top of the image contains one spot per $c(4 \times 2)$ unit cell similar to the image from another region shown in (b) (0.2 V bias, 0.1 nA current). After a tip change indicated by arrows half way through the image in (a) two spots per unit cell are seen. This is also observed in a different region as shown in (c) (0.25 V bias, 1 nA current). Sometimes a mixture of the two images in (b) and (c) is observed as shown in (d) (0.45 V bias, 0.44 nA current). The $c(4 \times 2)$ unit cells are indicated in (b-d). Note that the crystallographic directions in (a) are rotated by 45° relative to (b-d).

The $\text{TiO}_2\text{-DL(A)}$ reconstruction

Figure (6.17) shows a top view of $n(\mathbf{r})$, for the $\text{TiO}_2\text{-DL(A)}$ surface reconstruction, in a horizontal plane parallel to the surface that is 2.5 \AA above the topmost atom in the relaxed structure. This structure was not observed with a STM (a combination of HREM and theoretical crystallographic direct methods was used) and to simulate its image we adopted a 2 V energy window, which was one of the bias voltages used by Castell [11], and assumed a tunnelling current of 0.1 nA. The observed brightest spots are in places at the surface where the density of states corrugation changes sharply. Therefore, these regions are easier to image in an STM. These bright spots are related with the surface oxygens labelled as O1 in Figure (5.7c). Figure (6.16b) shows the density of states for a slice passing through these oxygen atoms, we can see that the apparent corrugation above these oxygens is about 0.5 \AA and changes sharply in that region. The topmost isoline in Figure (6.16b) represents a density of states of approximately 1×10^{-7} , which is, according to Equation (6.10), the required value for the tunnelling current to be 0.1 nA. This slice runs along one of the

Figure 6.15: Calculated density of states for the $c(4\times 2)$ surface reconstructions

Surface reconstruction	Bias [V]	Tunnelling current [nA]
TiO ₂ -SL[11]	2.0	0.1
TiO ₂ -DL(A)[16]	Not observed by STM	Not observed by STM
TiO ₂ -DL(B)[16]	Not observed by STM	Not observed by STM
Sr adatom[12]	0.7	0.03

Table 6.3: Experimental tunnelling currents and bias voltages for the $c(4\times 2)$ surface reconstructions. The reconstructions proposed by Erdman[16] were not observed by STM.

sides of the rhombus representing the surface unit cell in Figure (5.7c).

Figure (6.16a) shows the electronic density in the same slice, the topmost black circles with a white spot in the centre represent Figure's (5.7c) O1 atoms. Figures (6.16c) and (6.16d) show the electronic density and the density of states for a slice parallel to the previous one and at a distance of one quarter the length of the rhombus' side. In Figure (6.16c), the topmost atoms are Figure (5.7c)'s O3 atoms, which are represented by a small white circle. Below and to the right of these atoms, there are Figure (5.7c)'s O4 atoms, represented by white circles with a black spot in their centre. The density of electronic states in Figure (6.16d) have extended, electronically flat regions which, if imaged by STM, are not likely to be bright spots. Finally, Figures (6.16e) and (6.16f) represent the electronic density and the density of states in a slice parallel to the previous one and at a distance of a half the length of the rhombus' side. In Figure (6.16e)

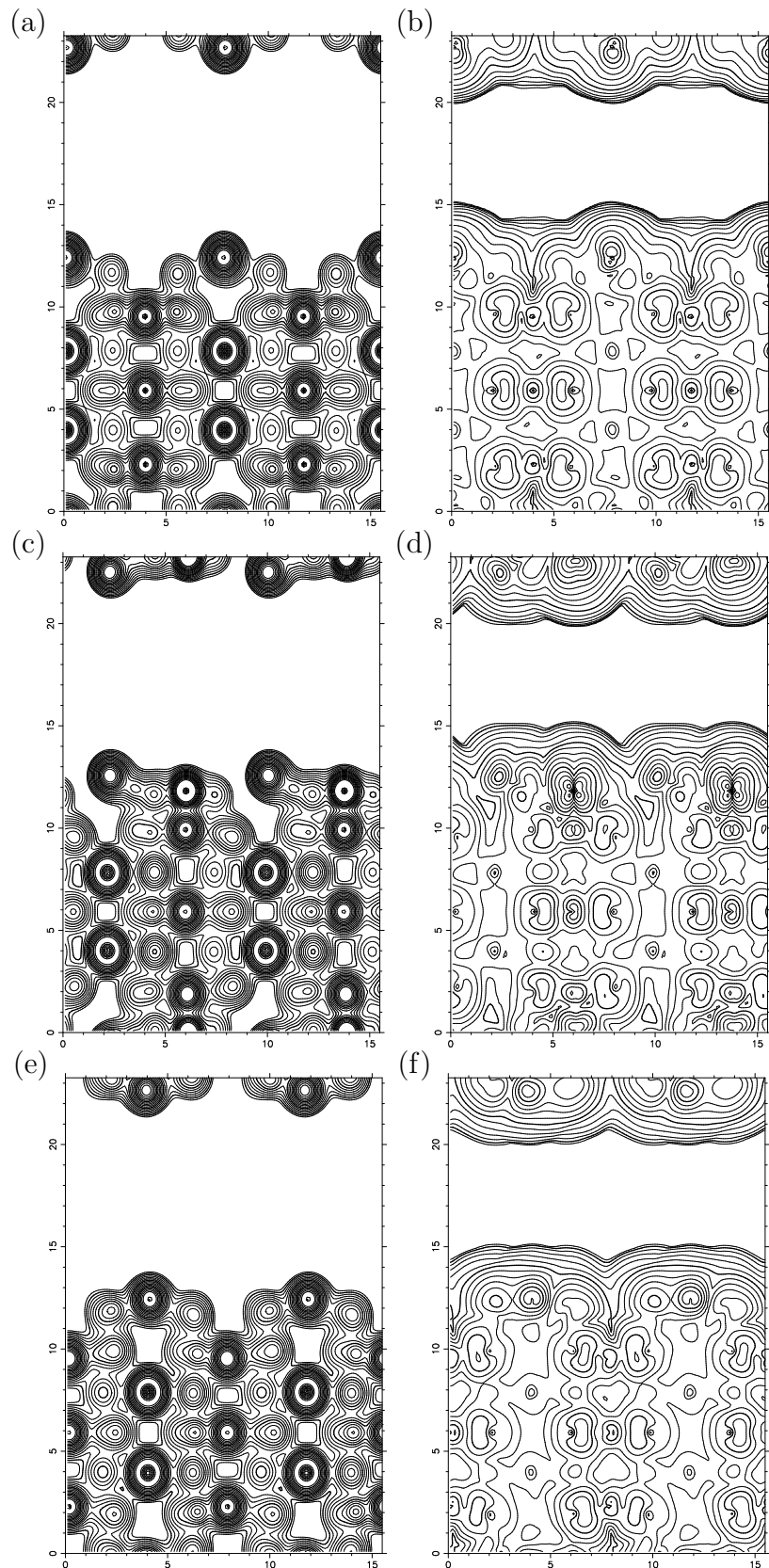


Figure 6.16: Lateral views for the DL-TiO₂-A proposed model for the c(4×2) surface reconstruction. Scales on the axis are in Å. The topmost contours in Figures (6.16b), (6.16d) and (6.16f) are representing constant density of states' values of $1 \times 10^{-7} \frac{\text{number of states}}{\text{Å}^3}$. This is the value we need for the experimental tunnelling current to be of the order of 0.1 nA[90].

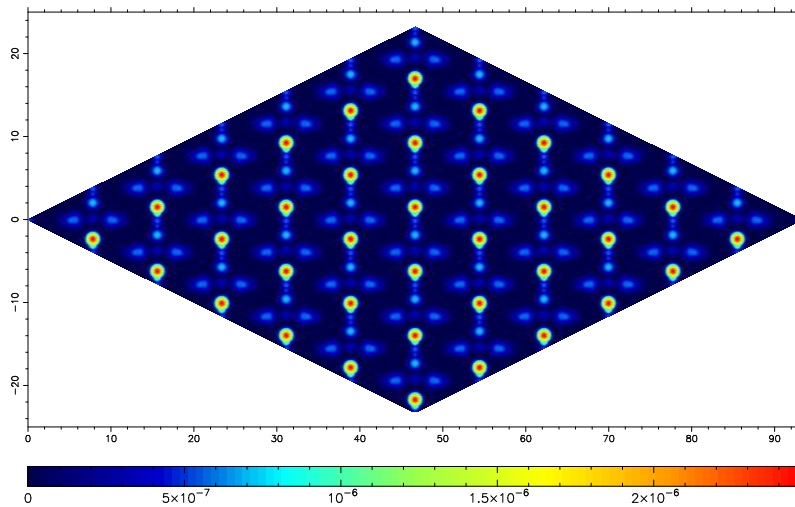


Figure 6.17: Top view $c(4\times 2)$ DL-TiO₂-A. Bias voltage: 2 V

the topmost atoms are Figure (5.7c)'s O₂ atoms. The density of states in Figure (6.16f) is flatter than in Figure (6.16d) and, therefore, it is even more difficult to obtain a STM image with the shape of a bright spot.

Figure (6.17) is the simulated STM image for the TiO₂-DL(A) surface reconstruction with a 2 V bias voltage, which is a geometric pattern of bright spots (red and yellow spots) that has the required $c(4\times 2)$ periodicity. This image is in excellent agreement with the experimental image showed in Figure (6.14b) [11]. However, Figure (6.14a), which was obtained with the same tip², has the same kind of STM image and its bias was 0.87 V. Figure (6.18) shows a simulated STM image with the required 0.87 V bias voltage. Although in Figure (6.18) we have more bright spots, we also clearly have the red and yellow spots (which, according to our interpretation of the STM images, would be easier to image) with the required $c(4\times 2)$ periodicity.

In conclusion, the simulated STM image of the proposed TiO₂-DL(A) model for the $c(4\times 2)$ reconstruction is in excellent agreement with experimental observations.

²As we mentioned at the beginning of this section, Castell[11] observed a significant difference in the atomic surface structure of a SrTiO₃ sample after a change in the STM tip. Except for the tip change, all the others STM parameters remained constant. As our model to simulate STM images explicitly ignores the tip's electronic structure, it cannot account for a tip's change. However, Castell[11] also obtained several STM images of the same surface reconstruction, using the same tip but changing the STM parameters. In such cases we simulated the corresponding STM image and compared it with the experiment

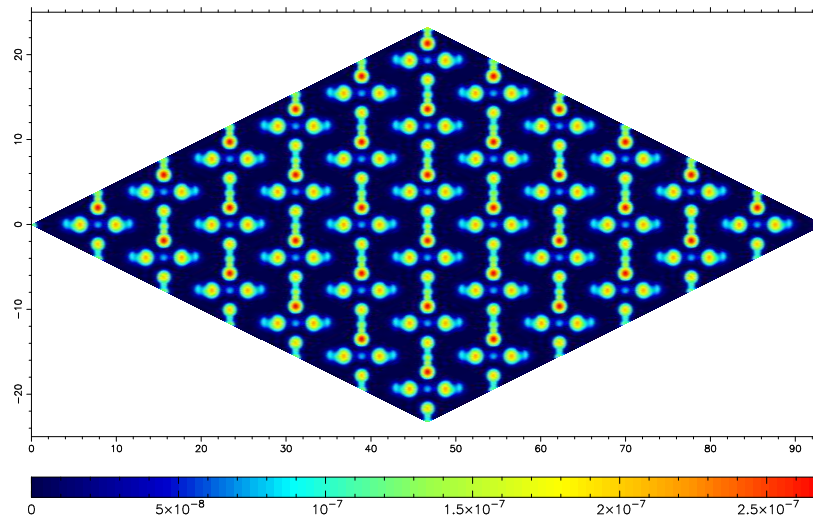


Figure 6.18: Top view of the DL-TiO₂-A model for the $c(4\times 2)$ reconstruction. Bias voltage: 0.87 V . Scales in the axis are in \AA .

The TiO₂-DL(B) reconstruction

Figure (6.19) shows the density of states $n(\mathbf{r})$ in a plane 2.5\AA above the outmost relaxed atoms in the surface, which are oxygens O4 in Figure (5.7d). As we already stated, the bright spots observed in this simulated STM image are regions where the density of states changes abruptly and are easier to image with STM. These high-corrugation regions are placed above the oxygens O4. Figures (6.20a) to (6.20f) show the electronic density and the density of states in slices identical to the ones we used for the TiO₂-DL(A) reconstruction. As before, the density at the uppermost contours in Figures (6.20b), (6.20d) and (6.20f) is 1×10^{-7} , in order to reproduce the right tunnelling current. In the slice depicted in Figure (6.20e) we can see the topmost O4 oxygens. These atoms are represented by a small white oval shape (left O4 atom) and an even smaller white circle (right O4 atom). The reason why the two oxygens appear differently is because, if we think of the line indicating the place in the top view where the slice plane cut the surface unit cell (this line passes through half the length of two parallel rhombus' sides), each of the O4 oxygens are situated on different sides of this line. Below and in between these O4 atoms is Figure (5.7d)'s oxygen O2. In Figure (6.20f) we can see that the density of states' contours extend higher above these O4 atoms. Regarding Figures (6.20b) and (6.20d), we observe their densities of states have more extended and flatter regions, which are not likely to be imaged as spots.

If we place the corners of the rhombus $c(4\times 2)$ unit cell in the centre of the squares defined

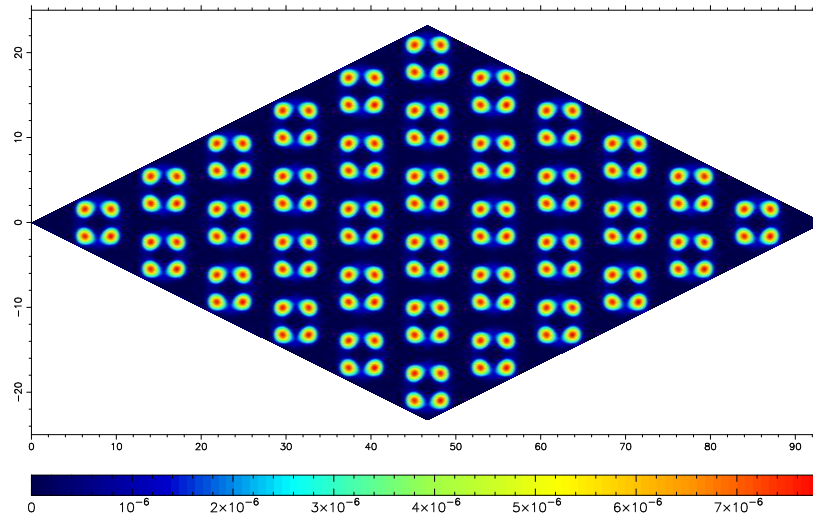


Figure 6.19: Top view $c(4\times 2)$ DL-TiO₂-B. Bias voltage: 2 V. Scales in the axis are in Å.

by the bright spots in Figure (6.19), we will not obtain an image like the one depicted in Figure (6.14c). In this Figure (6.14c), the spots are arranged in rectangles rather than squares and we have two spots per unit cell, while in Figure (6.19) we have four spots per unit cell. However, the spots are arranged with a $c(4\times 2)$ periodicity. We could, for instance, place the corner of the rhombus $c(4\times 2)$ unit cell over the spots on any of the corners of each square of spots. Furthermore, changing the bias voltage to 0.87 V do not affect the simulated STM image.

Finally, although the DL-TiO₂-B model for the $c(4\times 2)$ surface reconstruction has the required periodicity, its simulated STM image does not match the experimental observations as accurately as the DL-TiO₂-A model did.

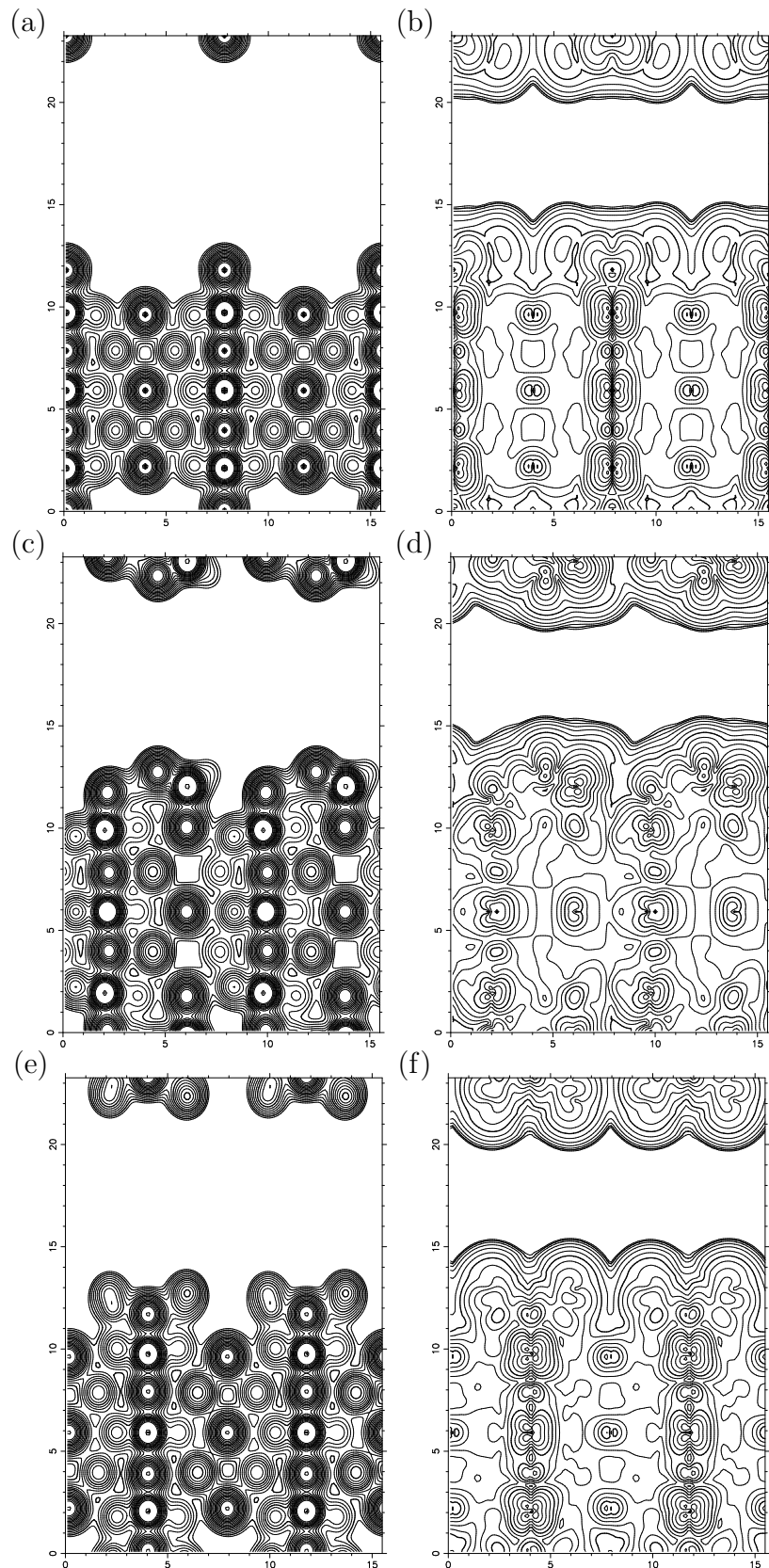


Figure 6.20: Lateral views for the DL-TiO₂-B proposed model for the c(4×2) surface reconstruction. The topmost contours in Figures (6.20b), (6.20d) and (6.20f) represent constant density of states' values of $1 \times 10^{-7} \frac{\text{number of states}}{\text{Å}^3}$. This is the value we need for the experimental tunnelling current to be of the order of $0.1 \text{ nA}[90]$. Scales in the axis are in Å.

The Sr adatom model

Figure (6.21) is the top view of the density of states of the Sr adatom model for the $c(4\times 2)$ reconstruction. Lateral views are in Figures (6.22a) and (6.22b). The top view is for a plane 4\AA above the Sr adatoms on the surface. The lateral views in Figures (6.22a) and (6.22b) show the electronic density and the density of states for a slice passing through the Sr adatoms. From Figure (6.22b) it is clear which are the Sr adatoms, and in Figure (6.22b) we can see that the density of states corrugation is higher above these atoms.

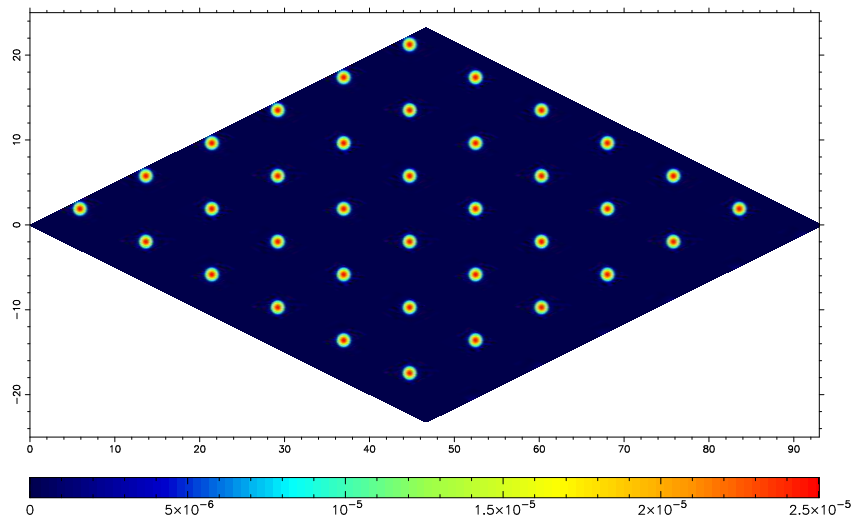


Figure 6.21: Top view $c(4\times 2)$ Kubo and Nozoye[12]. Bias voltage: 0.7 V . Scales in the axis are in \AA .

We have generated the STM images for this model using different bias voltages in addition to the experimental one, namely: 0.7 V , 1 V and 2 V . The obtained images are all similar to Figure (6.22), the density of states corrugation is always higher above the Sr adatoms. We can conclude that the generated STM images for the Sr adatom model of the $c(4\times 2)$ surface reconstruction are in excellent agreement with experimental observations.

The TiO_2 -SL model

Finally, Figure (6.23) shows the simulated STM images of model proposed by Castell [11] to explain the $c(4\times 2)$ reconstruction. This model is shown in Figure (5.12c) and its origin was discussed in Section (6.4). The top view in Figure (6.23a) shows $n(\mathbf{r})$ at a plane 3.5\AA above the topmost atom in the relaxed slab. The bright spots on the picture have the

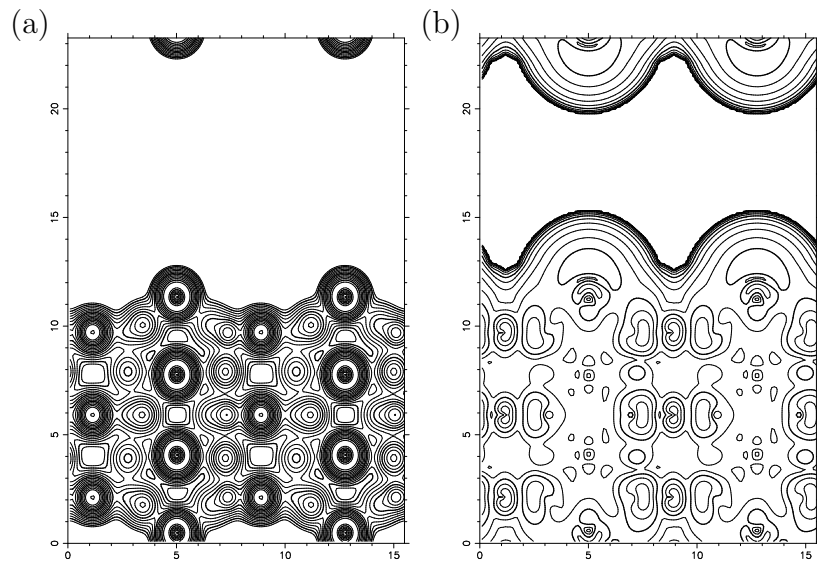


Figure 6.22: Top and lateral views $c(4 \times 2)$ Kubo and Nozoye[12]. Bias voltage: $0.7 V$. The topmost contour in Figure (6.22b), is representing a constant density of states' value of $3 \times 10^{-8} \frac{\text{number of states}}{\text{\AA}^3}$. This is the value we need for the experimental tunnelling current to be of the order of $0.03 nA$ [90]. Scales in the axis are in \AA .

required $c(4 \times 2)$ periodicity for the surface unit cell. These bright spots are above the Ti atoms on the surface unit cell, indicating that the density of states corrugation is higher there. The surface oxygens were not observed on this picture. If we change the energy window for integration to $0.25 V$, the simulated STM picture remains the same³.

Figures (6.23b) and (6.23c) are the electronic density and the density of states in a slice passing through the topmost Ti atoms, along one of the rhombus' sides in the unit cell. These Ti atoms are the outermost relaxed atoms in Figure (6.23c). In Figure (6.23b), we can clearly see that the density of states will be higher above these atoms. Figures (6.23e) and (6.23d) are the electronic and states' densities in a slice passing through the surface oxygen atoms in a slice parallel to the previous one and at a distance of a half the length of the rhombus' side. The surface oxygens atoms are the topmost atoms in Figure (6.23d), and we can see from this picture that they are placed below the topmost Ti atoms in Figure (6.23e).

³A bias voltage of $0.25 V$ was used in Figure (6.14c). This image was observed when the STM tip was changed. The periodic rectangular pattern of bright spots was associated with oxygen atoms

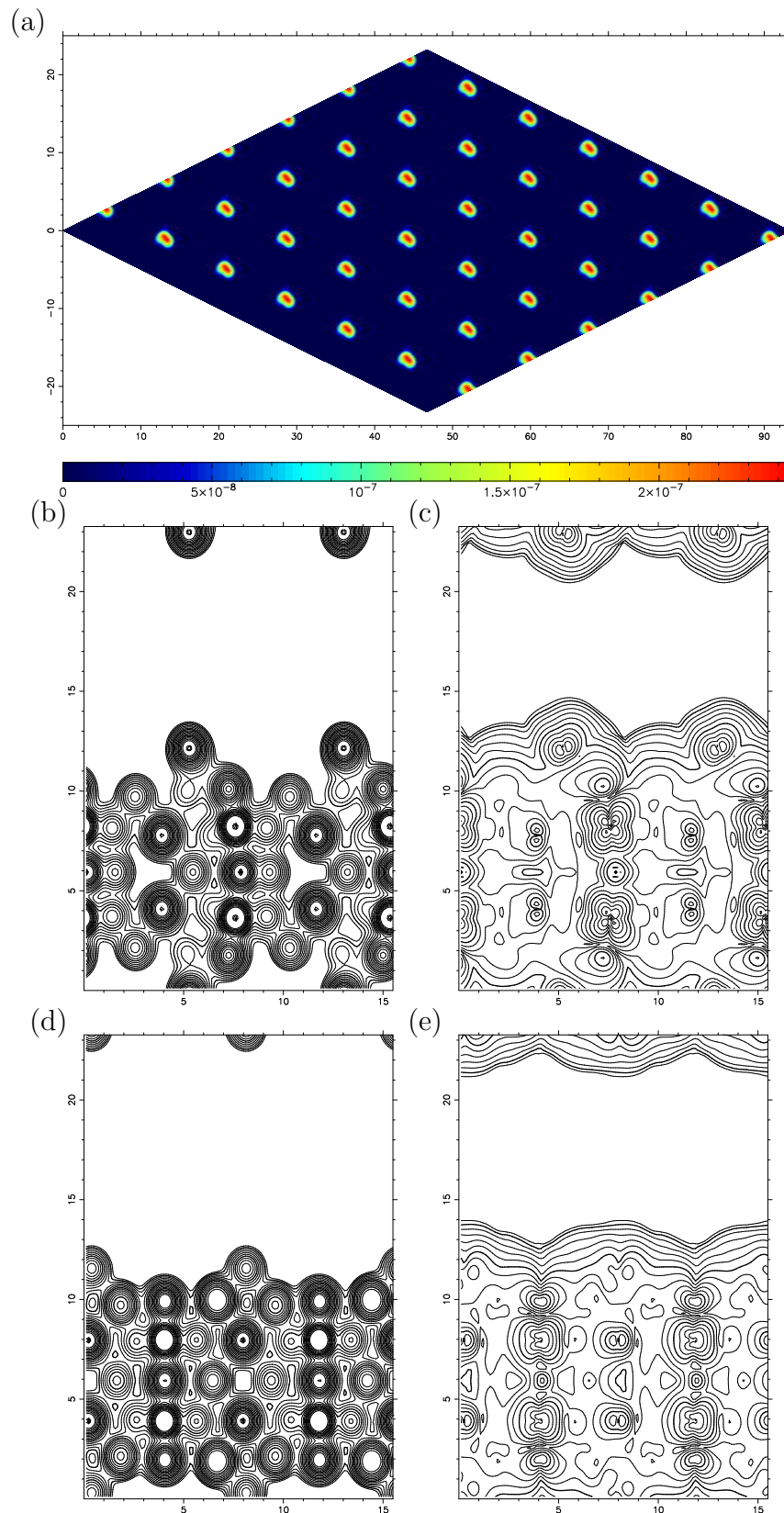


Figure 6.23: Top and lateral views of the SL-TiO₂ model for the $c(4 \times 2)$ reconstruction proposed by Castell [11]. The experimental bias voltage was $2V$. The topmost contours in Figures (6.23b) and (6.23d) represent constant density of states' values of $1 \times 10^{-7} \frac{\text{number of states}}{\text{\AA}^3}$. This is the value we need for the experimental tunnelling current to be of the order of $0.1 nA$ [90]. Scales in the axis are in \AA .

The density of states corrugation is higher above these oxygen atoms but is not as high as the one above titanium atoms in Figure (6.23b), which means the titaniums atoms are imaged easier than the oxygens. The density of states' value in Figures (6.23b) and (6.23d) uppermost iso-lines is $1 \times 10^{-7} \frac{\text{number of states}}{\text{\AA}^3}$.

The agreement between experimental and simulated STM pictures is very good.

6.5 Summary of results

Table (6.4) summarises the large number of results presented in this chapter. Except for the TiO₂-DL1 model, the depicted corrugation for the (2 × 1) surface reconstructions is along the length of the rectangular unit cell. In the TiO₂-DL1 model, the depicted corrugation is in the direction perpendicular to the bright rows in Figure (6.13a).

Surface reconstruction	Maximum Corrugation [Å]	Agreement with experimental STM?
Sr adatom structures		
($\sqrt{13} \times \sqrt{13}$) [12]	2.5	Yes
c(4 × 4) [12]	2	Yes
($\sqrt{5} \times \sqrt{5}$) [12, 13]	2	Yes
(2 × 2) [12]	2.5	Yes
c(4 × 2)		
TiO ₂ -SL[11]	2	Yes
TiO ₂ -DL(A)[16]	1	Yes
TiO ₂ -DL(B)[16]	1.5	No
Sr adatom[12]	2.5	Yes
(2 × 1)		
TiO ₂ -SL[11]	3	Yes
TiO ₂ -DL[15]	2	Yes
Ti ₂ O ₃ -SL[11]	0.5	Yes
Sr adatom[12]	2.5	Yes
TiO ₂ -DL1 [16]	1	No

Table 6.4: Brief summary of results on the simulated STM images.

Chapter 7

Conclusions

I have described a theoretical framework within which the surface energy of an ordered compound can be calculated as a function of external variables defining the state of the system, namely the temperature, chemical potential of one of its components and partial pressure of oxygen. Special attention was paid to how the surface energy dependence on the environmental parameters can be approximated with rather simple analytical expressions, in particular the vibrational contributions to the surface energy.

Within this framework and using the SIESTA[61] method, I have performed first principles total energy calculations for different atomic scale reconstructions proposed for the (001) surface of SrTiO₃. I focused in the Sr adatom model[12] and the double layer model[15]. However, I also performed calculations for other proposed surface structures, like the ones M. Castell[11] and us proposed for the (2×1) and c(4×2) observed surface reconstructions. The surface energies were calculated as a function of TiO₂ chemical potential, temperature and oxygen partial pressure for the conditions under which the substrate is thermodynamically stable.

Spatially resolved densities of states were calculated for every proposed model, in order to simulate STM images and compare them with the experimentally observed ones. There are basically two sources of error in the simulated STM images: the difference between physical excitation energies and DFT calculated band structures, and the error attributed to the simplification of tip structure in the calculation of the tunnelling current. The error in the band structures is inherent to DFT calculations. However, the use of DFT calculated band structures has already lead to successful STM image simulations for a large number

of different oxide surfaces [94, 36]. On the other hand, the error due to the simplification of the tip structure is more difficult to assess. From Figures (6.14) we know that STM image contrast variation is observed on the $c(4\times 2)$ surface reconstruction of SrTiO_3 due to a tip change. However, I obtained excellent agreement between experimentally observed STM images and the simulated ones for three of the four proposed models for the $c(4\times 2)$ reconstruction. There is disagreement only in the case of the $c(4\times 2)$ -DL(B) reconstruction. Nevertheless, since the bright spots on the simulated image of the $c(4\times 2)$ -DL(B)/(A) proposed models are above the uppermost relaxed oxygens at each surface, it seems that the disagreement between STM theoretical and experimental images seems to be due to the particular physical geometry of $c(4\times 2)$ -DL(B) rather than to tip effects. However, as Castell pointed out [11], the tip change might allow to image different surface sub-layers, and to properly account for these effects the tip's contribution should be explicitly treated.

7.1 The Sr adatom model

One of the things in favour of the Sr adatom model as a plausible model for the $\text{SrTiO}_3(001)$ surface reconstructions is the fact that its simulated STM images are in excellent agreement with the experimentally observed ones. Several authors proposed that the bright spots of STM images are due to oxygen vacancies [18, 95]. Using this model, the number of STM spots should increase with further annealing in UHV [97]. In contrast, the number of STM spots decreased with annealing, as shown in Figure (5.2)(a)-(c). These results indicate that the oxygen vacancy model is unacceptable. However, one of the key issues to be addressed is how Sr adatoms can appear in a $\text{TiO}_2(1\times 1)$ -terminated surface. The explanation to this fact lies in the procedure and the experimental conditions used in the preparation of the samples. Kubo and Nozoye [12] used the methodology proposed by Kawasaki et al [7] to prepare their samples. This methodology uses a wet solution that dissolves the basic SrO atomic layer. This selective dissolution can be achieved using a buffer solution (BHF) whose pH values can be controlled. An atomically smooth surface terminated in a TiO_2 plane can be obtained. However, it may be possible that small clusters appear on the TiO_2 terminated surface, as it has been observed by Kubo and Nozoye [12]. Experimental evidence [17] suggests that these clusters have the composition SrO_x . Kubo and Nozoye [12] observed these clusters after heating their samples at 1273 K, they were coexisting with the surface reconstruction's geometric patterns of bright spots. There is conclusive experimental evidence [23, 98, 99, 100] that Sr and/or SrO_x segregate to the surface under

oxidative conditions, while Ti and/or TiO_x segregate under reducing conditions. In both cases, segregation occurs under extreme annealing conditions, such as 40 hs annealing at 1000°C [98] and 100 hs at 800°C [100]. As the Kubo and Nozoye samples were lightly reduced in UHV, it is unlikely that the Sr adatoms come from internal segregation towards the surface. Instead, it was proposed that Sr adatoms come from surface migration of Sr and SrO_x from the clusters [12].

In conclusion, I have studied surface structures that were proposed by Kubo and Nozoye to explain a set of structural phase transitions on the $\text{SrTiO}_3(001)$ surface. The different surface structures that were observed using an STM and our simulated STM images are in excellent agreement with the experimental ones. Besides, the kinetics of the system is explained very well by the Sr adatom model. However, from Figures (5.4a) and (5.4b) it is clear that only surfaces with coverage of $\Theta=0.25$ and $\Theta=0.20$ are stable for the ranges of temperature and pressure reported by Kubo and Nozoye, and only when the system is in equilibrium with SrO. My calculations show that the lower Sr coverage implied in the Sr adatom model can only be explained if the surface is far from equilibrium, in a transient state as it loses Sr to the environment.

7.2 The (2×1) surface reconstructions

From the surface energy plots in Figures (5.14) it can be seen that the most energetically stable surface reconstructions do not have a (2×1) periodicity. In equilibrium with TiO_2 , the reconstruction with the lowest surface energy is the $(\sqrt{2}\times\sqrt{2})R45^\circ$ one, while in equilibrium with SrO the (1×1) SrO-terminated reconstruction is the most stable. According to Johnston and coworkers [36], the (1×1) SrO terminated surface reconstruction is electronically flat and it should be difficult to obtain STM images from it. Moreover, these authors suggest that both of the (1×1) reconstructions may not even exist in practice.

Kubo and Nozoye are the only authors to provide some evidence of the $\text{SrTiO}_3(001)$ surface reconstructions being in equilibrium with SrO [12, 17]. However, they did not experimentally observe the (2×1) reconstruction. Kubo and Nozoye [12] proposed the Sr adatom model of Figure (5.9b) for the (2×1) surface reconstruction. Assuming that the mechanism of the structural surface phase transitions observed in Figure (5.2) is the one they proposed in reference [12], they used their (2×1) model to explain the $(2\times 1)\rightarrow c(4\times 4)$

surface phase transition observed by Castell [11]. The simulated STM images of the Sr adatom model presented in Figures (6.11) are in excellent agreement with the experimentally observed ones. The experimental STM images of the (2×1) surface reconstruction are bright rows separated by around 0.8 nm (the separation distance is equivalent to two unit cells). The periodicity along these bright lines cannot be resolved by STM, but is known from LEED [11] to be one single unit cell. In the simulated images, the electronic corrugation along the length of the rectangular unit cell is larger than along the width. This means that it would be easier to get resolution in a direction along the length of the unit cell: the vertical lines of spots in Figure (6.11a) could actually be experimentally imaged as lines. Regarding the stability of this model, from Figure (5.14b) we can see that, except for the (1×1) SrO terminated surface, the Sr adatom model for the (2×1) surface reconstruction is the most stable reconstruction at $p_{O_2} \leq 1 \times 10^{-40}$ atm. Above that oxygen partial pressure, the TiO_2 -SL surface reconstruction is the most stable and its surface energy does not depend on the oxygen pressure. This reconstruction's simulated STM image is in Figure (6.8a), and agrees very well with the experimental one. The Ti_2O_3 -SL and the TiO_2 -DL reconstructions, whose surface energies are greater than the TiO_2 -SL reconstruction, have also simulated STM images in agreement with the experimental ones, but these reconstructions are certainly not stable.

In this analysis, there has been no consideration of the vibrational contributions to the surface energy. However, vibrational contributions to the TiO_2 -SL and TiO_2 -DL reconstructions would need to be of the order of $0.3\frac{J}{m^2}$ and $3\frac{J}{m^2}$ respectively, for any of these reconstructions to become more stable than the Sr adatom model of the (2×1) reconstruction. Estimations of these contributions are presented in Figures (3.1) and (5.8) where it can be seen that in no case are larger than $0.2\frac{J}{m^2}$.

In equilibrium with TiO_2 the situation is different. Vibrational contributions can lower the TiO_2 -DL surface energy to $1.58\frac{J}{m^2}$. Thus, the TiO_2 -DL reconstruction becomes more stable than the SrO (1×1) reconstruction for the entire p_{O_2} range. However, the TiO_2 and $(\sqrt{2} \times \sqrt{2})R45^\circ$ reconstructions are both more stable than the TiO_2 -DL one. These reconstructions have enough density of states corrugation to be imaged using a STM, although the periodicity of their simulated images is not (2×1) . In any case, to date there is no experimental STM images of any of the (1×1) reconstructions and it has been suggested that they may not be real[36]. As regards the $(\sqrt{2} \times \sqrt{2})R45^\circ$ reconstruction, its simulated

STM images in Figure (6.13) show that it can be imaged as bright rows, but the separation between rows is less than two units cells. Although the STM image of this reconstruction has *not* the experimentally observed periodicity, I thought it is important to present it in this work because, to the best of my knowledge, *it is the first SrTiO₃(001) surface reconstruction to be more stable than the (1×1) terminated ones*¹.

It can be concluded that, if the (1×1) reconstructions are considered as unrealistic ones, in equilibrium with SrO and under conditions of very low pressure ($1 \times 10^{-45} \leq p_{O_2} \leq 1 \times 10^{-40}$), the Sr adatom model could be the stable (2×1) reconstruction observed by STM. Similarly, at $p_{O_2} \geq 1 \times 10^{-40}$, the TiO₂-SL reconstruction becomes the most stable surface that can be imaged by STM. On the other hand, in equilibrium with TiO₂, the TiO₂-DL reconstruction would be the stable (2×1) reconstruction imaged by STM.

7.3 The c(4×2) surface reconstructions

The surface's energies in Figure (5.15) suggests that, depending on the values of the environmental variables, we can have energetically stable c(4×2) surface reconstructions. Even more stable than the (1×1) terminated ones.

Only Kubo and Nozoye[12] present some evidence of c(4×2) reconstructions being in equilibrium with SrO. Figure (5.15b) shows c(4×2) reconstructions' surface energy in this equilibrium case. Again, only assuming the (1×1) reconstructions are unreal, the Sr adatom model for the c(4×2) reconstruction is a suitable equilibrium model which can be imaged by STM. Vibrational contributions are negligible here, we would need them to be of the order of $1 \frac{J}{m^2}$ to lower surface energy of the c(4×2)-DL(B) in order for it to be as stable as the Sr adatom model at $p_{O_2} = 1 atm$. On the other hand, in equilibrium with TiO₂ (Figure (5.15a)) vibrational contributions play a crucial role. In this case, the c(4×2)-DL(B) reconstruction is as stable as the (1×1) TiO₂ reconstruction, and the c(4×2)-DL(A) is around $0.2 \frac{J}{m^2}$ above the (1×1) SrO reconstruction. The vibrational contributions could lower the surface energy of the c(4×2)-DL(B) reconstruction by $0.2 \frac{J}{m^2}$, and the surface energy of the c(4×2)-DL(A) reconstruction by $0.25 \frac{J}{m^2}$. Considering these values, the c(4×2)-DL(B) reconstruction becomes the most stable one, while c(4×2)-DL(A) reconstruction becomes

¹Without including the vibrational contributions.

more stable than the (1×1) SrO reconstruction (although not more stable than the (1×1) TiO_2 reconstruction nor the $c(4 \times 2)$ -DL(B)). The simulated STM image for the $c(4 \times 2)$ -DL(B) reconstruction has the required $c(4 \times 2)$ periodicity, but it is not related to any of the experimentally observed STM images of $c(4 \times 2)$ reconstructions. This simulated image remains the same after a change in the bias voltage. As regards the $c(4 \times 2)$ -DL(A) reconstruction, its simulated STM image agrees very well with the experimentally observed one. When we change the bias voltage, the simulated image changes slightly (Figure (6.17) \rightarrow Figure (6.18)) but it still keeps the required $c(4 \times 2)$ periodicity.

Finally, I conclude by saying that reconstruction $c(4 \times 2)$ -DL(B) should be considered as a stable model for the $c(4 \times 2)$, when the system is in equilibrium with TiO_2 . The experimental evidence from Figures (5.13), the theoretical calculations from Figure (5.15a) and the density of states corrugation from Figure (6.20) strongly support the fact that we should expect reconstruction $c(4 \times 2)$ -DL(B) to be experimentally imaged by STM. The stable reconstruction in equilibrium with TiO_2 , whose simulated STM image better matches the $c(4 \times 2)$ geometric pattern of bright spots, is $c(4 \times 2)$ -DL(A) provided it is assumed the (1×1) reconstructions do not exist in reality. As regards the $c(4 \times 2)$ - TiO_2 -SL model proposed by Castell [11], although its simulated image is in excellent agreement with the experimentally observed ones, its surface energy is too high for this reconstruction to be considered a stable model for the $c(4 \times 2)$ surface reconstruction.

7.4 Open questions and future work

I believe that the double layer model deserves to be studied in more detail. The double layer model for the $c(4 \times 2)$ surface reconstruction has proven to be as stable as the (1×1) reconstructions, even without considering the vibrational contributions to the surface energy. Moreover, the $(\sqrt{2} \times \sqrt{2})R45^\circ$ reconstruction has been found to be stable in equilibrium with TiO_2 . Why the surface energy of these double layer reconstructions is so low? Is it related with the electrostatics? At the moment I have proposed several double layer models for the $(\sqrt{5} \times \sqrt{5})$ surface reconstruction, and I am performing first principles calculations to calculate their surface energy. This $(\sqrt{5} \times \sqrt{5})$ surface reconstruction was experimentally observed using STM by M. Castell and D. Newell from Oxford University. Besides, the vibrational contributions to the surface energy have proven to be very important in the double layer model. My idea is to fully calculate these vibrational contributions

by calculating the full phonon frequencies of different proposed double layer models. To do this from first principles I intend to use the parallel version of SIESTA. The ultimate goal of all these calculation is to understand, in terms of the double layer model, an underlying structure formation rule for the (001) surface of Strontium Titanate.

Another important issue that should be addressed are the steps on the (001) surface. So far, I only know one theoretical study on steps on this surface [35], despite the important role steps are known to play in the reconstruction of surfaces [101]. Little is known about $\text{SrTiO}_3(001)$ step structures: the mechanism that creates them, step-step interaction, step energies, kink energies and chemistry. Moreover, on some of the STM images presented on this thesis (Figures (1.3) and (1.2)) it can be seen that different steps are related with different atomic scale reconstructions on their corresponding terraces. First principles calculations should be performed to estimate steps energies on different surface reconstructions. Given the sizes of the slabs involved, the use of the parallel version of SIESTA could be more appropriate.

Finally, the number of atomic scale surface reconstructions that were observed by STM on the $\text{SrTiO}_3(001)$ surface are remarkable. Among these structures there are nanostructures [24], the $c(6 \times 2)$ long-range atomically ordered surface reconstruction [8] and, more recently observed, a long-range ordered vicinal surface [102]. As part of the future work, it will certainly be necessary to use ab initio modelling to be able to resolve the detailed atomic structure of the aforementioned reconstructions.

Chapter 8

Appendix

Einstein model for the vibrational contributions to the Gibbs free energy.

Using the Einstein model, the expression for the surface vibrational free energy in Equation (3.17) is given by

$$\begin{aligned}
\sigma_{Vib}(T) = & \\
& = \frac{3}{2A_s} \left[\frac{\hbar C_{sup}}{2} \left(n_{Sr}^{Sup} \omega_{Sr}^{SrTiO_3} + n_{Ti}^{Sup} \omega_{Ti}^{SrTiO_3} + n_O^{Sup} \omega_O^{SrTiO_3} \right) \right] + \\
& \frac{3}{2A_s} n_{Sr}^{Sup} \left[k_B T \ln \left(1 - \exp \left(-\frac{\hbar \omega_{Sr}^{SrTiO_3} C_{sup}}{k_B T} \right) \right) \right] + \\
& \frac{3}{2A_s} n_{Ti}^{Sup} \left[k_B T \ln \left(1 - \exp \left(-\frac{\hbar \omega_{Ti}^{SrTiO_3} C_{sup}}{k_B T} \right) \right) \right] + \\
& \frac{3}{2A_s} n_O^{Sup} \left[k_B T \ln \left(1 - \exp \left(-\frac{\hbar \omega_O^{SrTiO_3} C_{sup}}{k_B T} \right) \right) \right] + \\
& \frac{3}{2A_s} (n_{Sr}^{slab} - N_{SrO}) \left[\frac{\hbar \omega_{Sr}^{SrTiO_3}}{2} + k_B T \ln \left(1 - \exp \left(-\frac{\hbar \omega_{Sr}^{SrTiO_3}}{k_B T} \right) \right) \right] + \tag{8.1} \\
& \frac{3}{2A_s} (n_{Ti}^{slab} - N_{SrO}) \left[\frac{\hbar \omega_{Ti}^{SrTiO_3}}{2} + k_B T \ln \left(1 - \exp \left(-\frac{\hbar \omega_{Ti}^{SrTiO_3}}{k_B T} \right) \right) \right] + \\
& \frac{3}{2A_s} (n_O^{slab} - 3N_{SrO}) \left[\frac{\hbar \omega_O^{SrTiO_3}}{2} + k_B T \ln \left(1 - \exp \left(-\frac{\hbar \omega_O^{SrTiO_3}}{k_B T} \right) \right) \right] - \\
& \frac{3}{2A_s} (N_{TiO_2} - N_{SrO}) \left[\frac{\hbar \omega_{Ti}^{TiO_2}}{2} + k_B T \ln \left(1 - \exp \left(-\frac{\hbar \omega_{Ti}^{TiO_2}}{k_B T} \right) \right) \right] - \\
& \frac{3}{2A_s} 2(N_{TiO_2} - N_{SrO}) \left[\frac{\hbar \omega_O^{TiO_2}}{2} + k_B T \ln \left(1 - \exp \left(-\frac{\hbar \omega_O^{TiO_2}}{k_B T} \right) \right) \right]
\end{aligned}$$

In this expression n_{Sr}^{sup} , n_{Ti}^{sup} and n_O^{sup} are the number of strontiums, titaniums and oxygens in the slab's surface layers, while n_{Sr}^{slab} , n_{Ti}^{slab} and n_O^{slab} are the number of strontiums, titaniums and oxygens in the slab, excluding the surface layers. C_{sup} is a constant that gives the percentage of variation of the atom's vibrational mode at the surface.

The crucial parameters in this formula are the ω 's. Table (8.1) shows the values we adopted. Cowley[45] studied the lattice dynamics of SrTiO₃ both experimentally and theoretically.

Frequency	value [$\frac{1}{s}$]	Optical mode	Ions displaced in the normal mode
$\omega_O^{SrTiO_3}$	4.5×10^{12}	TO	O _z
$\omega_{Sr}^{SrTiO_3}$	3.75×10^{12}	TO	Sr _x , O _x
$\omega_{Ti}^{SrTiO_3}$	5.0×10^{12}	TO	Ti _x , O _x
$\omega_O^{TiO_2}$	15×10^{12}	TO	Ti _{x-y} , O _{x-y}
$\omega_{Ti}^{TiO_2}$	12.5×10^{12}	Silent	Ti _{x-y}

Table 8.1: Values for the frequencies in the Einstein model.

He measured the frequency vs wave-vector dispersion curves, for some of the normal modes propagating along the [1,0,0] direction in the Brillouin zone, using neutron spectrometry. He used parametric models to fit the aforementioned dispersion curves, obtaining a reasonable agreement with experiment.

Similarly, Taylor and coworkers[103] studied the lattice dynamics of rutile.

Our criteria for adopting a particular frequency was related to the density of normal modes and the ions displacements associated with a particular normal mode. For instance, for strontium, among the experimentally observed and theoretically fitted normal modes that are within a frequency range with a high density of normal modes, we chose a frequency which has strontiums atoms as its associated displaced ions.

Normal frequencies and analytical expressions for the vibrational contributions of the oxygens in the double-layer model.

The values of ω_i^i for the bulk oxygens and the surface oxygens in each surface reconstruction are given in the following tables:

Bulk Oxygens		
O_{SrTiO_3}	$\omega_1 = 1.46 \times 10^{13}$	$\vec{v}_1 = (-0.31, 1, -1.13 \times 10^{-5})$
	$\omega_2 = 1.45 \times 10^{13}$	$\vec{v}_2 = (1, 0.31, 2 \times 10^{-5})$
	$\omega_3 = 2.96 \times 10^{13}$	$\vec{v}_3 = (1.28, 6.42 \times 10^{-6}, 1)$
O_{TiO_2}	$\omega_1 = 3.29 \times 10^{13}$	$\vec{v}_1 = (1, 0.45, 1.2 \times 10^{-4})$
	$\omega_2 = 3.40 \times 10^{13}$	$\vec{v}_2 = (0.3, 1, 0.7 \times 10^{-5})$
	$\omega_3 = 1.68 \times 10^{13}$	$\vec{v}_3 = (0.01, 1.3 \times 10^{-5}, 1)$

(2×1) DL-TiO ₂		
O_1	$\omega_1 = 1.87 \times 10^{13}$	$\vec{v}_1 = (1, 8.4 \times 10^{-3}, 0.16)$
	$\omega_2 = 2.46 \times 10^{13}$	$\vec{v}_2 = (-0.164, 6.8 \times 10^{-2}, 1)$
	$\omega_3 = 2.54 \times 10^{13}$	$\vec{v}_3 = (-2.92 \times 10^{-3}, 1, -4.55 \times 10^{-2})$
O_2	$\omega_1 = 2.57 \times 10^{13}$	$\vec{v}_1 = (1, -7.13 \times 10^{-3}, 5.34 \times 10^{-2})$
	$\omega_2 = 1.64 \times 10^{13}$	$\vec{v}_2 = (1.14 \times 10^{-2}, 1, -0.11)$
	$\omega_3 = 1.46 \times 10^{13}$	$\vec{v}_3 = (-4.89 \times 10^{-2}, 0.11, 1)$
O_3	$\omega_1 = 6.30 \times 10^{12}$	$\vec{v}_1 = (1, 6.36 \times 10^{-3}, 0.45)$
	$\omega_2 = 4.33 \times 10^{13}$	$\vec{v}_2 = (-0.46, -2.41 \times 10^{-4}, 1)$
	$\omega_3 = 7.49 \times 10^{12}$	$\vec{v}_3 = (1.38 \times 10^{-2}, 1, 6.57 \times 10^{-3})$
O_4	$\omega_1 = 3.37 \times 10^{13}$	$\vec{v}_1 = (1, 1.83 \times 10^{-2}, 4.89 \times 10^{-2})$
	$\omega_2 = 2.36 \times 10^{13}$	$\vec{v}_2 = (-3.11 \times 10^{-2}, -8.23 \times 10^{-2}, 1)$
	$\omega_3 = 1.05 \times 10^{13}$	$\vec{v}_3 = (-2.23 \times 10^{-2}, 1, 8.23 \times 10^{-2})$

(2×1) SL-TiO ₂		
O_1	$\omega_1 = 1.35 \times 10^{13}$	$\vec{v}_1 = (1, 3.33 \times 10^{-3}, 9.36 \times 10^{-5})$
	$\omega_2 = 1.51 \times 10^{13}$	$\vec{v}_2 = (4.34 \times 10^{-3}, -0.714, 1)$
	$\omega_3 = 1.42 \times 10^{13}$	$\vec{v}_3 = (-6.38 \times 10^{-4}, 1, 0.57)$
O_2	$\omega_1 = 1.2 \times 10^{13}$	$\vec{v}_1 = (1, 7.95 \times 10^{-5}, 2.04 \times 10^{-3})$
	$\omega_2 = 2.61 \times 10^{13}$	$\vec{v}_2 = (-1.67 \times 10^{-3}, 6.39 \times 10^{-3}, 1)$
	$\omega_3 = 2.33 \times 10^{13}$	$\vec{v}_3 = (1.47 \times 10^{-6}, 1, -7.42 \times 10^{-3})$

c(4×2) DL-TiO ₂ -A		
O ₁	$\omega_1 = 1.22 \times 10^{13}$	$\vec{v}_1 = (1, 2.20 \times 10^{-4}, -5.97 \times 10^{-7})$
	$\omega_2 = 2.25 \times 10^{13}$	$\vec{v}_2 = (1.86 \times 10^{-4}, 8.23 \times 10^{-2}, 1)$
	$\omega_3 = 1.28 \times 10^{13}$	$\vec{v}_3 = (-1.48 \times 10^{-4}, 1, -8.62 \times 10^{-3})$
O ₂	$\omega_1 = 1.87 \times 10^{13}$	$\vec{v}_1 = (1, 1.75 \times 10^{-3}, 1.99 \times 10^{-3})$
	$\omega_2 = 2.25 \times 10^{13}$	$\vec{v}_2 = (-2.23 \times 10^{-3}, 1, -0.56)$
	$\omega_3 = 1.28 \times 10^{13}$	$\vec{v}_3 = (-3.90 \times 10^{-4}, 0.55, 1)$
O ₃	$\omega_1 = 4.21 \times 10^{13}$	$\vec{v}_1 = (1, -8.6 \times 10^{-3}, 0.44)$
	$\omega_2 = 9.24 \times 10^{12}$	$\vec{v}_2 = (1.84 \times 10^{-2}, 1, -2.18 \times 10^{-2})$
	$\omega_3 = 5.65 \times 10^{12}$	$\vec{v}_3 = (-0.44, 1.12 \times 10^{-2}, 1)$
O ₄	$\omega_1 = 2.53 \times 10^{13}$	$\vec{v}_1 = (0.96, -4.17 \times 10^{-2}, 1)$
	$\omega_2 = 2.62 \times 10^{13}$	$\vec{v}_2 = (-0.99, -0.55, 1)$
	$\omega_3 = 2.33 \times 10^{13}$	$\vec{v}_3 = (-0.27, 1, 0.27)$

c(4×2) DL-TiO ₂ -B		
O ₁	$\omega_1 = 1.14 \times 10^{13}$	$\vec{v}_1 = (1, 3.42 \times 10^{-4}, -3.41 \times 10^{-3})$
	$\omega_2 = 1.84 \times 10^{13}$	$\vec{v}_2 = (1.65 \times 10^{-3}, 1.37 \times 10^{-4}, 1)$
	$\omega_3 = 3.37 \times 10^{13}$	$\vec{v}_3 = (-1.53 \times 10^{-4}, 1, -2.1 \times 10^{-4})$
O ₂	$\omega_1 = 2.48 \times 10^{13}$	$\vec{v}_1 = (1, 1.08 \times 10^{-4}, 3.36 \times 10^{-3})$
	$\omega_2 = 2.71 \times 10^{13}$	$\vec{v}_2 = (-1.84 \times 10^{-3}, 1, -4.33 \times 10^{-3})$
	$\omega_3 = 2.78 \times 10^{13}$	$\vec{v}_3 = (8.42 \times 10^{-4}, 1.03 \times 10^{-2}, 1)$
O ₃	$\omega_1 = 3.16 \times 10^{13}$	$\vec{v}_1 = (1, 5.72 \times 10^{-4}, 4.3 \times 10^{-2})$
	$\omega_2 = 2.57 \times 10^{12}$	$\vec{v}_2 = (4.99 \times 10^{-2}, 5.77 \times 10^{-3}, 1)$
	$\omega_3 = 1.08 \times 10^{12}$	$\vec{v}_3 = (-2.89 \times 10^{-4}, 1, -4.39 \times 10^{-3})$
O ₄	$\omega_1 = 1.06 \times 10^{13}$	$\vec{v}_1 = (0.56, -0.58, 1)$
	$\omega_2 = 2.89 \times 10^{13}$	$\vec{v}_2 = (1, -0.18, -0.52)$
	$\omega_3 = 2.66 \times 10^{13}$	$\vec{v}_3 = (0.11, 1, 0.51)$

The analytical expression for the vibrational contribution of the oxygens to the surface free energy in the (2×1) DL-TiO₂ surface reconstruction is given by

$$\begin{aligned}
\sigma_{Vib}(T) &= 2 \sum_{i=1}^4 F_{Vib}^{O^i_{surf}}(T) - 8F_{Vib}^{OTiO_2}(T) = \\
&= 2 \sum_{i=1}^4 \sum_{l=1}^3 \left[\frac{\hbar}{2} \omega_l^i + kT \ln \left(1 - e^{-\frac{\hbar \omega_l^i}{kT}} \right) \right] - \\
&\quad - 8 \sum_{l=1}^3 \left[\frac{\hbar}{2} \omega_l^i + kT \ln \left(1 - e^{-\frac{\hbar \omega_l^i}{kT}} \right) \right]
\end{aligned} \tag{8.2}$$

while for the c(4×2) DL-TiO₂-A/B surface reconstruction is given by

$$\begin{aligned}
\sigma_{Vib}(T) &= 2 \sum_{i=1}^8 F_{Vib}^{O^i_{surf}}(T) - 16F_{Vib}^{OTiO_2}(T) = \\
&= 2 \sum_{i=1}^8 \sum_{l=1}^3 \left[\frac{\hbar}{2} \omega_l^i + kT \ln \left(1 - e^{-\frac{\hbar \omega_l^i}{kT}} \right) \right] - \\
&\quad - 16 \sum_{l=1}^3 \left[\frac{\hbar}{2} \omega_l^i + kT \ln \left(1 - e^{-\frac{\hbar \omega_l^i}{kT}} \right) \right]
\end{aligned} \tag{8.3}$$

Bibliography

- [1] V. C. Matijasevic, B. Ilge, G. Rietveld, F. Tuinstra, and J. E. Mooij. Nucleation of a complex oxide during epitaxial film growth: $\text{SmBa}_2\text{Cu}_3\text{O}_y$ on SrTiO_3 . *Physical Review Letters*, 76:4765–4768, 1996.
- [2] Y. A. Boikov, Z. G. Ivanov, A. N. Kiselev, E. Olsson, and T. Claeson. Epitaxial $\text{YBaCuO}/\text{BaSrTiO}_3$ heterostructures on silicon-on-sapphire for tunable microwave components. *Journal of Applied Physics*, 78:4591–4595, 1995.
- [3] R. A. McKee, F. J. Walker, and M. F. Chisholm. Crystalline oxides on silicon: the first monolayers. *Physical Review Letters*, 81:3014–3017, 1998.
- [4] K. Pennicot. GaAs meets its match. *Physics World*, 14:6, 2001.
- [5] V. E. Henrich and P. A. Cox. *The Surface Science of Metal Oxides*. Cambridge University Press, 1994.
- [6] C. Noguera. *Physics and Chemistry of Oxide Surfaces*. Cambridge University Press, 1995.
- [7] M. Kawasaki, K. Takahashi, T. Maeda, R. Tsushiya, M. Shinohara, O. Ishiyama, M. Yoshimoto, T. Yonezawa, and H. Koinuma. Atomic control of the SrTiO_3 crystal surface. *Science*, 266:1540–1542, 1994.
- [8] Q. D. Jiang and J. Zegenhagen. $c(6\times 2)$ and $c(4\times 2)$ reconstruction of $\text{SrTiO}_3(001)$. *Surface Science*, 425:343–354, 1999.
- [9] M. Naito and H. Sato. Reflection high-energy electron diffraction study on the SrTiO_3 surface structure. *Physica C*, 229:1–11, 1994.

- [10] Q. D. Jiang and J. Zeguenhagen. SrTiO₃(001)-c(6×2): a long range, atomically ordered surface stable in oxygen and ambient air. *Surface Science*, 367:L42–L46, 1996.
- [11] M. Castell. Scanning tunneling microscopy of reconstructions on the SrTiO₃(001) surface. *Surface Science*, 505:1–13, 2002.
- [12] T. Kubo and H. Nozoye. Surface structure of SrTiO₃(001). *Surface Science*, 542:177–191, 2003.
- [13] T. Kubo and H. Nozoye. Surface structure of SrTiO₃(001)-($\sqrt{5}\times\sqrt{5}$)-R26.6°. *Physical Review Letters*, 86:1801–1804, 2001.
- [14] A. Kazimirov, D. M. Goodner, M. J. Bedzyk, J. Bai, and C.R. Hubbard. X-ray surface diffraction analysis of structural transformations on the (001) surface of oxidized SrTiO₃. *Surface Science*, 429:L711–L716, 2001.
- [15] N. Erdman, K. Poepelmeier, M. Asta, O. Warshkow, D. Ellis, and L. Marks. The structure and chemistry of the TiO₂-rich surface of SrTiO₃(001). *Nature*, 419:55–57, 2002.
- [16] N. Erdman, O. Warschkow, M. Asta, K. Poepelmeier, D. Ellis, and L. Marks. Surface structures of SrTiO₃(001): A TiO₂-rich reconstruction with a c(4×2) unit cell. *Journal of the American Chemical Society*, 125:10050–10056, 2003.
- [17] R. Akiyama, T. Matsumoto, H. Tanaka, and T. Kawai. Electric field and contact interactions of a Tip with adenine molecules on SrTiO₃(001)- $\sqrt{5}\times\sqrt{5}$ surfaces. *Japanese Journal of Applied Physics*, 36:3881–3886, 1997.
- [18] S. Kimura, J. Yamauchi, M. Tsukada, and S. Watanabe. First-principles study on electronic structure of the (001) surface of SrTiO₃. *Physical Review B*, 51:11049–11054, 1995.
- [19] G. Charlton, S. Brennan, C. A. Muryn, R. McGrath, D. Norman, T. S. Turner, and G. Thornton. Surface relaxation of SrTiO₃(001). *Surface Science*, 457:L376–L380, 2000.
- [20] N. Bickel, G. Schmidt, K. Heinz, and K. Müller. Ferroelectric relaxation of the SrTiO₃ surface. *Physical Review Letters*, 62:2009–2011, 1989.

- [21] Y. Liang and D. A. Bonnell. Atomic structures of reduced SrTiO₃(001) surfaces. *Surface Science Letters*, 285:L510–L516, 1993.
- [22] S. N. Ruddlesden and P. Popper. The compound Sr₃Ti₂O₇ and its structure. *Acta Crystallographica*, 11:54–55, 1958.
- [23] K. Szot and W. Speier. Surfaces of reduced and oxidized SrTiO₃ from atomic force microscopy. *Physical Review B*, 60:5909–5926, 1999.
- [24] M. Castell. Nanostructures on the SrTiO₃(001) surface studied by stm. *Surface Science*, 516:33–42, 2002.
- [25] T. Nishimura, A. Ikeda, H. Namba, T. Morishita, and Y. Kido. Structure change of TiO₂-terminated SrTiO₃ surfaces by annealing in O₂ atmosphere and ultrahigh vacuum. *Surface Science*, 421:273–278, 1999.
- [26] Karen Johnston. *Atomic Scale Modeling of Strontium Titanate*. PhD thesis, Faculty of Science and Agriculture, Queen’s University Belfast, 2003.
- [27] T. Hikita, T. Hanada, M. Kudo, and M. Kawai. Structure and electronic state of the TiO₂ and SrO terminated SrTiO₃(001) surfaces. *Surface Science*, 287-288:377–381, 1993.
- [28] Materials Science and Engineering Department Stony Brook University. <http://www.matscieng.sunysb.edu/>, 2005.
- [29] S. Andersson and J. B. Pendry. The surface structure of c(2×2)CO adsorbed on copper and nickel(001) surfaces. *Journal of Physics C: Solid State*, 13:3547–3561, 1980.
- [30] S. Watanabe, T. Hikita, and M. Kawai. Cleaning the surface of SrTiO₃(100) and LaAlO₃(100) under moderate temperature condition by bi adsorption/desorption treatment. *Journal of Vacuum Science and Technology A*, 9:2394–2396, 1991.
- [31] E. Zanazzi and F. Jona. A reliability factor for surface structure determinations by low-energy electron diffraction. *Surface Science*, 62:61–80, 1977.
- [32] D. P. Woodruff and T. A. Delchar. *Modern Techniques of Surface Science*. Cambridge University Press, 1994.

- [33] J. Padilla and D. Vanderbilt. Ab initio study of SrTiO₃ surfaces. *Surface Science*, 418:64–70, 1998.
- [34] C. Cheng, K. Kunc, and M. H. Lee. Structural relaxation and longitudinal dipole moment of SrTiO₃ (001)(1×1) surfaces. *Physical Review B*, 62:10409–10418, 2000.
- [35] X. Zhang and A. Demkov. Steps on the (001) SrTiO₃ surface. *Journal of Vacuum Science and Technology B*, 20:1664–1670, 2002.
- [36] K. Johnston, M. Castell, A. T. Paxton, and M. W. Finnis. SrTiO₃(001)(2x1) reconstructions: first-principles calculations of surface energy and atomic structure compared with scanning tunnelling microscopy images. *Physical Review B*, 70:085415–085427, 2004.
- [37] M. Scheffler. Thermodynamic aspects of bulk and surface defects from first principles calculations. In *Proceedings of the Fourth Symposium on Surface Physics*. Studies in Surface Science and Catalysis 40, September 1987.
- [38] K. Reuter and M. Scheffler. Composition, structure, and stability of RuO₂(110) as a function of oxygen pressure. *Physical Review B*, 65:035406–035422, 2001.
- [39] K. Reuter and M. Scheffler. Composition and structure of the RuO₂(110) surface in an O₂ and CO₂ environment: Implications for the catalytic formation of CO₂ of oxygen pressure. *Physical Review B*, 68:045407–045423, 2003.
- [40] J. Rogal, K. Reuter, and M. Scheffler. On the thermodynamic stability of PdO surfaces. *Physical Review B*, 69:075421–075429, 2004.
- [41] J. W. Cahn. Thermodynamics of solid and fluid surfaces. In *Interfacial Segregation*. American Society for Metals, 1977.
- [42] M. W. Finnis. Accessing the excess: An atomistic approach to excesses at planar defects and dislocations in ordered compounds. *Physica Status Solidi (a)*, 166:397–416, 1998.
- [43] A. Marmier, A. Lozovoi, and M.W. Finnis. The α-alumina (0001) surface: relaxations and dynamics from shell model and density functional theory. *Journal of the European Ceramic Society*, 23:2729–2735, 2003.

- [44] M. B. Taylor, C. E. Sims, G. D. Barrera, N. Allan, and W. C. Mackrodt. Quasiharmonic free energy and derivatives for slabs: Oxide surfaces at elevated temperatures. *Physical Review B*, 59:6742–6751, 1999.
- [45] R. A. Cowley. Lattice dynamics and phase transitions of Strontium Titanate. *Physical Review*, 134:A981–A997, 1964.
- [46] C. Lee, P. Ghosez, and X. Gonze. Lattice dynamics and dielectric properties of incipient ferroelectric TiO_2 rutile. *Physical Review B*, 50:13379–13387, 1994.
- [47] M. W. Finnis, A. Y. Lozovoi, and A. Alavi. The oxidation of NiAl: what can we learn from ab initio calculations? *Annual Review of Materials Research*, 35, 2005.
- [48] W. Li, C. Stampfl, and M. Scheffler. Oxygen adsorption on Ag(111): a density functional theory investigation. *Physical Review B*, 65:075407–075419, 2002.
- [49] J. P. Perdew, K. Burke, and M. Ernzerhof. Generalized gradient approximation made simple. *Physical Review Letters*, 77:3865–3868, 1996.
- [50] P. I. Sorantin and K. Schwartz. Chemical bonding in rutile-type compounds. *Inorganic Chemistry*, 31:567–576, 1992.
- [51] Th. Demuth, Y. Jeanvoine, J. Hafner, and G. Angyan. Polymorphism in silica studied in the local density and generalised-gradient approximations. *Journal of Physics: Condensed Matter*, 11:3833–3874, 1999.
- [52] D. Lide, editor. *CRC Handbook of Chemistry and Physics*. CRC Press, 83rd edition, 2002.
- [53] D. B. Rogers, R. D. Shannon, A. W. Sleight, and J. L. Gillson. Crystal chemistry of metal dioxides with rutile-related structures. *Inorganic Chemistry*, 8:841–849, 1969.
- [54] R. W. G. Wyckoff. *Crystal Structures*. Interscience, New York, 1963.
- [55] P.J.Linstrom. <http://webbook.nist.gov/chemistry/guide/>, 2003.
- [56] D. R. Gaskell. *Introduction to Metallurgical Thermodynamics*. McGraw-Hill, 1973.
- [57] J. P. Perdew and A. Zunger. Self-interaction correction to density-functional approximations for many-electron systems. *Physical Review B*, 23:5048–5079, 1981.

- [58] D. M. Ceperley and B. J. Alder. Ground state of the electron gas by a stochastic method. *Physical Review Letters*, 45:566–569, 1980.
- [59] P. Hohenberg and W. Kohn. Inhomogeneous electron gas. *Physical Review*, 136:B864–B871, 1964.
- [60] L. J. Sham and W. Kohn. Self-consistent equations including exchange and correlation effects. *Physical Review*, 140:A1133, 1965.
- [61] J. M. Soler, E. Artacho, J. D. Gale, A. García, J. Junquera, P. Ordejón, and D. Sánchez-Portal. The SIESTA method for ab initio order- n materials simulation. *Journal of Physics: Condensed Matter*, 14:2745–2779, 2002.
- [62] P. Ordejón, E. Artacho, and J. M. Soler. Self-consistent order- n density-functional calculations for very large systems. *Physical Review B*, 53:R10441–R10444, 1996.
- [63] J. M. Soler, E. Artacho, A. García, P. Ordejón, and D. Sánchez-Portal. Linear-scaling ab-initio calculations for large and complex systems. *Physica Status Solidi (b)*, 215:809–817, 1999.
- [64] W. E. Pickett. Pseudopotential methods in condensed matter applications. *Computational Physics Reports*, 9:115, 1989.
- [65] J. C. Phillips and L. Kleinmann. New method for calculating wave functions in crystals and molecules. *Physical Review*, 116:287–294, 1959.
- [66] N. Troullier and J. L. Martins. Efficient pseudopotentials for plane-wave calculations. *Physical Review B*, 43:1993–2006, 1991.
- [67] A. P. Horsfield. Efficient ab initio tight binding. *Physical Review B*, 56:6594–6602, 1997.
- [68] O. F. Sankey and D. J. Niklevsky. Ab initio multicenter tight-binding model for molecular-dynamics simulations and other applications in covalent systems. *Physical Review B*, 40:3979–3995, 1998.
- [69] O. Paz, E. Artacho, J. Junquera, and D. Sánchez-Portal. Numerical atomic orbitals for linear-scaling calculations. *Physical Review B*, 64:235111–235120, 2001.

- [70] R. D. King-Smith and D. Vanderbilt. First principles investigation of ferroelectricity in perovskite compounds. *Physical Review B*, 49:5828–5844, 1994.
- [71] C. G. Sánchez, A. Y. Lozovoi, and A. Alavi. Field-evaporation from first-principles. *Molecular Physics*, 102:1045–1050, 2004.
- [72] S. Huzinaga, J. Andzelm, M. Klobukowski, E. Radzio-Andzelm, Y. Sakai, and H. Tatewaki. *Gaussian basis sets for molecular calculations*. Elsevier, 1984.
- [73] C. G. Sánchez. *Estudio Teórico de la Interfase Electroquímica Mediante Cálculos de a Partir de Primeros Principios*. PhD thesis, Facultad de Ciencias Químicas, UNC, 2000.
- [74] J. Junquera, M. Zimmer, P. Ordejón, and P. Ghosez. First-principles calculation of the band offset at BaO/BaTiO₃ and SrO/SrTiO₃ interfaces. *Physical Review B*, 67:155327–155338, 2003.
- [75] P. Ordejón, E. Artacho, R. Cachau, J. Gale, A. García, J. Junquera, J. Kohanoff, M. Machado, D. Sánchez-Portal, J. M. Soler, and R. Weht. Linear scaling DFT calculations with numerical atomic orbitals. *Materials Research Society Symposium Proceedings*, 677:AA9.6.1, 2001.
- [76] *Landolt-Börnstein, Group III, Condensed Matter*, volume 36 subvol.V, chapter 1A Simple perovskite-type oxides, pages 116–147. Springer Verlag, 2002.
- [77] R. O. Bell and G. Rupprecht. Elastic constants of SrTiO₃. *Physical review*, 129:90–94, 1963.
- [78] B. Golding. Thermal expansivity and ultrasonic propagation near the structural transition of SrTiO₃. *Physical Review Letters*, 25:1439–1442, 1970.
- [79] N. Sai and D. Vanderbilt. First-principles study of ferroelectric and antiferrodistortive instabilities in tetragonal SrTiO₃. *Physical Review B*, 62:13942–13950, 2000.
- [80] V. Milman, B. Winkler, J. A. White, C. J. Pickard, M. C. Payne, E. V. Akhmatkaya, and R. H. Nobes. Electronic structure, properties, and phase stability of inorganic crystals: A pseudopotential plane-wave study. *Journal of Quantum Chemistry*, Volume 77:895–910, 2000.

- [81] R. D. Diehl and R. McGrath. Current progress in understanding alkali metal adsorption on metal surfaces. *Journal of Physics: Condensed Matter*, 9:951–968, 1997.
- [82] C. G. Van de Walle and J. Neugebauer. First-principles phase diagram for hydrogen on GaN surfaces. *Physical Review Letters*, 88:066103–066106, 2002.
- [83] L. M. Liborio, C. G. Sánchez, A. T. Paxton, and M. W. Finnis. Stability of Sr adatoms model structures for SrTiO₃(001) surface reconstructions. *Journal of Physics: Condensed Matter*, 17:L1–L8, 2005.
- [84] P. A. Redhead. Thermal desorption of gases. *Vacuum*, 12:203–211, 1962.
- [85] M. C. Desjonqueres and D. Spanjaard. *Concepts in Surface Physics*. Springer, 1996.
- [86] L. D. Marks, N. Erdman, and A. Subramanian. Crystallographic direct methods for surfaces. *Journal of Physics: Condensed Matter*, 13:10677–10688, 2001.
- [87] L. D. Marks, E. Bengu, C. Collazo-Davila, D. Grozea, E. Landree, C. Leslie, and W. Sinkler. Direct methods for surfaces. *Surface Review Letters*, 5:1087–1106, 1998.
- [88] L. J. Whitman. *to appear in The Encyclopedia of Applied Physics*, chapter Tunneling Microscopy and Spectroscopy. VCH.
- [89] J. Tersoff and D. R. Hamann. Theory and application for the scanning tunneling microscope. *Physical Review Letters*, 50:1998–2001, 1983.
- [90] J. Bardeen. Tunneling from a many-particle point of view. *Physical Review Letters*, 6:57–59, 1960.
- [91] U. Diebold, J. F. Anderson, K. Ng, and D. Vanderbilt. Evidence for the tunneling site on transition-metal oxides: TiO₂(110). *Physical Review Letters*, 77:1322–1325, 1996.
- [92] J. Smith and D. A. Bonnell. Determination of the TiO₂(110) (2×3) surface structure via a parametric approach to STM image simulation. *Physical Review B*, 62:4720–4725, 2000.
- [93] D. Jung, H. J. Koo, D. Dai, and M. H. Whangbo. Electronic structure study of scanning tunneling microscopy images of the rutile TiO₂(110) surface and their implications on the surface relaxations. *Surface Science*, 473:193–202, 2001.

- [94] S. N. Magonov and M.-H. Whangbo. *Surface analysis with STM and AFM*. VCH, 1996.
- [95] D. K. Seo, J. Ren, and M. H. Whangbo. Study of the origin of superstructure patterns in the scanning tunneling images of perylene-3,4,9,10-tetracarboxylic-dianhydride on graphite by electronic structure calculations. *Surface Science*, 370:252–258, 1997.
- [96] D. Jung, D. K. Seo, J. Ren, and M. H. Whangbo. Simulation of the scanning tunneling and atomic force microscopy images of a xanthine monolayer on graphite. *Surface Science*, 401:476–481, 1998.
- [97] T. Tanaka, K. Matsunaga, Y. Ikuhara, and T. Yamamoto. First principles study on structures and energetics of intrinsic vacancies in SrTiO₃. *Physical Review B*, 68:205213–205221, 2003.
- [98] K. Szot, W. Speier, J. Herion, and Ch. Freiburg. Restructuring of the surface region of SrTiO₃. *Applied Physics A*, 64:55–59, 1997.
- [99] Yu. Ya. Tomashpolsky, I. Ya. Kolotyrykin, and E. N. Lubnin. Thermostimulated segregation on oxide surfaces: auger spectroscopies and model views. *J. Microsc. Spectrosc. Electron.*, 10:521–537, 1985.
- [100] G. Horvath, J. Gerblinger, H. Meixner, and J. Giber. Segregation driving forces in perovskite titanates. *Sensors and Actuators B*, 32:93–99, 1996.
- [101] A. A. Chernov, J. J. De Yoreo, L. N. Rashkovich, and P. G. Vekilov. Step and kink dynamics in inorganic and protein crystallization. *MRS Bulletin*, 29:927–933, 2004.
- [102] X. Torrelles, J. Zegenhagen, J. Rius, T. Gloege, L. X. Cao, and W. Moritz. Atomic structure of a long-range ordered vicinal surface of SrTiO₃. *Surface Science*, 589:184–191, 2005.
- [103] J. G. Taylor, H. G. Smith, R. M. Nicklow, and M. K. Wilkinson. Lattice dynamics of rutile. *Physical Review B*, 3:3457–3472, 1971.